Dynamic Processes in the Line Shift and Linewidth of CaF_2 and $CsCdBr_3$ Doped with Er^{3+}

A thesis submitted in partial fulfilment of the requirements for the

Degree

Of Master of Science in Physics

By Adrian Reynolds

University of Canterbury

2012

Abstract

The linewidths and line positions of $^4I_{15/2}$ to $^4I_{13/2}$ absorption transitions of trivalent erbium in $CsCdBr_3$ and CaF_2 were measured as a function of temperature from approximately 10 K to 300 K. By comparing the temperature dependence of these transitions with theoretical models of electron-phonon coupling the primary mechanism involved were determined.

For Er^{3+} doped CaF_2 the Raman scattering processes dominated the line broadening, although the single-phonon direct processes were significant enough to drastically alter the values of the Raman scattering electron-phonon coupling constant. In comparison, the Er^{3+} doped $CsCdBr_3$ had negligible Raman scattering contributing to the line broadening. This is likely due to the exceedingly low Debye temperature and consequently low number of phonons, reducing the likelihood of two-phonon processes relative to single-phonon processes. The results were then analysed in terms of the bond length with the ligands and compared with other studies showing that as the bond length gets shorter the electron-phonon coupling constant associated with Raman scattering is expected to get smaller.

To explain the line shifts in CaF_2:Er^{3+} it is necessary to treat the Debye temperature as a parameter. This indicates that the phonon modes causing the line shifts are different from those causing the line broadening, and in most of the cases are vibronic processes rather than Raman processes. In the case of $CsCdBr_3$:Er^{3+} there is very little difference between the fits using the fixed Debye temperature and a varied Debye temperature in over half of the cases examined. Given the distribution of phonon modes, it is likely that this small difference arises because combinations of these processes are of similar intensity, meaning that a combination of Raman and optical phonon modes are likely causing the line shift.

Acknowledgements

I would like to thank my supervisors Jon-Paul Wells and Michael Reid for their assistance and the encouragement that they have provided to me throughout this project. This undoubtedly took longer than any of us expected, with delays caused by ill health and acts of God.

Thanks also to Scott Choi and Roger Reeves for helpful discussions.

I would especially like to thank Pubudu Senanayake, a fellow postgraduate student. He has provided valuable assistance and advice with experimental technique.

I would also like to thank the technical staff, especially Wayne Smith, for their prompt assistance whenever there were problems with the equipment.

Finally I would like to thank my family and friends for bearing with me as I worked on my studies.

Table of Contents

Abstract i

Acknowledgements ii

Chapter 1 Introduction 1

1.1 Motivation 1

1.2 Rare Earth Ions 2

1.3 Rare Earth Ions in Alkaline Earth Fluoride Crystals and AMX_3 Salts 3

1.4 An Outline of this Thesis 7

Chapter 2 Theoretical Background 9

2.1 The Free Ion 9

2.1.1 The Central Field Model 10

2.1.2 Spin-Orbit Coupling 11

2.1.3 The Configuration and Intra-Atomic Magnetic Interactions 12

2.2 The Crystal Field Model 14

2.3 Intensity Calculations 16

2.4 Models of Spectral Lineshapes 17

2.5 Dynamic Line-Broadening and Line-Shift Processes 19

Chapter 3 Experimental Details 23

3.1 Crystal Preparation 23

3.2 Infrared Absorption 24

Chapter 4 Temperature Dependent Infrared Absorption of $CaF_2:Er^{3+}$ 26

4.1 Introduction 26

4.2 IR Spectra 26

4.3 Crystal Field Analysis 30

4.4 Simulated Spectra 33

4.5 Temperature Dependent Linewidth Analysis 37
4.6 Temperature-Dependent Line Position Analysis 49
4.7 Conclusion 59
Chapter 5 Temperature Dependent Infrared Absorption of $CsCdBr_3:Er^{3+}$ 60
5.1 Introduction 60
5.2 IR Spectra 61
5.3 Crystal Field Analysis 63
5.4 Simulated Spectra 65
5.5 Temperature Dependent Linewidth Analysis 68
5.6 Temperature Dependent Line Position Analysis 74
5.7 Conclusion 80
Chapter 6 Discussion and Conclusions 80
References 84

Figures

1.1 CaF_2 crystal structure 4

1.2 CaF_2:RE^{3+} C_{4v} symmetry site 4

1.3 CaF_2:RE^{3+} C_{3v} symmetry site 5

1.4 $CsCdBr_3$ $[MX_3]^-$ chain 5

1.5 $CsCdBr_3$ substitution centers 6

2.1 Phonon processes 19

4.1 FTIR CaF_2:Er^{3+} spectra at 13K 28

4.2 FTIR CaF_2:Er^{3+} spectra at 70K 29

4.3 Experimental and simulated CaF_2:Er^{3+} spectra at 13K 34

4.4 Experimental and simulated CaF_2:Er^{3+} spectra at 70K 36

4.5 CaF_2:Er^{3+} linewidth: Z_1Y_2 C_{4v} Raman only 37

4.6 CaF_2:Er^{3+} linewidth: Z_1Y_3 C_{4v} Raman only 38

4.7 CaF_2:Er^{3+} linewidth: Z_2Y_1 C_{4v} Raman only 38

4.8 CaF_2:Er^{3+} linewidth: Z_3Y_1 C_{4v} Raman only 39

4.9 CaF_2:Er^{3+} linewidth: Z_1Y_1 C_{3v} Raman only 39

4.10 CaF_2:Er^{3+} linewidth: Z_1Y_2 C_{3v} Raman only 40

4.11 CaF_2:Er^{3+} linewidth: Z_3Y_2 C_{4v} Raman only 40

4.12 CaF_2:Er^{3+} linewidth: Z_1Y_1 C_{3v} 41

4.13 CaF_2:Er^{3+} linewidth: Z_1Y_2 C_{3v} 42

4.14 CaF_2:Er^{3+} linewidth: Z_1Y_2 C_{4v} 43

4.15 CaF_2:Er^{3+} linewidth: Z_2Y_1 C_{4v} 44

4.16 CaF_2:Er^{3+} linewidth: Z_3Y_2 C_{4v} 45

4.17 $CaF_2:Er^{3+}$ linewidth: Z_3Y_1 C_{4v} 46

4.18 $CaF_2:Er^{3+}$ linewidth: Z_1Y_3 C_{4v} 47

4.19 $CaF_2:Er^{3+}$ line position: Z_1Y_1 C_{3v} 50

4.20 $CaF_2:Er^{3+}$ line position: Z_1Y_2 C_{4v} 51

4.21 $CaF_2:Er^{3+}$ line position: Z_1Y_2 C_{3v} 52

4.22 $CaF_2:Er^{3+}$ line position: Z_1Y_3 C_{4v} 53

4.23 $CaF_2:Er^{3+}$ line position: Z_2Y_1 C_{4v} 54

4.24 $CaF_2:Er^{3+}$ line position: Z_3Y_2 C_{4v} 55

4.25 $CaF_2:Er^{3+}$ line position: Z_3Y_1 C_{3v} 56

4.26 $CaF_2:Er^{3+}$ line position: Z_2Y_2 C_{3v} 57

5.1 FTIR $CsCdBr_3:Er^{3+}$ spectra at 10K 61

5.2 FTIR $CsCdBr_3:Er^{3+}$ spectra at 70K 62

5.3 Experimental and simulated $CsCdBr_3:Er^{3+}$ spectra at 10K..... 66

5.4 Experimental and simulated $CsCdBr_3:Er^{3+}$ spectra at 70K..... 67

5.5 $CsCdBr_3:Er^{3+}$ linewidth: Z_1Y_1 69

5.6 $CsCdBr_3:Er^{3+}$ linewidth: Z_1Y_2 69

5.7 $CsCdBr_3:Er^{3+}$ linewidth: Z_1Y_3 70

5.8 $CsCdBr_3:Er^{3+}$ linewidth: Z_1Y_5 70

5.9 $CsCdBr_3:Er^{3+}$ linewidth: Z_2Y_1 71

5.10 $CsCdBr_3:Er^{3+}$ linewidth: Z_2Y_3 71

5.11 $CsCdBr_3:Er^{3+}$ linewidth: Z_2Y_4 72

5.12 $CsCdBr_3:Er^{3+}$ line position: Z_1Y_2..... 75

5.13 $CsCdBr_3:Er^{3+}$ line position: Z_1Y_3..... 76

5.14 $CsCdBr_3:Er^{3+}$ line position: Z_1Y_5 77

5.15 $CsCdBr_3:Er^{3+}$ line position: Z_2Y_1 78

5.16 $CsCdBr_3:Er^{3+}$ line position: Z_2Y_3 79

Tables

4.1 $CaF_2:Er^{3+}$ linewidths and line positions 30

4.2 $CaF_2:Er^{3+}$ Hamiltonian parameters 31

4.3 $CaF_2:Er^{3+}$ crystal field parameters 31

4.4 $CaF_2:Er^{3+}$ C_{4v} energy levels 32

4.5 $CaF_2:Er^{3+}$ C_{3v} energy levels 33

4.6 $CaF_2:Er^{3+}$ FWHM for C_{4v} for simulated spectra 35

4.7 $CaF_2:Er^{3+}$ FWHM for C_{3v} for simulated spectra 35

4.8 $CaF_2:Er^{3+}$ linewidth parameters 48

4.9 $CaF_2:Er^{3+}$ line shift parameters 58

5.1 $CsCdBr_3:Er^{3+}$ linewidths and line positions 63

5.2 $CsCdBr_3:Er^{3+}$ energy levels 64

5.3 $CsCdBr_3:Er^{3+}$ Hamiltonian parameters 64

5.4 $CsCdBr_3:Er^{3+}$ FWHM for simulated spectra 67

5.5 $CsCdBr_3:Er^{3+}$ linewidth parameters 73

5.6 $CsCdBr_3:Er^{3+}$ line shift parameters 79

Chapter 1 Introduction

1.1 Motivation

The purpose of this thesis is to investigate the electron-phonon coupling and the dynamic crystal field in Erbium doped crystals through variations in both linewidth and line position of infrared absorption transitions. This allows us to determine the dominant relaxation processes, giving a better understanding of the systems in question. The linewidth study tells us which phonon modes dominate in one phonon absorption or emission, or two phonon Raman scattering, and gives a minimum linewidth for that crystal. Studies of the temperature dependent line position tells us how well the Debye approximation holds for that system when the Debye temperature from the analysis is compared to the calculated or reference Debye temperature.

The 1.5μm transition of the trivalent erbium (Er^{3+}) is used extensively in communications. This is because the optical fibres used are commonly made of silica, in which the lowest loss window is in the region of 1.55 μm[1]. This means that the 1.5 μm $^4I_{13/2} \rightarrow {}^4I_{15/2}$ transitions of Er^{3+} are appropriate to make amplifiers[1][2] for long optical cables, whilst Er^{3+} doped semiconductor lasers are also used to generate the signal. Also, as knowledge of how temperature affects the linewidth and line position allows for the creation of temperature controlled semiconductor laser diodes which can be precisely tuned to the optimum transmission frequency for the silica, meaning smaller loss and therefore fewer amplifiers required for a given distance. This also allows for more precise optimisation of the detectors. Studies of the temperature dependence of linewidths[3][4][5][6][7] and line positions[4][5][6][7] of ions in crystals have been performed since the early 1960s, however these studies commonly focussed on transition-metal ions rather than the rare earths[3][4][5][6]. Of the reported works which deal with rare-earth ions [7] these most often focussed on europium and praseodymium[8][9][10]. We are not aware of many detailed studies of the technologically relevant, infrared transitions of trivalent erbium. The linewidth studies, both of rare earths and transition metal ions, were largely based off the direct single phonon absorption and emission processes, and two phonon Raman scattering. The component linewidth function, neglecting higher order terms, was developed by McCumber and Sturge in 1963[5], building on the seminal work of Van Vleck [11].

A comprehensive study of the linewidths of rare earth ions has been done by A Ellens in 1996[12], who studied line broadening of trivalent lanthanides in order to determine trends in electron-phonon coupling strength along the series. This showed that α, the electron-phonon coupling parameter derived from a fit with the Raman two phonon processes, is a good indicator of electron-phonon coupling strength [13][12]. They also found that α is large at the beginning and end of the lanthanide series, including Er^{3+}, and smaller in the centre [13][14]. When α is large it indicates that there is strong electron-phonon coupling, so Er^{3+} should have stronger electron-phonon coupling compared to the rare earth ions in the centre of the series. Strong electron-phonon coupling means that there is a strong interaction between electronic states and the phonon states.

1.2 Rare Earth Ions

Rare-earth metals include the lanthanide group of the periodic table as well as yttrium and scandium. They are characterised by partially filled 4f shells of their electronic configuration. They were first discovered in Ytterby, Sweden in 1787, and was first spectroscopically analysed in 1794 by J.J. Gadolin who described Yttria, which naturally contained a mixture of rare earth compounds. Of specific interest here are the lanthanides which contain a common configuration of a xenon-like rare gas shell of 54 electrons. The lanthanides do not include lanthanum itself which in its normal configuration has no 4f electrons.

Spectroscopically, it was found that lanthanide-doped compounds contained very sharp spectral lines. Becquerel, amongst others, studied these spectral lines at liquid helium temperatures and discovered that they became even sharper [15]. The lines originated from the 4f energy levels, and were split mostly due to the electric fields within the host lattice structures[16], giving a large number of very close together lines. These lines were theorised to be from intra-configurational 4f transitions and the inter-configurational 4f→5d transitions[17]. The outer 5s and 5p electrons surround the inner shells of electrons, effectively shielding the 4f electrons[16] due to the so called ‘lanthanide contraction’. The lanthanide contraction arises from the imperfect shielding of 4f electrons by other 4f electrons[18]. Proceeding through the lanthanide series, the charge of the nucleus and the number of 4f electrons increases by one at each step. With each increase, the effective nuclear charge increases, causing a reduction in radius of the entire $4f^n$ shell. This reduction of the radius is due to the aforementioned imperfect

screening of the 4f electrons. This means that the spectra we associate with the 4f valence shell appear much more like those of a free ion than that of a doped compound, and consequently we obtain the sharp spectral lines.

The rare-earth ion which is investigated in this study is erbium, which was discovered in 1843 by Mosander[17]. Erbium has an atomic number of 68, which has the electronic structure of [Xe] $4f^{12}$ $6s^2$. This means that erbium is a 'heavy' lanthanide, with a 4f shell over half full, and forms trivalent ions (Er^{3+}) with the electronic structure of [Xe] $4f^{11}$. Er^{3+} has many transitions in the infra-red region most notably at the 1.5μm telecommunications wavelength range due to $^4I_{13/2} \rightarrow {}^4I_{15/2}$ emission as mentioned above.

1.3 Rare Earth Ions in Alkaline Earth Fluoride Crystals and AMX_3 Salts

Alkaline-earth fluoride crystals have O_h^5 space group symmetry. They are thermally and mechanically stable having a cubic array of fluoride ions with the divalent alkaline earth ion in the centre of every second cube. When the crystal is doped with rare-earth ions (RE), the rare-earth takes the place of the divalent alkaline-earth ion. When the rare-earth ion is divalent, no charge compensation is required and thus the ion is most likely to occupy a site having cubic point group symmetry. When trivalent ions are incorporated, charge compensation will be required in order to maintain charge neutrality.

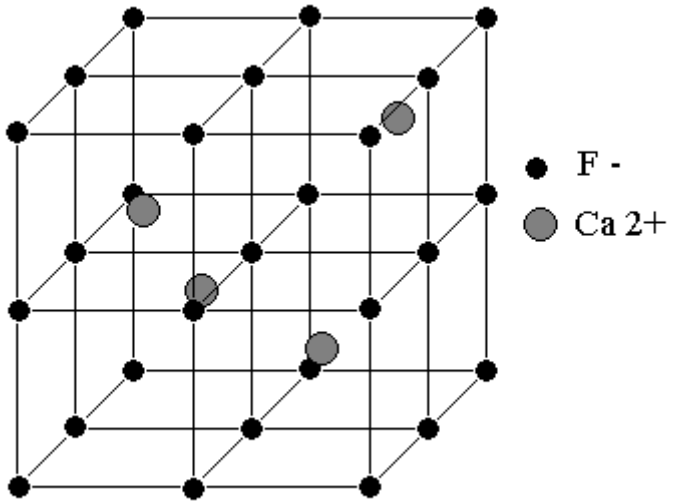

Figure 1-1: The CaF_2 crystal structure

For lightly doped CaF_2 crystals (less than 0.05 molar percent) the predominant centre will have C_{4v} point group symmetry consisting of an interstitial F^- ion located in the next nearest neighbour position along the <100> direction from the RE^{3+} ion.

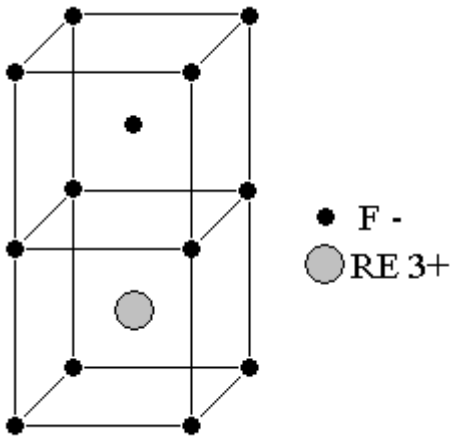

Figure 1-2: The CaF_2:RE^{3+} C_{4v}(F^-) symmetry site, showing the charge compensation along <100> with an interstitial F- ion.

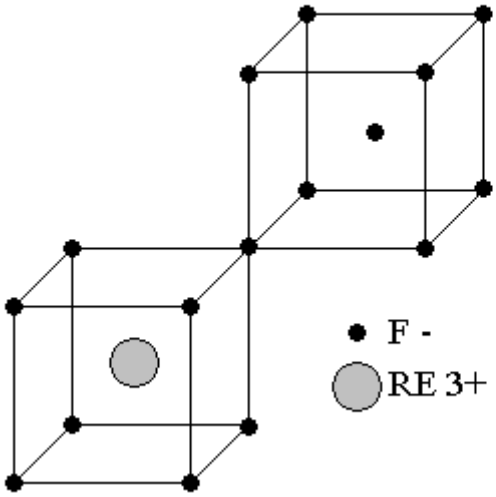

Figure 1-3: The $CaF_2:RE^{3+}$ $C_{3v}(F^-)$ symmetry site in a fluorite structure, showing charge compensation along <111> with an interstitial F- ion.

A minority centre of C_{3v} symmetry also occurs in $CaF_2:Er^{3+}$. In most fluorite structures, such as SrF_2 or BaF_2 this would be the $C_{3v}(F^-)$ site [19], a trigonal centre which consists of an RE^{3+} ion charge compensated by a F^- ion located in the next nearest neighbour position along the <111> direction. There is evidence that this is not the case in $CaF_2:Er^{3+}$, however [20][21]. In this situation the fluorine charge compensated centre has an unassigned configuration but is believed to have vacancies in the fluorine cage around the RE ion[20][21].

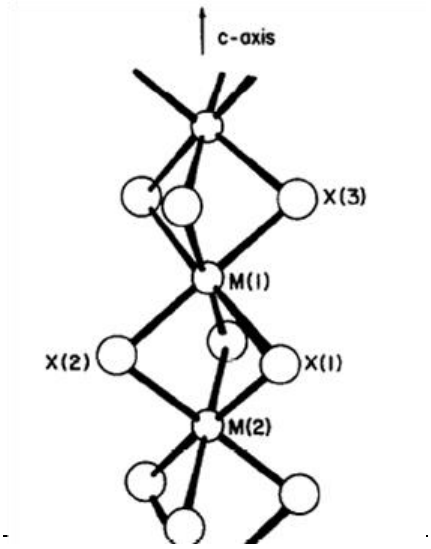

Figure 1-4: Part of an $[MX_3]^-$ chain, with the M denoting Cd^{2+} ions and X denoting Br^- ions in $CsCdBr_3$. This figure is sourced from McPherson et al [22].

AMX_3 salts, and in particular $CsCdBr_3$, have a hexagonal symmetry with $P63/mmc(D_{6h}^4)$ space group[23][22]. The most significant feature of the structure is that it forms face-sharing

anionic $(M^{2+}X_6^-)^{4-}$ chains[23], with a single divalent metal ion (M^{2+}) surrounded by six halide ions (X^-) in approximately an octahedral array, with D_{3d} point symmetry[23]. This octahedral array is elongated along the axis of the chain (the crystallographic c-axis). These chains are of infinite length and have A^+ ions between them.

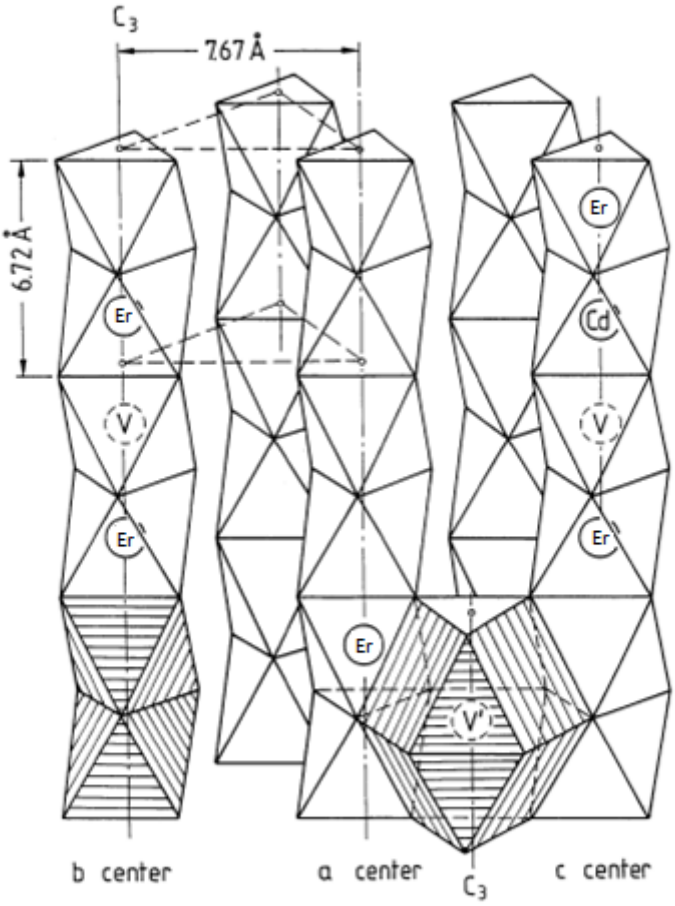

Figure 1-5: $CsCdBr_3:Er^{3+}$ crystal structure showing the possible substitution centers. The centre under investigation in this work is the b center. The V vacancies, the Er denote Er^{3+} ions. This figure is sourced from Heber et al [24].

When doped with trivalent rare earth ions (RE^{3+}), two RE^{3+} ions displace three adjacent M^{2+} ions, leaving a vacancy between.

$$-\ M^{2+}\ -\ RE^{3+}\ -\ v\ -\ RE^{3+}\ -\ M^{2+}\ -$$

This ensures charge remains balanced in the local lattice[23]. The point symmetry for each of the RE^{3+} ions in this arrangement is C_{3v}. There are other arrangements possible, but studies by Cockroft *et al* [25] indicate that this is the dominant arrangement of $CsCdBr_3:Er^{3+}$, with both of the Er^{3+} ions experiencing the same crystal field environment. The alternative arrangement,

$$-\ Cd^{2+}\ -\ Er^{3+}\ -\ Er^{3+}\ -\ v\ -\ Cd^{2+}\ -$$

gives distinct transitions for each ion as the two Er^{3+} ions are not in symmetric arrangements, with one Er^{3+} ion adjacent to a Cd^{2+} ion and the other adjacent to a vacancy. These Er^{3+} ions therefore have different potentials acting on them, which will be expressed as measurable differences in the spectra.

1.4 An Outline of this Thesis

Chapter two discusses the theoretical background of this thesis. The approximation of rare earths as free ions to determine energy levels is discussed, then how these are modified by the addition of spin-orbit parameters in section 2.1.

In section 2.2 the crystal field model is introduced, describing the energy levels from a theoretical basis and showing the crystal field splitting of the energy levels. These theoretical results can then be compared with experimental data to determine the accuracy of the model, and therefore can be used to determine the accuracy of the parameters used in the model.

Section 2.3 discusses the theoretical modeling of the intensities of the transition energy levels. This helps to identify the transitions which arise from each configuration, either C_{3v} or C_{4v} in this case.

Section 2.4 discusses the line shape of the transitions, the homogenous Lorentzian component and the inhomogeneous Gaussian components. The homogenous component arises due to Raman scattering and lifetime broadening which are temperature dependent, while the inhomogeneous component is temperature independent. This is expanded upon in section 2.5 where the models describing the temperature dependence of the linewidths and the line positions of the transition energies. There are five main components to the linewidth, the temperature independent homogenous term, the Raman scattering, the two-phonon Orbarch processes and direct one-phonon absorption and emission. There are also some higher order terms which not needed.

Chapter three discusses the experimental processes used in both preparing the crystals and then measuring the line -positions and –widths at a variety of temperatures.

Chapter four discusses the temperature dependence of the linewidths of the erbium-doped alkaline earth fluorides. The components of the linewidth are analyzed to see what processes

are dominant, and the coupling coefficients, α, are compared. A comparison is done between the different components of the linewidths between the different host metal ions in the crystals.

Chapter five discusses the temperature dependence of the line positions of the erbium doped alkaline earth fluorides. A comparison is then done on the different positions of the transition energy levels based on the differing host metal ions.

Chapter six discusses the temperature dependence of the linewidth and line position of the transition energy levels of erbium doped $CsCdBr_3$. A comparison is then done between the various different C_{3v} states and between the AMX_3 structure crystal and the fluorite structure crystals.

Chapter 2 Theoretical Background

There are two main considerations when dealing with the energy levels of rare earth (RE) ions in crystals, that of the free ion and that of the crystal field. The Hamiltonian can be written as the sum of these parts

$$H = H_f + H_{cf}$$

In the following the free ion component dominates on the large scale, giving the primary energy-level splitting, while the crystal field component can be seen as splitting the free-ion component.

Z is the atomic number and N is the number of electrons, L is total orbital momentum, S is total spin momentum, J is total angular momentum, nl describes the state (4f for the transitions in this thesis is given by $n = 4$, $l = 3$)

2.1 The Free Ion

The free-ion model is a model of an ion floating in free space, only affected by the magnetic and electrical fields of its component parts, without any external potentials acting on it. The total free ion Hamiltonian is given by

$$H_f = H_0 + H_{SO}$$

H_0 is due to accounts for the kinetic energy and potential energy of the electrons, arising from both the field of the nucleus and Coulomb interactions, and is given by

$$H_0 = H_K + H_U + H_C$$

$$H_0 = -\frac{\hbar^2}{2m}\sum_{i=1}^{N}\nabla_i^2 - e^2\sum_{i=1}^{N}\frac{Z_i}{r_i} + e^2\sum_{i<j}^{N} r_{ij}^{-1}$$

while H_{SO} accounts for spin-orbit interactions, given by

$$H_{SO} = \sum_{i=1}^{N} \xi(r_i)\, \boldsymbol{l}_i \cdot \boldsymbol{s}_i$$

It is impossible to find exact solutions to Schrödinger's equation for systems with multiple electrons, so approximations need to be made.

2.1.1 The Central Field Model

The central field model takes the first component of the free ion Hamiltonian above, H_0, and assumes that in the case of RE ions that it is minimally distorted by the unfilled 4f shell. This means that, as an approximation of the first two terms in H_0 above, the 4f electrons can be considered to be moving independently of each other in a central electric field, created by the other 4f electrons and the [Xe] core. The electrons therefore are considered to be moving in a spherically symmetric potential ($-U(r_i)/e$), giving

$$H_{Atomic} = \sum_{i=1}^{N} \left[\frac{-\hbar^2}{2m} \nabla_i^2 + U(r_i) \right]$$

The difference $H_0 - H_{Atomic}$ may then be treated as a perturbation potential, allowing you to write out Schrödinger's equation for the central field. This can be separated if we chose as solution such that

$$\Psi = \sum_{i=1}^{N} \varphi_i(a^i) \qquad \text{and} \qquad E_{CF} = \sum_{i=1}^{N} E_i$$

where a^i is an operator, which represents a set of quantum numbers, nlm_l. These cover the motion of a single electron in the central field. Converting to polar coordinates it is possible to write the effective Hamiltonian in terms of radial and angular parts. For the Coulomb interactions, using the Hartree-Fock method, this gives [26]

$$\frac{1}{r_{ij}} = \sum_{k=0}^{\infty} \frac{4\pi}{2k+1} \frac{r_<^k}{r_>^k} Y_i^{(k)} \cdot Y_j^{(k)}$$

where $r_>$ is the distance from the nucleus to the further electron being considered, $r_<$ the distance from the nucleus to the nearer, and

$$Y_i^{(k)} \cdot Y_j^{(k)} = \sum_{-k \le q \ge k} (-1)^q Y_q^{(k)}(\theta_i, \varphi_j)\, Y_{-q}^{(k)}(\theta_j, \varphi_i)$$

Therefore, for *N* equivalent electrons in orbits *nl*, the matrix operator of H_C can be expressed as

$$\left\langle l^N \tau LS \middle| \sum_{i>j}^{N} \frac{e^2}{r_{ij}} \middle| l^N \tau LS \right\rangle = \sum_k f_k(l,l) F^k(nl,nl)$$

where $k = 0,2,4,6$ and $F^k(nl,nl)$ are Slater radial integrals, describing the radial component of electrostatic interaction, and are defined by

$$F^k(nl,nl) = e^2 \iint_0^\infty \frac{r_<^k}{r_>^{k+1}} [R_{nl}(r_i)]^2 \left[R_{nl}(r_j)\right]^2 dr_i dr_j$$

The values of the F^k can be calculated, but in practice they are usually experimentally determined [26].

The angular part of the matrix, $F^k(l,l)$, may however be calculated [18].

2.1.2 Spin-Orbit Coupling

H_0 is due to electrostatic interactions, but there are also magnetic interactions. These involve spin-orbit interactions, as well as spin-spin or spin-other-orbit interactions, but the most significant are spin-orbit. In spin-orbit coupling, the Hamiltonian is given by

$$H_{SO} = \sum_{i=1}^{N} \xi(r_i)\, \boldsymbol{l}_i \cdot \boldsymbol{s}_i$$

where l_i is the orbital angular momentum, $\boldsymbol{s_i}$ is the spin, r_i is the radial coordinate of the i^{th} electron, while

$$\xi(r_i) = \frac{\hbar^2}{2m^2c^2 r_i} \frac{dU(r_i)}{dr_i}$$

When there are strong spin-orbit interactions, such as in the case of rare earth ions, the matrix is diagonalized. This allows a wave function describing the resultant energy states to be written in terms of the basis states. The spin-orbit contribution can be written as [27]

$$\langle l^N LSJM | \sum_{i=1}^{N} \xi(r_i) l_i \cdot s_i | l^N L'S'J'M' \rangle = \zeta_{nl} A_{SO}(nl)$$

where ζ_{nl} is the spin-orbit interaction parameter, defined by

$$\zeta_{nl} = \int_0^\infty [R_{nl}(r)]^2 \xi(r) dr$$

This can be evaluated numerically, using the Hartree -Fock central field potential [26], but it is usually derived using experimentally observed energy levels.

$A_{SO}(nl)$ is a matrix element, which in the case of $S = S'$ and $L = L'$ can be reduced to

$$A_{SO} = \frac{\lambda}{2}[J(J+1) - L(L+1) - S(S+1)]$$

where λ is constant for a given L and S.

2.1.3 The Configuration and Intra-Atomic Magnetic Interactions

Other parameters need to be added to the Hamiltonian to account for higher order interactions. These are

$$H_{c1=} \alpha L(L+1) + \beta G(G_2) + \gamma G(R_7)$$

where L is the total orbital angular momentum, α, β and γ are the parameters associated with the two-body correction terms and $G(G_2)$ and $G(R_7)$ are Casmir's operators for the groups G_2 and R_7 [28]. These terms were first introduced by Rajnak and Wybourne in 1963 [29].

$$H_{c2} = \sum_{i=2,3,4,6,7,8} T^i t_i$$

This term is included when $N \geq 3$ such as in Er^{3+}, as it represents three particle interactions. T^i are the parameters and t_i are the three particle operators. These terms were first introduced by Judd in 1966 [30].

$$H_{c3} = \sum_{h=0,2,4} M^h m_h$$

This term represents magnetic relativistic effects, where the parameters given by M^h are the Marvin integrals. These represent the spin-spin and spin-other-orbit relativistic corrections, while m_h represents the effective operator. These terms were first introduced by Marvin in 1947 [31].

$$H_{c4} = \sum_{k=2,4,6} P^k p_k$$

This term accounts for electrostatically correlated magnetic interactions, with P^k as the parameter, and p_k as the effective operator.

The effective Hamiltonian for $4f^n$ free ions is therefore given by

$$H_{FI} = H_K + H_U + \sum_{k=2,4,6} F^k f_k + \zeta_f A_{SO} + \alpha L(L+1) + \beta G(G_2) + \gamma G(R_7) + \sum_{i=2,3,4,6,7,8} T^i t_i + \sum_{h=0,2,4} M^h m_h + \sum_{k=2,4,6} P^k p_k$$

2.2 The Crystal Field Model

A free atom or ion has spherical symmetry, and each energy level is $(2J + 1)$ degenerate. Once a free ion is placed in a crystalline host it is surrounded by other ions, and therefore loses its spherical symmetry and there is a concomitant reduction in the degeneracy of the individual energy levels. The effect of this is to split the energy levels, and it should be possible to predict how this happens from first principles due to a specific crystal field symmetry environment[32]. This is, in practice, difficult to do due to the complexity of the crystal field interactions, so simplified models are usually used instead. The Hamiltonian for the ion in the crystal field is given by

$$H = H_{FI} + H_{cf}$$

Where the first term is due to the spherically symmetric part of the Hamiltonian, the term as a free ion, given in section 2.1.3, and the second term is due to the crystal field. This term can be considered a perturbation on the free ion, to split the energy levels, lifting the degeneracy.

The component of the Hamiltonian given by H_{cf} expressed as

$$H_{cf} = \sum_{k,q} B_q^k C_q^{(k)} \qquad (1)$$

is due to the crystal field itself, where B_q^k is due to radial factors and $C_q^{(k)}$ is due to angular factors. The radial factors are treated as experimentally derived parameters, whereas the radial factors can be expressed numerically in terms of Racah spherical tensors. This gives

$$C_q^{(k)} = \sqrt{\frac{4\pi}{2k+1}} Y_{kq}$$

where Y_{kq} is the spherical harmonics.

The possible values of *k* and *q* can be minimised by considering several factors:

- If $k = q = 0$ then the field remains spherically symmetric, shifting all energy levels by the same amount, and therefore not contributing to energy splitting.

- For the f to f transitions, such as those of the rare earths in this thesis, the odd *k* terms in a crystal field expansion result in integrals which are effectively zero. Therefore only the even terms need to be considered.
- $l_1 + l_2 \geq k$
- For f electrons, $l = 3$, therefore $k \leq 6$

Taken together, these indicate that for f to f transition, $k = 2,4,6$

For the symmetry sites in this thesis, C_{4v} and C_{3v}, H_{cf} is given by

$$H_{cf}(C_{4v}) = B_A^2 C_0^{(2)} + B_A^4\left[C_0^{(4)} - \sqrt{\frac{7}{10}}\left(C_4^{(4)} + C_{-4}^{(4)}\right)\right] + B_A^6\left[C_0^{(6)} + \sqrt{\frac{1}{14}}\left(C_4^{(6)} + C_{-4}^{(6)}\right)\right] + B_C^4\left[C_0^{(4)} + \sqrt{\frac{5}{14}}\left(C_4^{(4)} + C_{-4}^{(4)}\right)\right] + B_C^6\left[C_0^{(6)} - \sqrt{\frac{7}{2}}\left(C_4^{(6)} + C_{-4}^{(6)}\right)\right] \quad (2)$$

where the Racah tensors are given by $C_q^{(k)}$, while the radial factors, B_q^k, have been selected in order to split the Hamiltonian into cubic and axial components[33], using the notation of *Mujaji et al* [34] where

$$B_A^2 = B_0^2$$

$$B_A^4 = \frac{15}{2}B_0^4$$

$$B_A^6 = \frac{7}{8}B_0^6$$

$$B_C^4 = B^4 + \frac{7}{12}B_0^4$$

$$B_C^6 = B^6 + \frac{1}{8}B_0^6$$

are the operators in order to convert equation (2) into the form used in equation (1), and

$$H_{cf}(C_{3v}) = B_A^2 C_0^{(2)} + B_A^4\left[C_0^{(4)} - \frac{1}{2}\sqrt{\frac{7}{10}}\left(C_3^{(4)} - C_{-3}^{(4)}\right)\right]$$
$$+ B_A^6\left[\sqrt{\frac{11}{42}}\left(C_3^{(6)} - C_{-3}^{(6)}\right) + \sqrt{\frac{5}{21}}\left(C_6^{(6)} + C_{-6}^{(6)}\right)\right]$$
$$+ B_A^{6\prime}\left[C_0^{(6)} + \frac{4}{7}\sqrt{\frac{10}{21}}\left(C_3^{(6)} - C_{-3}^{(6)}\right) - \frac{4}{7}\sqrt{\frac{11}{21}}\left(C_6^{(6)} + C_{-6}^{(6)}\right)\right] + B_C^4\left[C_0^{(4)} + \sqrt{\frac{10}{7}}\left(C_3^{(4)} - C_{-3}^{(4)}\right)\right]$$
$$+ B_C^6\left[C_0^{(6)} - \sqrt{\frac{35}{96}}\left(C_3^{(6)} - C_{-3}^{(6)}\right) + \frac{1}{8}\sqrt{\frac{77}{3}}\left(C_6^{(6)} + C_{-6}^{(6)}\right)\right] \qquad (3)$$

is also split into cubic and axial components, [33] also using the notation of *Mujaji* [35] where

$$B_A^2 = B_0^2$$

$$B_A^4 = 2\frac{\sqrt{70}}{27}\left(\sqrt{\frac{10}{7}}B_0^4 - B_3^4\right)$$

$$B_A^6 = \frac{\sqrt{42}}{21}\left(\sqrt{10}B_6^6 - \sqrt{11}B_3^6\right)$$

$$B_A^{6\prime} = \frac{56}{81}\left(\frac{7}{8}B_0^6 - \sqrt{\frac{10}{21}}B_3^6 - \sqrt{\frac{11}{21}}B_6^6\right)$$

$$B_C^4 = 2\frac{\sqrt{70}}{27}\left(\frac{1}{2}\sqrt{\frac{7}{10}}B_0^4 + B_3^4\right)$$

$$B_C^6 = \frac{56}{81}\left(\frac{4}{7}B_0^6 + \sqrt{\frac{10}{21}}B_3^6 + \sqrt{\frac{11}{21}}B_6^6\right)$$

are the operators used to covert equation (3) into the form used in equation (1)

2.3 Intensity Calculations

The theoretical calculation of intensity in this thesis is based off of the magnetic dipole transitions. With $q = (0, -1, 1)$ and with the magnetic dipole operator defined as

$$M_q^{(1)} = \frac{-e\hbar}{2mc}\left(L_q^{(1)} + 2S_q^{(1)}\right)$$

The magnetic dipole line strength can be written as [26]

$$S_{FI,q}^{MD} = \sum_i \sum_f \left|\left\langle Ff\left|M_q^{(1)}\right|Ii\right\rangle\right|^2$$

This can be used to express the intensity in a non-polarised crystal, however the $CsCdBr_3$ used requires further consideration. For orthoaxial measurements and defining the electric field along the z axis, the magnetic field along the x axis, the intensity can be written as [26]

$$S_{FI,\pi}^{MD} = \frac{1}{2}\left(S_{FI,1}^{MD} + S_{FI,-1}^{MD}\right)$$

If the electric field is instead perpendicular to the z axis the intensity is given by the σ value:

$$S_{FI,\sigma}^{MD} = S_{FI,0}^{MD}$$

For the axial spectra the dipole strength is given as

$$S_{FI,axial}^{MD} = S_{FI,\pi}^{MD\,\prime}$$

2.4 Models of Spectral Lineshapes

There are several processes that contribute to the lineshape. There is a natural linewidth for spectral lines associated with long lived energy states, arising from the uncertainty principle. The longer the lifetime, the narrower the natural linewidth for that transition. The measured linewidth of a transition is almost always larger than that expected due to the lifetime of that state. The increased linewidth is due to a number of factors, giving a total temperature dependent linewidth of

$$v = v^{Inh} * (v^{Raman} + v^{Abs} + v^{Ems} + v^{Orbach} + v^{R.R.} + v^{Multiphonon})$$

v^{Inh} is the inhomogeneous component, the part that is independent of temperature to a very good approximation. It is caused by the random distribution of microscopic strain fields in the material[32] which are different for each site of each ion, dependent on the local crystal field environment. This component has a Gaussian line shape.

v^{Raman} is the component due to two-phonon Raman scattering. This is where phonons of differing energies are absorbed and emitted, but the ion remains in the same state, therefore not altering the lifetime of the energy level. The intermediate state between the phonon getting absorbed and getting emitted is a virtual state. This component has a Lorentzian lineshape.

v^{Abs} and v^{Ems} are the components covering direct one-phonon absorption and emission. This is where a single phonon is absorbed or emitted, changed the state of the ion. This, therefore, is part of the lifetime broadening process, and is the usually the largest contributor. These components also have Lorentzian lineshapes.

The other components of the linewidth, v^{Orbach}, $v^{R.R.}$ and $v^{Multiphonon}$, are the Orbach relaxation, the two-phonon Raman relaxation and the multiphonon relaxation. All of these terms are higher order than the single phonon direct terms, and in the temperature ranges studied in this thesis are very small compared to the other processes involved and therefore do not have a measurable effect [32]. The reason the Raman scattering is significant, despite also being a second order process, is due to the integration along the range of multiple phonon states.

Therefore, only the three dynamic processes which can cause line broadening, and the inhomogeneous component, are being considered. These processes can be considered by the model in figure 2.1.

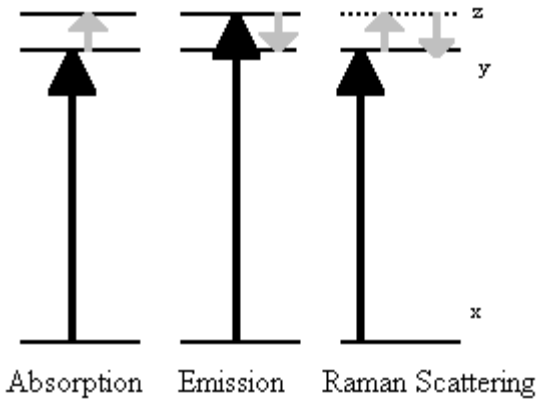

Figure 2-1: In the case of the absorption, the transition is from the ground state, x, to the excited state, y. This transition is then broadened by the absorption of the phonon, and moves, non-radiatively, to state z. In the case of the emission, the primary transition is from x to z. This state then emits a phonon and decays non-radiatively to state y. In the case of Raman scattering, the transition from x to y is broadened by the two phonons, y to the virtual state z and then z to y, but it is important to note that the state does not actually change.

Due to the differing component lineshapes between the inhomogenous and the homogenous terms, the resultant lineshape has a Voigt profile. This is a convolution of the Gaussian and the Lorentzian components.

2.5 Dynamic Line-Broadening and Line-Shift Processes

Of the terms being considered for temperature-dependent line broadening, and when dealing with the full-width at half maximum of the resulting line, the components can be approximated as

$$\Delta v = \Delta v^{Inh} * (\Delta v^{Raman} + \Delta v^{Abs} + \Delta v^{Ems})$$

Δv^{Inh} is independent of temperature, and so will be treated as a constant in the models.

Δv^{Raman} can expressed as

$$\Delta v^{Raman} = \alpha \left(\frac{T}{T_D}\right)^7 \int_0^{T_D/T} \frac{x^6 e^x}{(e^x - 1)^2} dx$$

where α is an electron-phonon coupling coefficient, and is given by

$$\alpha = (3.34 \times 10^{-11}) \frac{9}{2\pi^3 \rho^2 \mathrm{v}^{10}} \left(\frac{k_B T_D}{\hbar}\right)^7 \times \left(\sum_{j \neq i} \frac{\left|\langle \psi_i^{el} | V_1 | \psi_j^{el} \rangle\right|^2}{E_i^{el} - E_j^{el}} + \langle \psi_i^{el} | V_2 | \psi_j^{el} \rangle \right)^2$$

and the Debye temperature, T_D, is defined in terms of the Debye cutoff frequency

$$T_D = \frac{\hbar \omega_D}{k_B}$$

The Debye temperature is treated as a constant for the purposes of linewidth study, while α is treated as a variable to be experimentally derived.

The direct process terms, Δv^{Abs} and Δv^{Ems}, can be expressed as

$$\Delta v^{Abs} = \sum_{f>i} \beta'_{if} \frac{1}{e^{\frac{\hbar \omega_o}{k_B T}} - 1}$$

$$\Delta v^{Ems} = \sum_{f<i} \beta'_{if} \frac{e^{\frac{\hbar \omega_o}{k_B T}}}{e^{\frac{\hbar \omega_o}{k_B T}} - 1}$$

where β is an electron-phonon coupling coefficient, given by

$$\beta'_{if} = 3.34 \times 10^{-11} \left(\frac{3|\omega_o|^3}{2\pi \rho \mathrm{v}^5 \hbar} \left|\langle \psi_f^{el} | V_1 | \psi_i^{el} \rangle\right|^2 \right)$$

In units of wavenumber, and varying dependent on the transition, *i*→*f*, involved. The terms β'_{if} are also treated as variables to be experimentally derived.

The approximation

$$f_V \approx 0.5346 f_L + \sqrt{0.2166 f_L^2 + f_g^2}$$

is used to approximate the convolution, where f_V is the FWHM of the Voigt linewidth, f_L is the sum of the Lorentzian components and f_g is the Gaussian component [36]. This approximation reduces to a pure Gaussian where $f_L = 0$, but when $f_g = 0$ it does not reduce to a pure Lorentzian. This should not matter on the data range being used, as there will be a notable Gaussian component even when f_L dominates.

The positions of the absorption lines are also shifted by the phonons, and these positions are also temperature dependent. This is due to the continual absorption and emission of virtual phonons by the ion in the host crystal. This is different from Raman scattering as the two phonons have the same frequency. The phonon field itself makes an energy contribution to the system of ions. The contribution in the i^{th} energy state is given by

$$\delta v_i = \langle \psi_i | H_2^{ep} | \psi_i \rangle + \sum_{j \neq i} \frac{\left| \langle \psi_j | H_2^{ep} | \psi_i \rangle \right|^2}{E_i - E_j}$$

Using a first and second order electron-phonon interaction Hamiltonian, combined with the above equation, an equation describing the temperature dependence of spectral line position can be determined. Once the temperature-independent part has been removed, the equation needs to be split into two components for ease of calculation.

First consider the contribution from states with energies such that $|Ei - Ej| \gg \hbar\omega_D$. Using the Debye model for the distribution of phonons, the contribution can be written as

$$\delta v_i^a(T) = \alpha' \left(\frac{T}{T_D}\right)^4 \int_0^{\frac{T_D}{T}} \frac{x^3}{e^x - 1} dx$$

where the coupling constant α' is given by

$$\alpha' = (5.03 \times 10^{15}) \frac{3\hbar}{2\pi^2 \rho v^5} \left(\frac{k_B T_D}{\hbar}\right)^4 \left(\langle \psi_i^{el} | V_2 | \psi_i^{el} \rangle + \sum_{j \neq i} \frac{\left| \langle \psi_i^{el} | V_1 | \psi_j^{el} \rangle \right|^2}{E_i^{el} - E_j^{el}} \right)$$

where α' has units of wavenumbers and can be positive or negative. A positive α' indicates that the intermediate energy level has a greater energy level than the initial energy level, while a negative α' indicates that it is lower. Therefore this component can cause a positive or negative line shift with an increase in temperature.

Now, considering the contribution from states such that $|E_i - E_j| \leq \hbar\omega_D$. Once again using the Debye model for the distribution of phonons, the contribution can be written as

$$\delta\nu_i^b(T) = \sum_{j<i} \beta'_{ij} \left(\frac{T}{\Delta E_{ij}}\right)^2 \mathbf{P} \int_0^{\frac{T_D}{T}} \frac{x^3}{e^x - 1} \frac{1}{x^2 - \left(\frac{\Delta E_{ij}}{k_B T}\right)^2} dx$$

$$- \sum_{j>i} \beta'_{ij} \left(\frac{T}{\Delta E_{ij}}\right)^2 \mathbf{P} \int_0^{\frac{T_D}{T}} \frac{x^3}{e^x - 1} \frac{1}{x^2 - \left(\frac{\Delta E_{ij}}{k_B T}\right)^2} dx$$

where β_{ij}' is a coupling constant with units of wavenumbers and is given by

$$\beta'_{ij} = (3.34 \times 10^{-11}) \frac{3|\omega_{ij}|^3}{2\pi^2 \rho v^5} \left|\langle \psi_i^{el} | V_1 | \psi_j^{el} \rangle\right|^2$$

and **P** is the principal value of the integral.

When these equations are used to fit experimental results, the coupling constants and T_D are treated as variables. The reason T_D is treated as a variable is because the value for it is usually not the same for line shift measurements as it is for linewidth measurements, as the electron-phonon coupling is not the same in all phonon modes, particularly for those contributing to the differing processes.

Chapter 3 Experimental Details

3.1 Crystal Preparation

The CaF_2 crystals used in this study were grown from offcuts of CaF_2 crystals purchased from CRYSTRAN Ltd in the United Kingdom. The offcuts were crushed and then mixed with ErF_3 (which was in the form of a powder) in the appropriate concentrations. The exact concentration of 0.05% was chosen such that the lowest energy spectral lines of the $^4I_{13/2}$ multiplet were sharp and strongly absorbing. In the case of CaF_2:Er^{3+} a low concentration was desirable to avoid unnecessary spectral congestion because of the presence of clustering. This would mean that adjacent Er^{3+} ions would modify the symmetry sites, and therefore the energy levels, causing slight shifts in the spectra.

The crystals were grown in graphite crucibles over a period of 24 hours using an Arthur D. Little 38 kW radio frequency furnace. The vertical Bridgman-Stockbarger (temperature gradient) method was employed in the crystal growth process which entailed lowering the crucible through a temperature gradient in a vacuum of around 10^{-5} Torr. Small amounts of PbF_2 were added to the charge prior to lowering in order to scavenge for residual oxygen. Annealing is achieved via an automatic cooling cycle which leads to an improved quality crystal without cracks due to thermal stress.

The crystals were cut using a Struers Minitom diamond lined blade cutter at 150 rpm at a cutting rate of 2.5 mm/hour, using a Struers cutting fluid for Minitom. The faces were cut at slightly different angles to minimise internal reflection.

The faces of the crystals were polished on a Lab Pol-2 crystal polisher with a P1000 polishing paper, covered with water and Struers DP lubricant for 25 seconds at 250 rpm, then a further 15 seconds at 500 rpm on each side. The P1000 polishing paper replaced with P4000, which was once again covered with water and the Struers DP lubricant and polished for 30 seconds at 250 rpm then 30 seconds at 500 rpm on each side. Next, a MD Dur polishing cloth was used to polish the crystals, using 9 μm diamond particles in suspension (Struers DP-suspension –P) and the Struers DP lubricant. This was done at 250 rpm for 2 minutes, then 500 rpm for 3 minutes on each side. The optical finish was then checked, and the final stage repeated as necessary.

In addition to the crystals grown by the author, a $CsCdBr_3:Er^{3+}$ crystal was used. This crystal was grown during the mid 1990's. Caesium Cadmium Bromide crystals are also grown using the Bridgman-Stockbarger technique but at low temperatures and in sealed quartz ampoules in an HBr atmosphere. The crystal in question was provided 'ready to use' with an excellent optical finish provided by cleaving the crystal surfaces.

3.2 Infrared Absorption

Infrared spectra were taken with the Physics and Astronomy Department's Digilab FTS-40 Infrared Fourier Transform (FTIR) spectrometer. The FTS-40 is a single beam spectrometer which employs a He-Ne 3121 H-P model laser to determine the interference fringe spacings. The spectrometer has two compartments. One uses a deuterated triglycline sulphate (DTGS) detector to cover the 400-4500 cm^{-1} spectral range at room temperature. The other (external) compartment has two detectors. A mercury cadmium telluride (MCT) detector coupled with a KBr beamsplitter and globar source for response in the 400-4000 cm^{-1} region or for experiments in the 3000-15000 cm^{-1} region, an indium antimonide detector, quartz beamsplitter and quartz halogen source. The interferometer of this system comes as a lift-out unit which can be changed with comparative ease. The entire beampath is flushed with dry N_2 gas to minimize the effects of atmospheric absorption in the region of interest in this study.

The spectrometer has a resolving power down to 0.1 cm^{-1}. In Fourier-transform spectroscopy, the resolution is $\delta f_0 = 1/L$, where L is the maximum optical path difference in the Michelson interferometer of the Fourier transform spectrometer. If no special apodisation is used δf_0 represents the difference in wavenumber between the first zeros of the instrumental function $\mathrm{sinc}\, x = (\sin x)/x$ while the full-width half-maximum (FWHM) of this function is 0.603 δf_0 . The shape of spectral lines with a FWHM not smaller than δf_0 is not distorted by the spectrometer.

The linewidths of the spectral lines observed in the spectra obtained from this spectrometer were in general taken from direct fits to a combined Gaussian and Lorentzian lineshape function, as given in chapter two.

A secondary approach can also be used. When monochromatic light is incident on an ion with electrons in a non excited state absorption of those photons may take place. The intensity of the transmitted radiation at a frequency of absorption is:

$$I = I_0 \exp(-\alpha t)$$

where I_0 is the radiation intensity, α is the absorption coefficient and t is the thickness of the crystal. The half width at half intensity maximum (or half width at half height) is determined such that:

$$\alpha_{1/2} = \frac{1}{2}\alpha_m$$

where α_m is the absorption coefficient at the maximum of absorption or the centre wavelength. By substitution of the expression for I and simplification we get:

$$2ln\left(\frac{I_0}{I_{\frac{1}{2}}}\right) = ln\left(\frac{I_0}{I_m}\right)$$

Using $log_b x^n = n log_b x$ we can say

$$ln\left(\frac{I_0}{I_{\frac{1}{2}}}\right)^2 = ln\left(\frac{I_0}{I_m}\right)$$

$$\left(\frac{I_0}{I_{\frac{1}{2}}}\right)^2 = \left(\frac{I_0}{I_m}\right)$$

and finally

$$I_{\frac{1}{2}} = \sqrt{I_0 I_m}$$

Therefore by taking the geometric mean of the incident intensity I_0 and the intensity at maximum absorption I_m we can work out a closely approximate value for the intensity which yields the FWHM. This gives a useful check on the fitted values most often used and quoted in this study.

Chapter 4 Temperature Dependent Infrared Absorption of $CaF_2:Er^{3+}$

4.1 Introduction

Calcium Fluoride (CaF_2) is an alkaline earth fluoride of the fluorite structure. *Ho and Ruoff* determined the Debye temperature of CaF_2 to be 519 K in 1967[37]. The trivalent erbium ion, Er^{3+}, is capable of being in one of three symmetry states, either of two main C_{3v} symmetry states[20], or a C_{4v} symmetry state. Previous work on $CaF_2:Er^{3+}$ has mainly focused on single temperatures, with *Freeth et al* [38] studying the Zeeman effect, while *Cockroft et al* [20] isolated the different symmetry sites using laser site selection spectroscopy. In the course of their work, both of these efforts have produced crystal field calculations, which provide parameters to be used as a starting point in the crystal field calculations in this chapter. These crystal field calculations are then used to create simulated spectra, providing a model for the final equations of line position and linewidth to eventually fit into.

The models used here for temperature-dependent linewidth are based on a simplified approximation, neglecting several higher order terms. They do, however, adequately describe the behavior of the transitions in almost all the circumstances, although it is difficult in some cases to isolate exactly which single-phonon direct process is dominant. There is enough information, however, to state that in almost all circumstances the Raman scattering contribution is much larger than the single-phonon direct processes contribution.

The models for temperature dependent line position are also based on a simplified approximation. Although there is some evidence that states with intermediate energies less than the Debye energy have some effect, the approximation seems valid. The differences between the Debye temperatures obtained from most of the line position models and the Debye temperatures used in the linewidth models suggests that in most cases different phonon processes broaden the transitions than cause the shifts.

4.2 IR Spectra

The initial line positions were determined using the energy levels deduced by Freeth *et al* [38] for the C_{4v} symmetry site, and Cockroft *et al* [20] for the C_{3v} symmetry sites. The energy levels defined by *Freeth et al* and *Cockroft et al* were compared to the energy levels observed in the experimental spectra, allowing transitions to be assigned. This showed that in CaF_2 the majority of the Er^{3+} was in a C_{4v} state. By comparison with the data from Cockroft *et al*, it was determined that the majority of the erbium in this system that was in a C_{3v} centre was in the B centre, although there were a few transitions observed that seemed to originate in the G1 centre.

As expected, all of the transitions identified are narrow. Even the widest, those involving the $Y_4\ \gamma_7$ excited state, are narrow relative to the energy spacing. The transition assigned X is assumed to be from an impurity. This energy level does not seem to correspond to any transitions for Er^{3+} in a C_{4v} site or with either of the C_{3v} sites. Therefore this transition was assigned, based on the energy levels by Hargreaves [39] to a ground state $^3H_4\ Z_1 \rightarrow {}^3F_3\ V_4$ transition of Pr^{3+}. This transition is observed at all the temperatures studied.

As the temperatures increase the spectral lines broaden and merge, therefore it become increasingly difficult to model lineshapes to these transitions. This means that, particularly in the more crowded areas, such as between 6500 and 6600 cm^{-1}, there are only a small range of temperatures over which it is possible to model the lineshape. Further, the noise in the spectra means that low intensity transitions cannot adequately be isolated from the background. These factors limit the number of transitions which are able to be studied, and the temperature ranges over which those available can be usefully described.

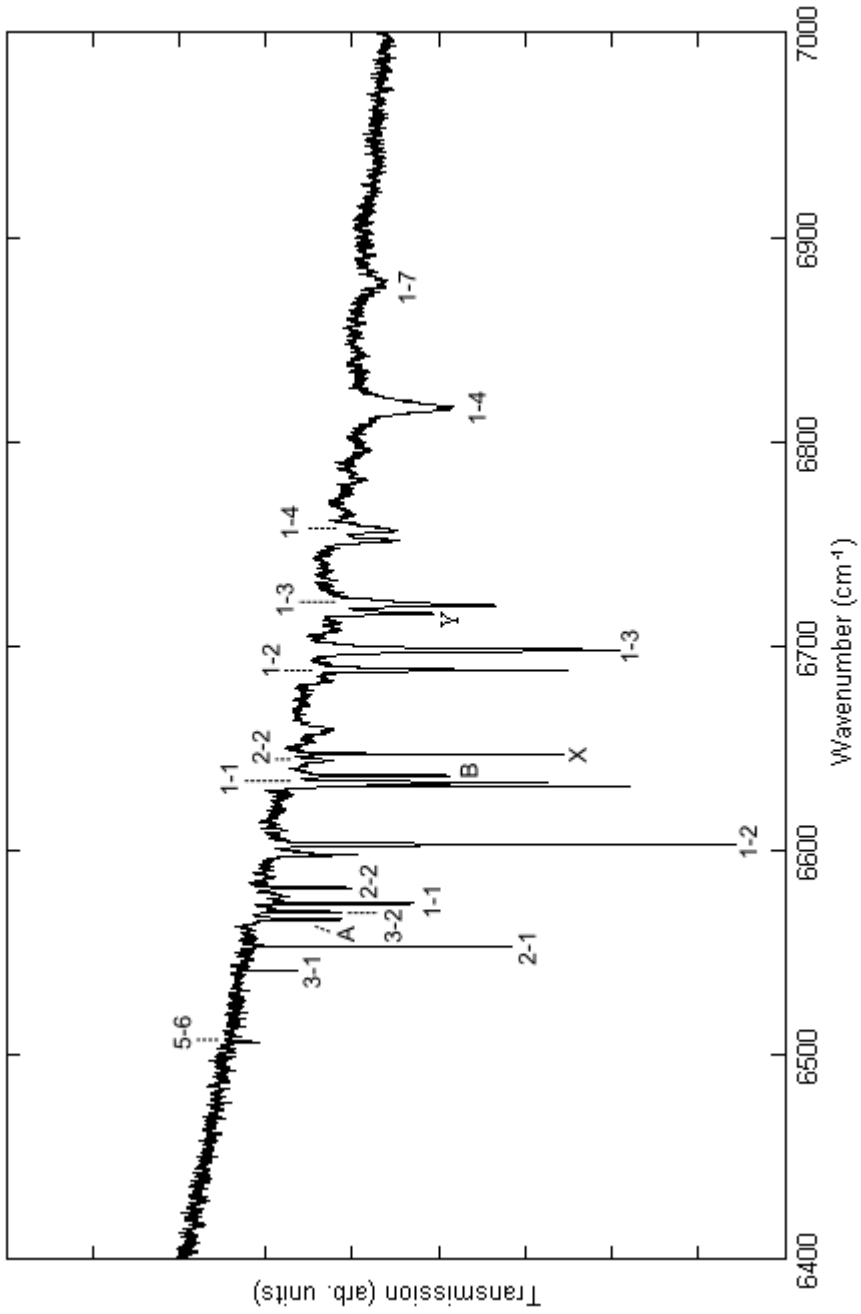

Figure 4-1: FTIR $CaF_2:Er^{3+}$ spectra at 13 K with transitions assigned. Notation is A-B denoting $Z_A \rightarrow Y_B$, with C_{4v} symmetry sites labelled below the line, and C_{3v} symmetry sites labelled above the line. Transitions denoted by A and B are from the minority G1 C_{3v} site, and are assigned A= $Z_2\ \gamma_{5,6} \rightarrow Y_2\ \gamma_{5,6}$ and B=$Z_2\ \gamma_{5,6} \rightarrow Y_3\ \gamma_4$. The transitions denoted X and Y are assumed to be from impurities.

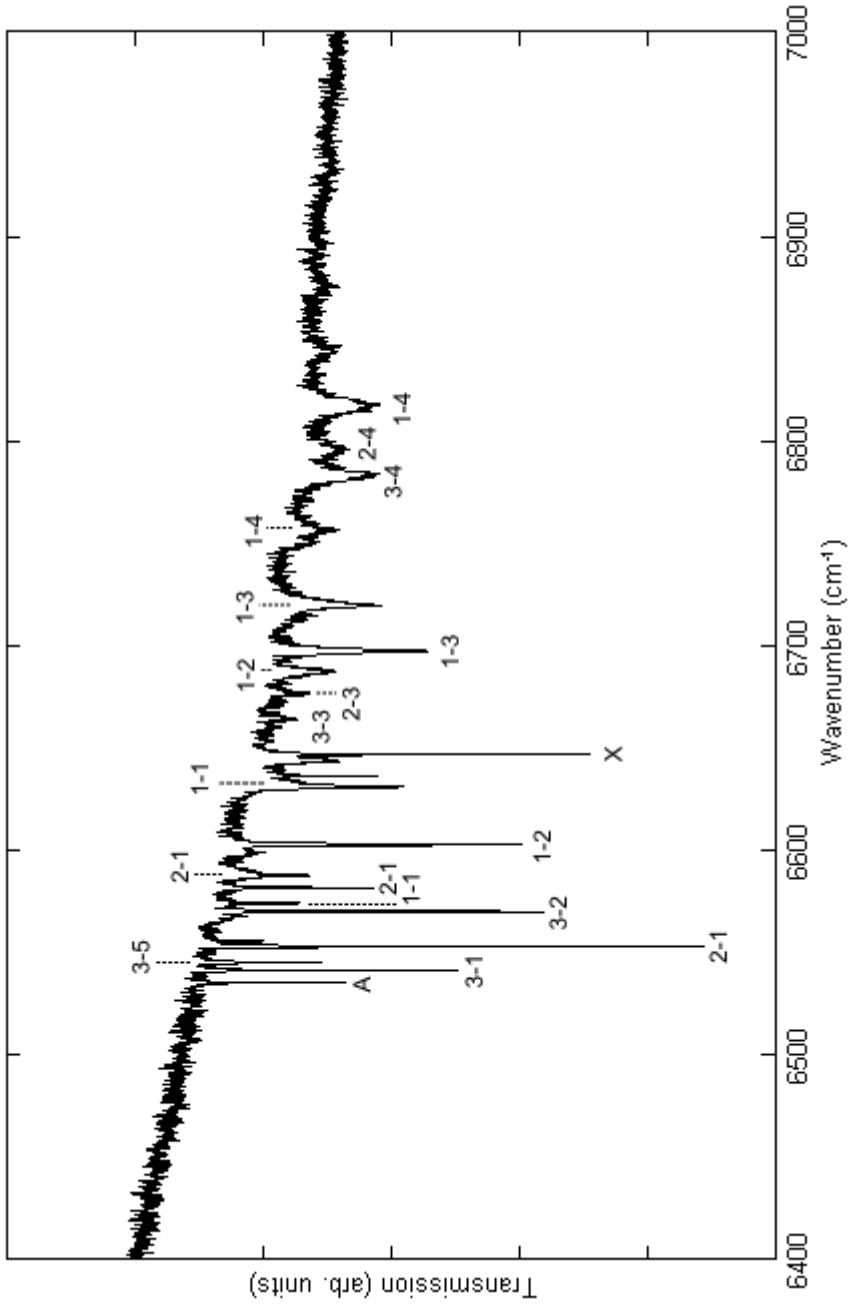

Figure 4-2: FTIR CaF_2:Er^{3+} spectra at 70 K with transitions assigned. Notation is A-B denoting $Z_A \rightarrow Y_B$, with C_{4v} symmetry sites labelled below the line, and C_{3v} symmetry sites labelled above the line. The transition denoted by A is from the minority G1 C_{3v} site, and is assigned $Z_2\ \gamma_{5,6} \rightarrow Y_1\ \gamma_4$. The transition denoted X is assumed to be from impurities.

Transition	Line position	Energy	Linewidth
$Z_1\,\gamma_7 \rightarrow Y_2\,\gamma_7\ C_{4v}$	6603	6603.5	0.7
$Z_1\,\gamma_7 \rightarrow Y_3\,\gamma_7\ C_{4v}$	6698	6699	1.7
$Z_2\,\gamma_6 \rightarrow Y_1\,\gamma_6\ C_{4v}$	6553	6553	0.3
$Z_2\,\gamma_6 \rightarrow Y_2\,\gamma_7\ C_{4v}$	6582	6582.4	0.4
$Z_3\,\gamma_7 \rightarrow Y_1\,\gamma_6\ C_{4v}$	6542	6541	0.3
$Z_3\,\gamma_7 \rightarrow Y_2\,\gamma_7\ C_{4v}$	6570	6570.4	0.3
$Z_1\,\gamma_4 \rightarrow Y_1\,\gamma_4\ C_{3v}$	6632	6629.2	0.7
$Z_1\,\gamma_4 \rightarrow Y_2\,\gamma_{5,6}\ C_{3v}$	6688	6686	1.0

Table 4-1: Linewidths and line positions of the transitions studied in this chapter, given at 12 K. Line position is compared with transition energies, obtained from the energy levels of *Cockroft et al* [20] for the C_{3v} symmetry sites and *Freeth et al* [38] for the C_{4v} symmetry sites. All parameters have units of wavenumbers (cm^{-1}).

The transitions studied in detail in this chapter are given in table 4.1, with values given at 12 K. The other transitions are not studied as they are not intense enough at a large enough temperature range to differentiate from the noise.

There is good agreement between the 12 K spectra used in this work and the transitions calculated from the energy levels determined by Cockroft *et al* [20] and Freeth *et al* [38]. This indicates that the transition assignments of the hot transitions are in agreement with this earlier work.

4.3 Crystal Field Analysis

Both *Cockroft et al* [20] and *Freeth et al* [38] have done work on the crystal field of Er^{3+} doped CaF_2, in C_{3v} and C_{4v} site symmetry respectively. The crystal field parameters used in these papers was used as the basis for crystal field calculations in this work, although the other parameters were varied to improve the fit.

Parameter	Value	Parameter	Value
F^2	97483	T^6	[-271]
F^4	67904	T^7	[308]
F^6	54010	T^8	[299]
α	17.79	M^0	[3.86]
β	-582.1	M^2	0.56 M^0
γ	18000	M^4	0.31 M^0
T^2	[400]	P^2	[594]
T^3	[43]	P^4	0.5 P^2
T^4	[73]	P^6	0.1 P^2

Table 4-2: Hamiltonian parameters obtained from crystal field analysis of CaF_2:Er^{3+}, for both the C_{3v} and C_{4v} symmetry sites, in units of cm^{-1}. Parameters in brackets were obtained from *Carnall et al* [28] from LaF_3:Er^{3+}.

There is good agreement between the theoretical energy levels in the C_{4v} site, obtained from the crystal field calculations, and the experimental energy levels measured by Freeth et al (see table 4.5 below). There are larger differences between the $^4I_{15/2}$ calculated and experimental enerergy levels than the $^4I_{13/2}$ levels. This is likely due to the small number of parameters which were varied, meaning that the small differences between CaF_2 and LaF_3 as a host lattice are not accounted for.

Parameter	C_{4v}	C_{3v}
B_A^2	608.83	140.6
B_A^4	7366.5	-292.6
B_A^6	355.27	-300.1
$B_A^{6\prime}$	-	-513.5
B_C^4	-1662.65	112.1
B_C^6	502.28	581.6
ζ	2371.7	2378.8

Table 4-3: Hamiltonian parameters obtained from crystal field analysis of CaF_2:Er^{3+}, in either a C_{3v} or C_{4v} symmetry site, in units of cm^{-1}. The crystal field parameters for the C_{4v} site were obtained from *Freeth et al* [38], while the crystal field parameters for the C_{3v} were obtained from *Cockroft et al* [20]. The ζ values were varied to conform to the experimental spectra.

Multiplet	Label	Irrep	$E_{observed}$	E_{calc}
$^4I_{13/2}$	Y_7	γ_7	6878.7	6876.4
	Y_6	γ_6	6842.7	6841.9
	Y_5	γ_6	6816.9	6818.2
	Y_4	γ_7		6815.1
	Y_3	γ_7	6699	6698.1
	Y_2	γ_7	6603.5	6602.7
	Y_1	γ_6	6574.1	6575.4
$^4I_{15/2}$	Z_8	γ_6	563	566.5
	Z_7	γ_7	452.2	452.2
	Z_6	γ_6	436	437.8
	Z_5	γ_7	404.6	401.4
	Z_4	γ_6	231.5	233.4
	Z_3	γ_7	33.1	34.3
	Z_2	γ_6	21.1	21.9
	Z_1	γ_7	0	0

Table 4-4: Calculated and observed energy levels of Er^{3+}: CaF_2 in C_{4v} symmetry. The observed energy levels are from *Freeth et al* [38] and the calculated energy levels are from this thesis, both with units of cm^{-1}.

The C_{3v} symmetry site had some variation in the agreement between the calculated and the experimental energy levels derived by Cockroft et al (see table 4.6 below). This was likely due to slight variations in the differences between the non-crystal field parameters in the C_{3v} and C_{4v} sites, most of which were taken to be identical, and differences between CaF_2 and LaF_3 as a host lattice.

Multiplet	Label	Irrep	$E_{observed}$	E_{calc}
$^4I_{13/2}$	Y_7	γ_4	6816	6816
	Y_6	γ_4	6779	7690
	Y_5	$\gamma_{5,6}$	6774	6773
	Y_4	γ_4	6754	6754
	Y_3	γ_4	6718	6728
	Y_2	$\gamma_{5,6}$	6686	6687
	Y_1	γ_4	6629.2	6633
$^4I_{15/2}$	Z_8	$\gamma_{5,6}$	461	436
	Z_7	γ_4	385	384
	Z_6	γ_4	342	353
	Z_5	$\gamma_{5,6}$	272	251
	Z_4	γ_4	261	240
	Z_3	$\gamma_{5,6}$	227	218
	Z_2	γ_4	43.5	42
	Z_1	γ_4	0	0

Table 4-5: Calculated and observed energy levels of Er^{3+}: CaF_2 in C_{3v} symmetry B centre. The observed energy levels are from *Cockroft et al* [20] and the calculated energy levels are from this thesis, both with units of cm^{-1}.

4.4 Simulated Spectra

Using the calculated energies in section 4.3, spectra were able to be simulated. Intensities were simulated using magnetic dipole intensity calculations, giving delta functions. These were then converted into Lorentzian line shapes by convoluting the delta functions with a Lorentzian. A Voigt line shape simulated spectra was created, but analysis showed little difference between the Voigt and the Lorentzian spectra. These spectra are specific to the site symmetry, although by adding both the C_{3v} and the C_{4v} site spectra together a spectra of the entire series may be obtained.

The simulated spectra, like the experimental spectra it models, is temperature dependent, requiring the linewidths from the experimental spectra at that temperature in order to give the correct line shape. Unfortunately it was not possible to use experimentally measured linewidths

for all the transitions, so for some of the transitions the linewidths were estimated by what gave a lineshape and intensity in agreement with the experimental spectra instead.

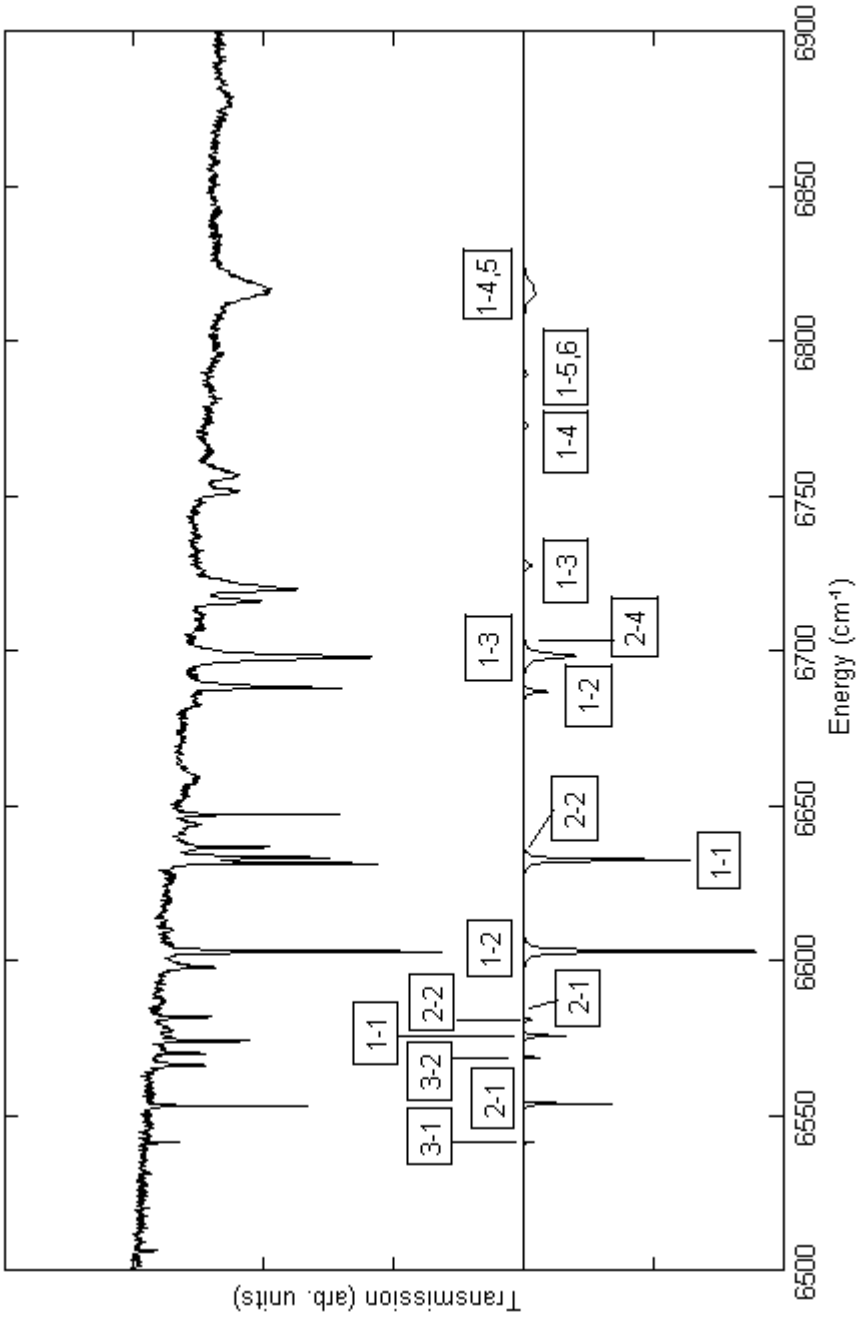

Figure 4-3: Experimental (top) and simulated (bottom) spectra of $CaF_2:Er^{3+}$ at 13 K. Transitions are labeled $Z_A \rightarrow Y_B$ as A-B. The C_{4v} transitions are labeled above the simulated spectra while the C_{3v} transitions are labeled below the simulated spectra. Unlabeled transitions were not significant in the simulated spectra.

There is good agreement between most of the relative intensities and linewidths for the C_{4v} sites. This is complicated by the fact that the $Z_1\ \gamma_7 \rightarrow Y_4\ \gamma_7$ and the $Z_1\ \gamma_7 \rightarrow Y_5\ \gamma_6$ transitions are both very close to one another, making it very difficult to distinguish between the peaks, meaning that the parameters for these peaks are much less certain than for the other transitions.

There was also good agreement for the C_{3v} site with the main discrepancy between the experimental and simulated spectra being the overestimation of the $Z_1\,\gamma_4 \rightarrow Y_1\,\gamma_4$ transition in the simulated spectra.

Temperature	FWHM							
70K		Y_1	Y_2	Y_3	Y_4	Y_5	Y_6	Y_7
	Z_1	0.51	0.89	2.33	4 *	4 *	6.76	-
	Z_2	0.53	0.55	3 *	3.7	3.7	-	-
	Z_3	0.42	0.55	4.3	3.5	2.5	-	-
13K		Y_1	Y_2	Y_3	Y_4	Y_5	Y_6	Y_7
	Z_1	0.5 *	0.70	1.8	4 *	4 *	-	-
	Z_2	0.33	0.66	-	-	-	-	-
	Z_3	0.27	0.28	-	-	-	-	-

Table 4-6: Full widths at half maximum (FWHM) for the transitions for the $CaF_2:Er^{3+}$ in C_{4v} site symmetry for the simulated spectra shown in figures 4.3 and 4.4. All units are in cm^{-1}. Parameters marked * are estimated, transitions with parameters marked - were not significant enough to be noticeable; the other parameters were obtained from the experimental spectra. Transitions not in this table were also not significant enough to be noticeable.

Temperature	FWHM							
70K		Y_1	Y_2	Y_3	Y_4	Y_5	Y_6	Y_7
	Z_1	2.11	3.58	3.39	5.24	2 *	2 *	2 *
	Z_2	2.76	3 *	4 *	2 *	3 *	3 *	-
13K		Y_1	Y_2	Y_3	Y_4	Y_5	Y_6	Y_7
	Z_1	0.71	1.03	1.5 *	3.72	2 *	2 *	-
	Z_2	0.53	3 *	-	4 *	-	-	-

Table 4-7: Full widths at half maximum (FWHM) for the transitions for the $CaF_2:Er^{3+}$ in C_{3v} site symmetry for the simulated spectra shown in figures 4.3 and 4.4. All units are in cm^{-1}. Parameters marked * are estimated, transitions with parameters marked - were not significant enough to be noticeable; the other parameters were obtained from the experimental spectra. Transitions not in this table were also not significant enough to be noticeable.

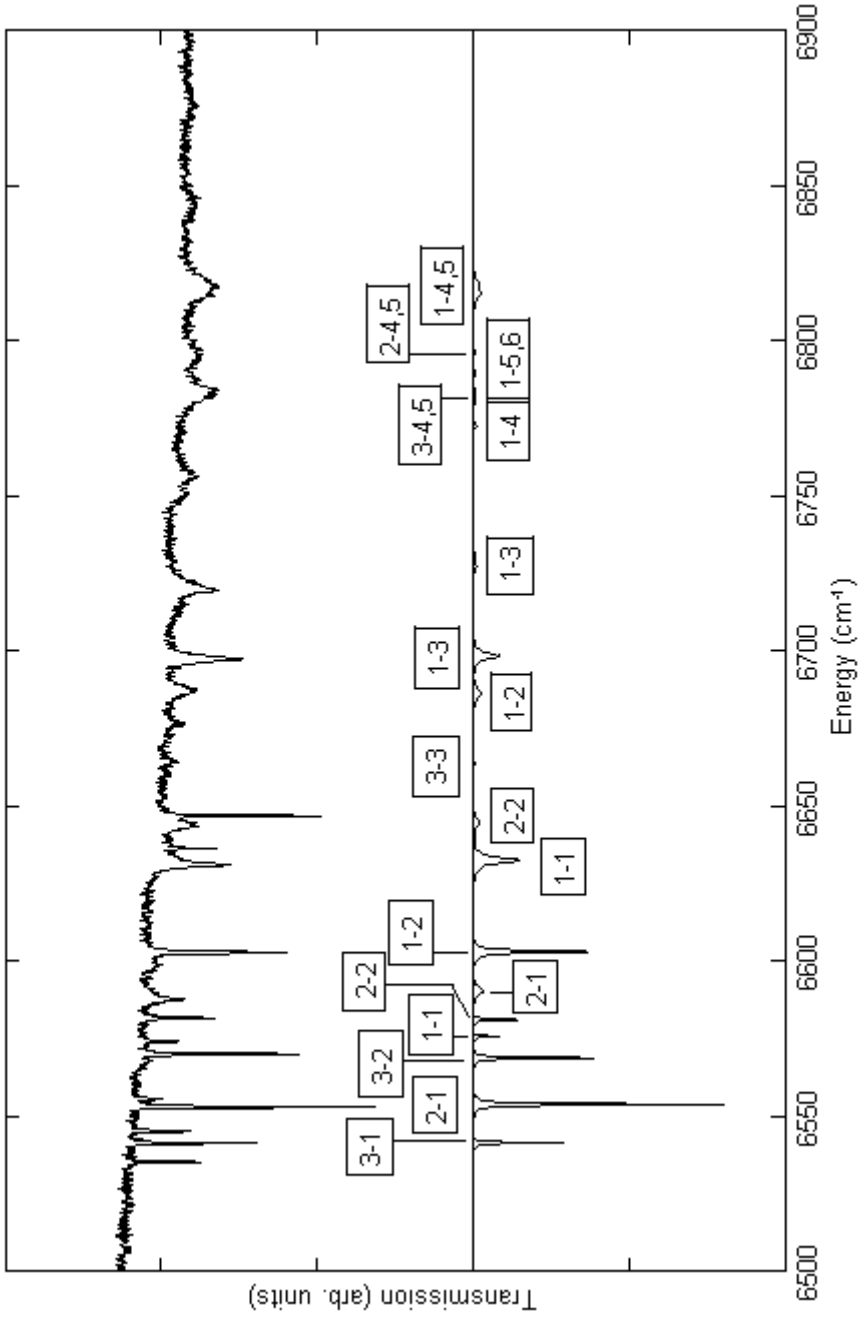

Figure 4-4: Experimental (top) and simulated (bottom) spectra of CaF_2:Er^{3+} at 70 K. Transitions are labeled $Z_A \rightarrow Y_B$ as A-B. The C_{4v} transitions are labeled above the simulated spectra while the C_{3v} transitions are labeled below the simulated spectra. Unlabeled transitions were not significant in the simulated spectra.

Much like the 13 K simulated spectra, in the 70 K simulated spectra the relative positions and intensities of many of the C_{4v} transitions accord well with the experimentally derived spectra. Some of the smaller features on the experimental spectra, such as the $Z_3\ \gamma_7 \rightarrow Y_4\ \gamma_7$ and $Z_2\ \gamma_6 \rightarrow Y_4\ \gamma_7$ transitions, are much smaller in the simulated spectra relative to the surrounding transitions than expected. With the C_{3v} the discrepancies between the simulated and the

experimental spectra are once again the overestimation of the $Z_1\ \gamma_4 \rightarrow Y_1\ \gamma_4$ transition relative to the other C_{3v} transitions and at 70 K also the lack of the $Z_3\ \gamma_{5,6} \rightarrow Y_6\ \gamma_4$ transition in the model.

4.5 Temperature Dependent Linewidth Analysis

The $CaF_2:Er^{3+}$ was analysed by first applying a line-shape to the spectral data, giving the experimental linewidth that to be analysed. The theoretical models were firstly done using just the inhomogeneous and the Raman terms. This, however, did not accurately fit the data in all cases. In the specific case of the $Z_1\ \gamma_7 \rightarrow Y_2\ \gamma_7$, $Z_3\ \gamma_7 \rightarrow Y_1\ \gamma_6$ and $Z_2\ \gamma_6 \rightarrow Y_1\ \gamma_6$ C_{4v} transitions the simplified model works to a good approximation, but in the other transitions, the model was found to be too simplistic. Therefore the direct phonon transitions have to be invoked in order for the model to match the data series.

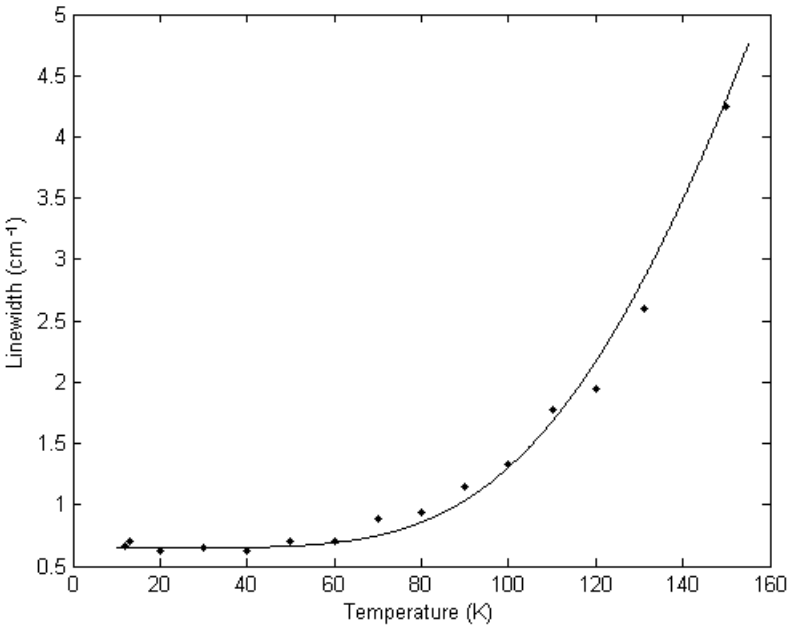

Figure 4-5: Fitted curve to the linewidth of the $CaF_2:Er^{3+}$ $Z_1\ \boldsymbol{\gamma_7} \rightarrow Y_2\ \boldsymbol{\gamma_7}$ transition in C_{4v} point symmetry using only inhomogeneous and Raman scattering terms. This is a good approximation for this transition.

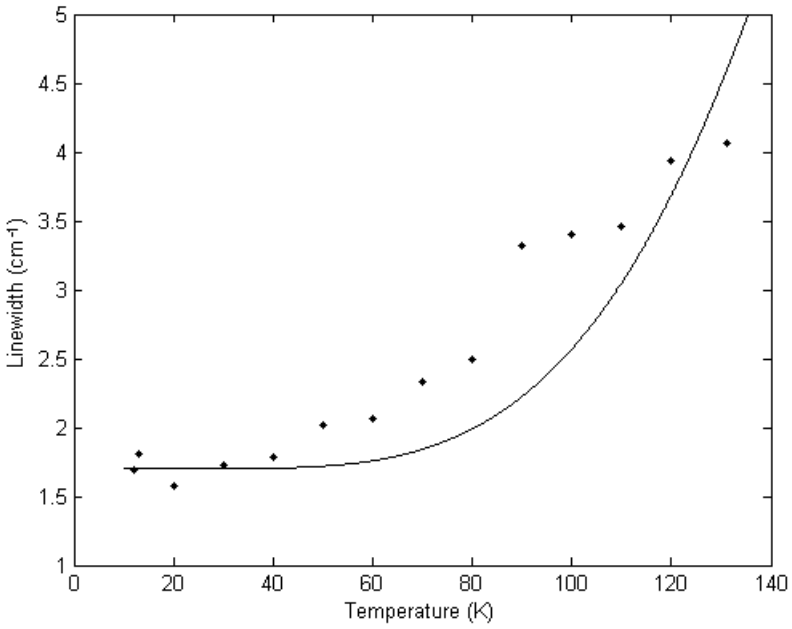

Figure 4-6: Fitted curve to the linewidth of the CaF_2:Er^{3+} Z_1 $\boldsymbol{\gamma_7}$ → Y_3 $\boldsymbol{\gamma_7}$ transition in C_{4v} point symmetry, using only inhomogeneous and Raman scattering terms. This is not a good approximation for this transition.

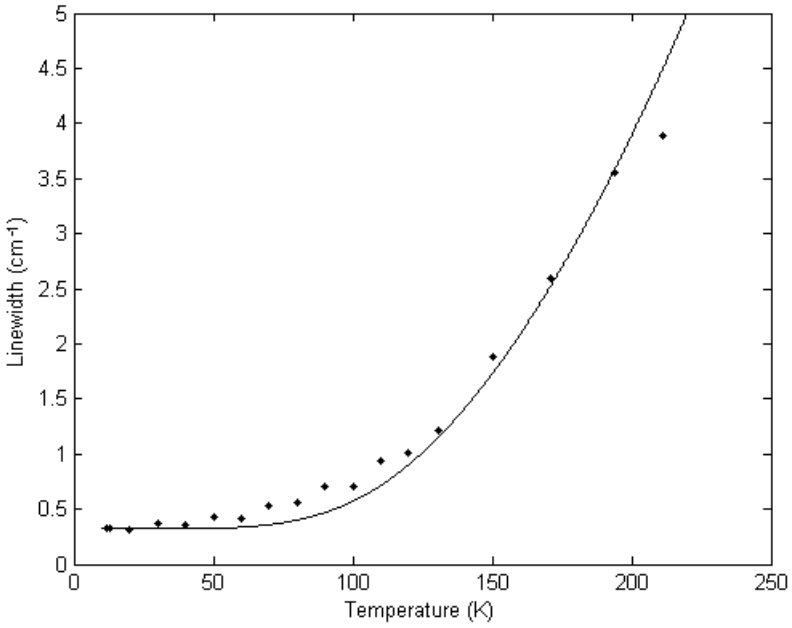

Figure 4-7: Fitted curve to the linewidth of the CaF_2:Er^{3+} Z_2 $\boldsymbol{\gamma_6}$ → Y_1 $\boldsymbol{\gamma_6}$ transition in C_{4v} point symmetry, using only inhomogeneous and Raman scattering terms. This is a good approximation for this transition.

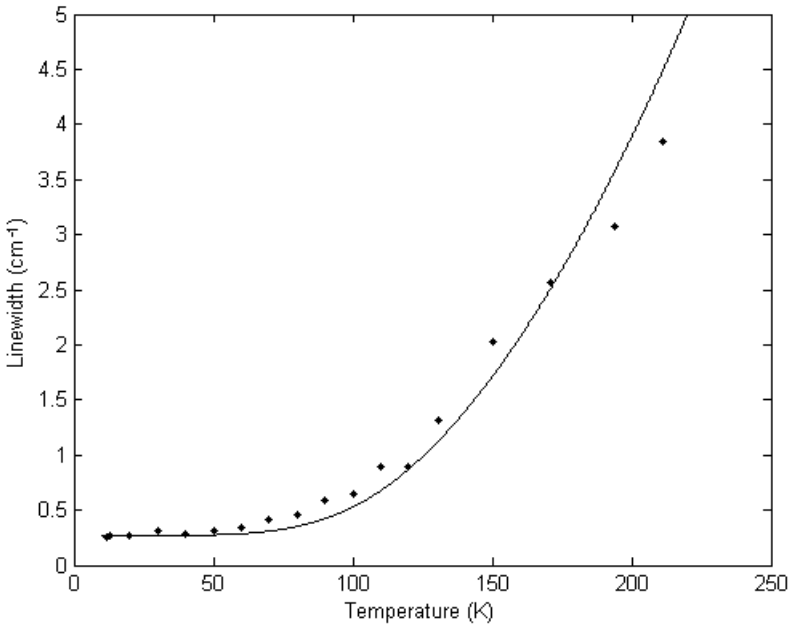

Figure 4-8: Fitted curve to the linewidth of the CaF_2:Er^{3+} Z_3 $\boldsymbol{\gamma_7}$ → Y_1 $\boldsymbol{\gamma_6}$ transition in C_{4v} point symmetry, using only inhomogeneous and Raman scattering terms. This is a good approximation for this transition.

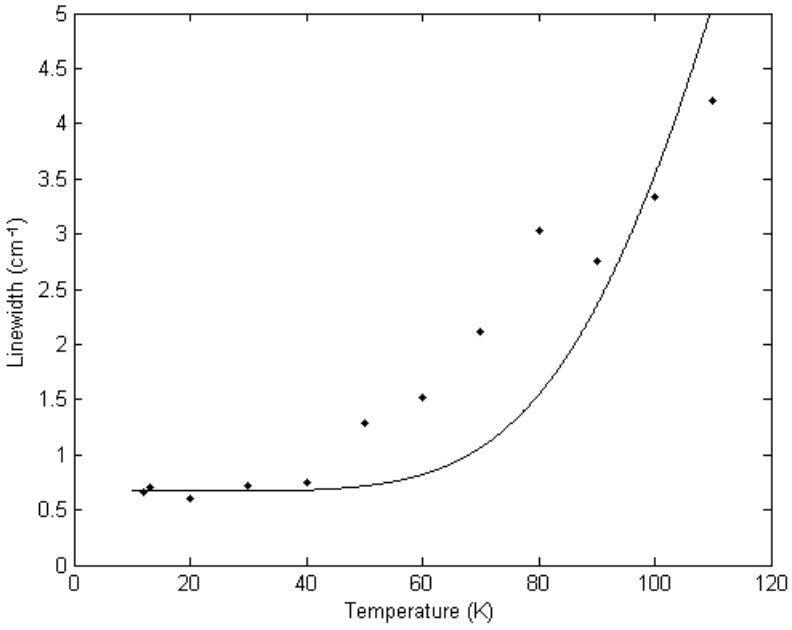

Figure 4-9: Fitted curve to the linewidth of the CaF_2:Er^{3+} Z_1 $\boldsymbol{\gamma_4}$ → Y_1 $\boldsymbol{\gamma_4}$ transition in C_{3v} point symmetry, using only inhomogeneous and Raman scattering terms. This is not a good approximation for this transition.

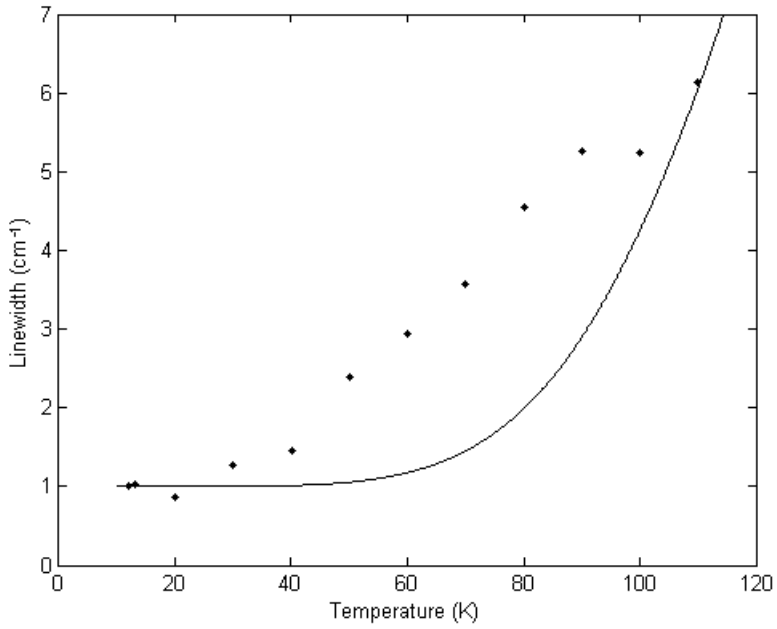

Figure 4-10: Fitted curve to the linewidth of the CaF_2:Er^{3+} Z_1 $\boldsymbol{\gamma_4}$ → Y_2 $\boldsymbol{\gamma_{5,6}}$ transition in C_{3v} point symmetry, using only inhomogeneous and Raman scattering terms. This is not a good approximation for this transition.

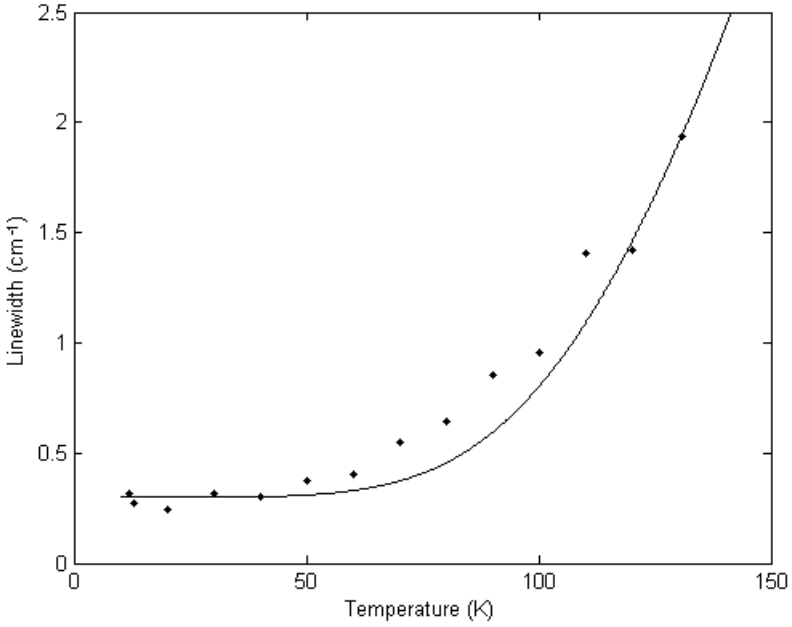

Figure 4-11: Fitted curve to the linewidth of the CaF_2:Er^{3+} Z_3 $\boldsymbol{\gamma_7}$ → Y_2 $\boldsymbol{\gamma_7}$ transition in C_{4v} point symmetry, using only inhomogeneous and Raman scattering terms. This is not a good approximation for this transition.

To account for the discrepancies between the models and the data, fitting was redone with one-phonon direct absorption and emission processes included. Although it may have been possible to use some of the fits, for consistency all of the fits were redone with direct one-phonon processes. To avoid overparameterization the nearest electronic states were focused on, although if these were inadequate to explain the curve then more distant states were considered.

Even so, in some cases multiple direct one-phonon processes were needed to account for the linewidth.

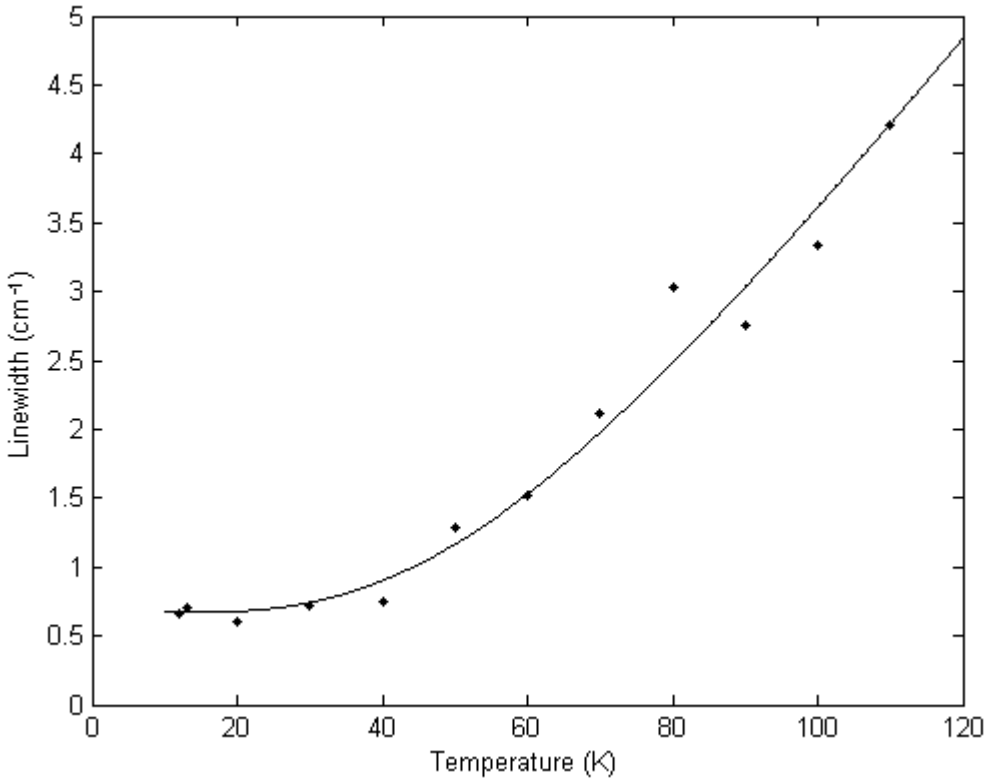

Figure 4-12: The final fitted function for the linewidth for the CaF_2:Er^{3+} Z_1 $\boldsymbol{\gamma_4}$ → Y_1 $\boldsymbol{\gamma_4}$ transition in C_{3v} point symmetry.

Figure 4.12 shows the $Z_1\,\gamma_4 \rightarrow Y_1\,\gamma_4$ transition in C_{3v} symmetry. This fit relies only on the inhomogeneous component and a direct single phonon absorption term from $Y_1\,\gamma_4 \rightarrow Y_3\,\gamma_4$. The lack of a term for Raman scattering indicates that, for the temperature range investigated, single phonon interactions dominate, with two-phonon processes such as Raman scattering not yet becoming significantly established. This is within reasonable expectation for the temperature range in question, as Raman scattering tends to dominate at higher temperatures.

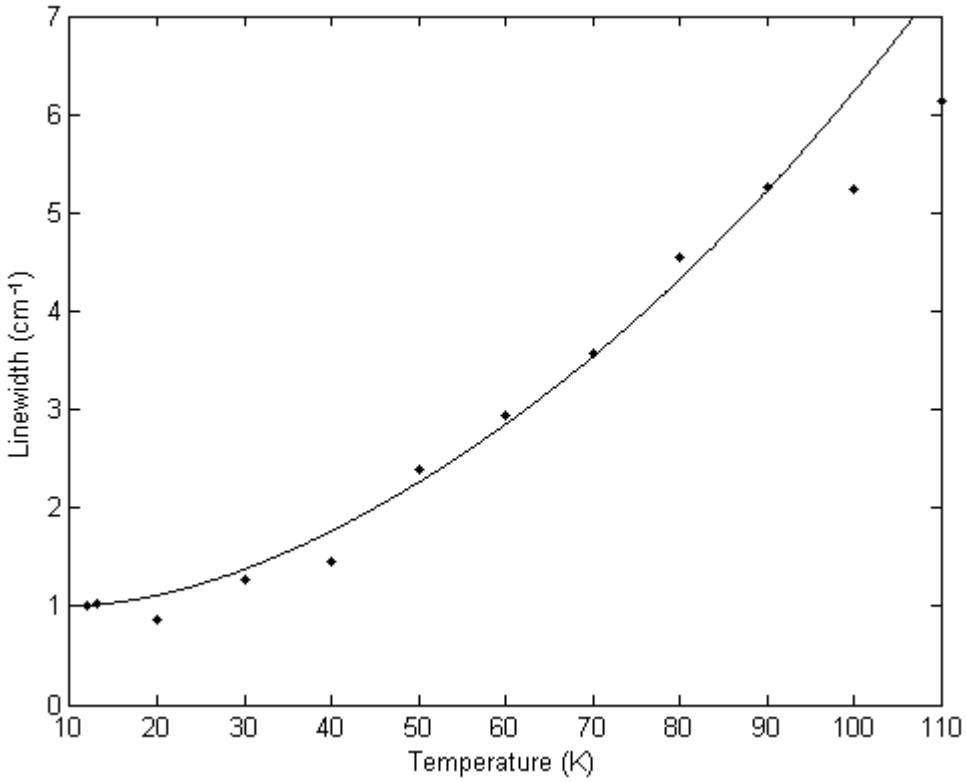

Figure 4-13: The final fitted function for the linewidth for the CaF_2:Er^{3+} Z_1 $\boldsymbol{\gamma_4}$ → Y_2 $\boldsymbol{\gamma_{5,6}}$ transition in C_{3v} point symmetry.

The Z_1 γ_4 → Y_2 $\gamma_{5,6}$ C_{3v} transition, shown in figure 4.13, relies on the inhomogeneous component, on the Raman process and a direct single phonon absorption term from Z_1 γ_4 → Z_2 γ_4. The fit from 20K to 50K suggests that there are other direct processes involved, although the contribution from these components is small compared to the Z_1 γ_4 → Z_2 γ_4 contribution. The contribution due to Raman scattering is small on this temperature range, only surpassing the inhomogeneous component at 100K, and not surpassing the direct process at all in this range.

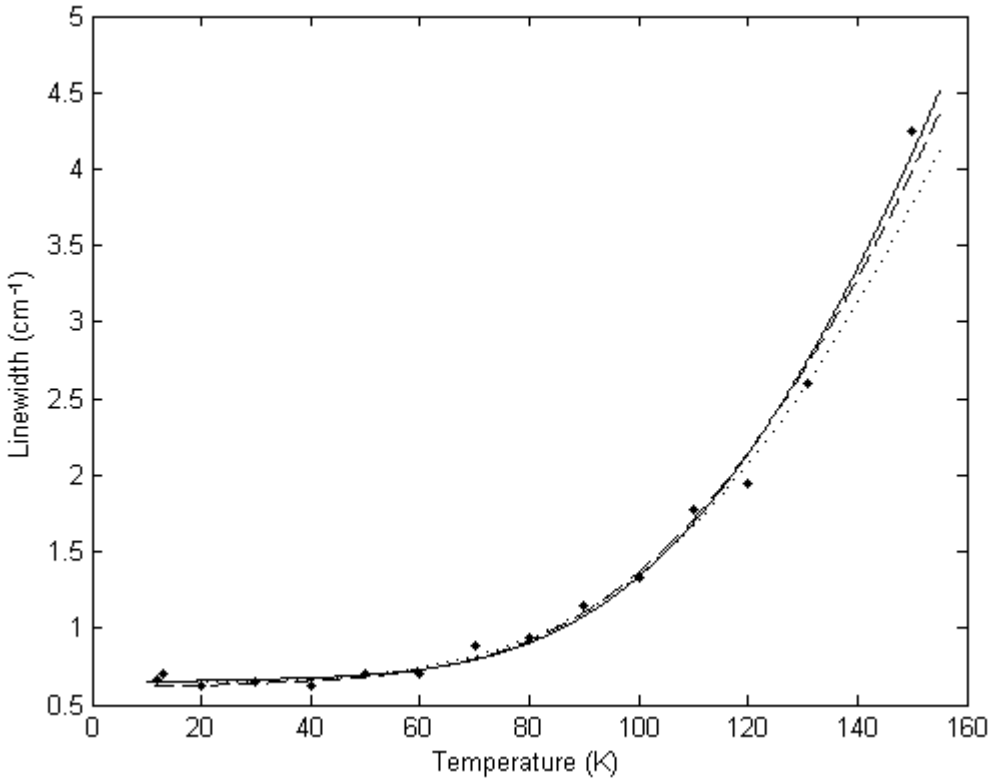

Figure 4-14: The final fitted function for the linewidth for the CaF_2:Er^{3+} Z_1 $\boldsymbol{\gamma_7} \rightarrow$ Y_2 $\boldsymbol{\gamma_7}$ transition in C_{4v} point symmetry. All fits involve Raman scattering and direct one-phonon processes. The solid line is broadened by Z_1 $\boldsymbol{\gamma_7} \rightarrow Z_2$ $\boldsymbol{\gamma_6}$ direct absorption, the dotted line is broadened by Y_2 $\boldsymbol{\gamma_7} \rightarrow Y_3$ $\boldsymbol{\gamma_7}$ direct absorption and the dashed line is broadened by Y_2 $\boldsymbol{\gamma_7} \rightarrow Y_1$ $\boldsymbol{\gamma_6}$ direct emission.

For the Z_1 $\gamma_7 \rightarrow Y_2$ γ_7 C_{4v} transition, shown in figure 4.14, there is very little difference between the linewidth as a result of any of three one-phonon direct processes in this range. It is apparent that one direct process is dominant, however there is insufficient evidence to exclude any of these processes. In each of these cases the coupling constant associated with Raman scattering is about 400 cm^{-1}. This illustrates how little effect direct processes have on this transition.

For the Z_2 $\gamma_6 \rightarrow Y_1$ γ_6 C_{4v} transition, shown in figure 4.15, there is a similar situation, with three possible direct processes. In this case the coupling constant associated with Raman scattering is about 140 cm^{-1} for each of the possible fits, showing that once again direct processes are very minor compared with Raman scattering.

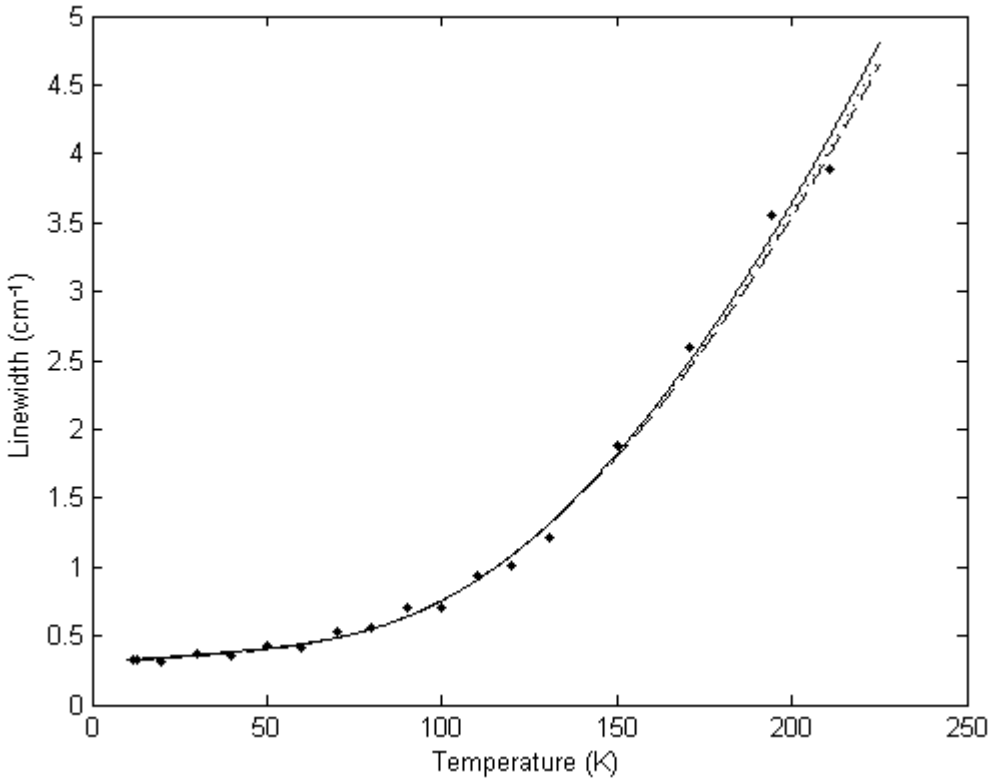

Figure 4-15: The final fitted function for the linewidth for the CaF_2:Er^{3+} Z_2 $\boldsymbol{\gamma_6}$ → Y_1 $\boldsymbol{\gamma_6}$ transition in C_{4v} point symmetry. All fits involve Raman scattering and direct one-phonon processes. The solid line is broadened by Z_2 $\boldsymbol{\gamma_6}$ → Z_3 $\boldsymbol{\gamma_7}$ direct absorption, the dotted line is broadened by Z_2 $\boldsymbol{\gamma_6}$ → Z_1 $\boldsymbol{\gamma_7}$ direct emission and the dashed line is broadened by Y_1 $\boldsymbol{\gamma_6}$ → Y_2 $\boldsymbol{\gamma_7}$ direct absorption.

The Z_3 γ_7 → Y_2 γ_6 C_{4v} transition, shown in figure 4.16, relies on inhomogeneous broadening and single phonon emission at low temperatures. This is due to the temperature independent component of the emission. At higher temperatures, the Raman process dominates the direct emission significantly, starting at approximately 90 K.

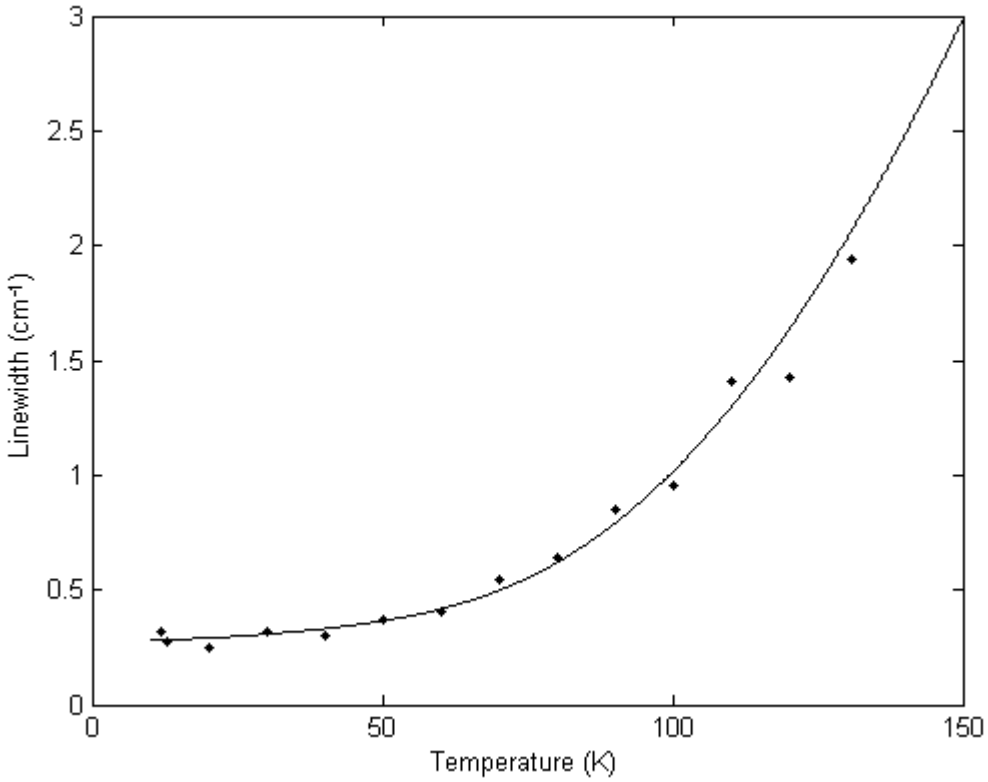

Figure 4-16: The final fitted function for the linewidth for the CaF_2:Er^{3+} Z_3 $\boldsymbol{\gamma_7}$ → Y_2 $\boldsymbol{\gamma_7}$ transition in C_{4v} point symmetry.

The Z_3 γ_7 → Y_1 γ_6 C_{4v} transition, shown in figure 4.17, relies on the inhomogeneous component, on the Raman process and on two direct single phonon absorption terms from Z_3 γ_7 → Z_4 γ_6 and from Y_1 γ_6 → Y_2 γ_7. The most significant component is the Raman scattering, although at low temperatures the inhomogeneous component is the most significant, with the Y_1 γ_6 → Y_2 γ_7 absorption also being significant. The Z_3 γ_7 → Z_4 γ_6 direct absorption becomes more significant than either the inhomogeneous or the Y_1 γ_6 → Y_2 γ_7 only at temperatures in excess of 150 K, although it is never more than a small component of the total linewidth.

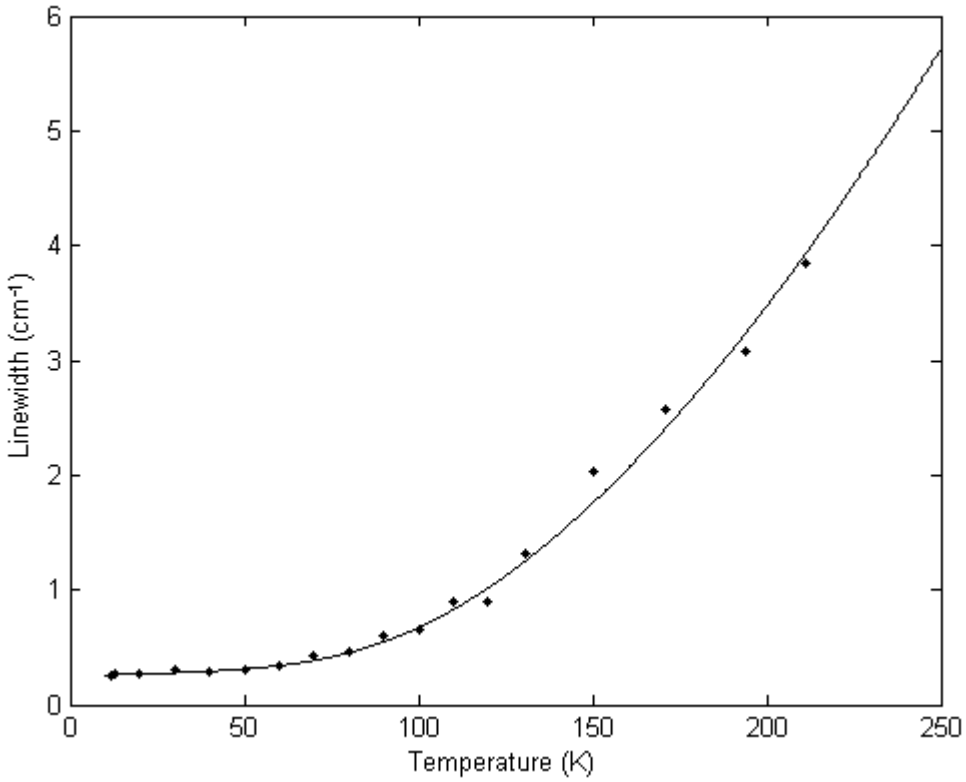

Figure 4-17: The final fitted function for the linewidth for the CaF_2:Er^{3+} Z_3 $\boldsymbol{\gamma_7}$ → Y_1 $\boldsymbol{\gamma_6}$ transition in C_{4v} point symmetry.

For the Z_1 γ_7 → Y_3 γ_7 C_{4v} transition, shown in figure 4.18, there are two possible fits. One relies on the inhomogeneous component and the Y_3 γ_7 → Y_4 γ_7 absorption process only, the other relying on the inhomogeneous component, the Z_1 γ_7 → Z_2 γ_6 direct absorption and Raman scattering. This latter fit is not as good, but still provides a reasonable fit whilst not completely neglecting Raman scattering. This is considered as no other fits in the C_{4v} symmetry site have zero Raman scattering and the associated coupling constant is of the same order as the rest of the series.

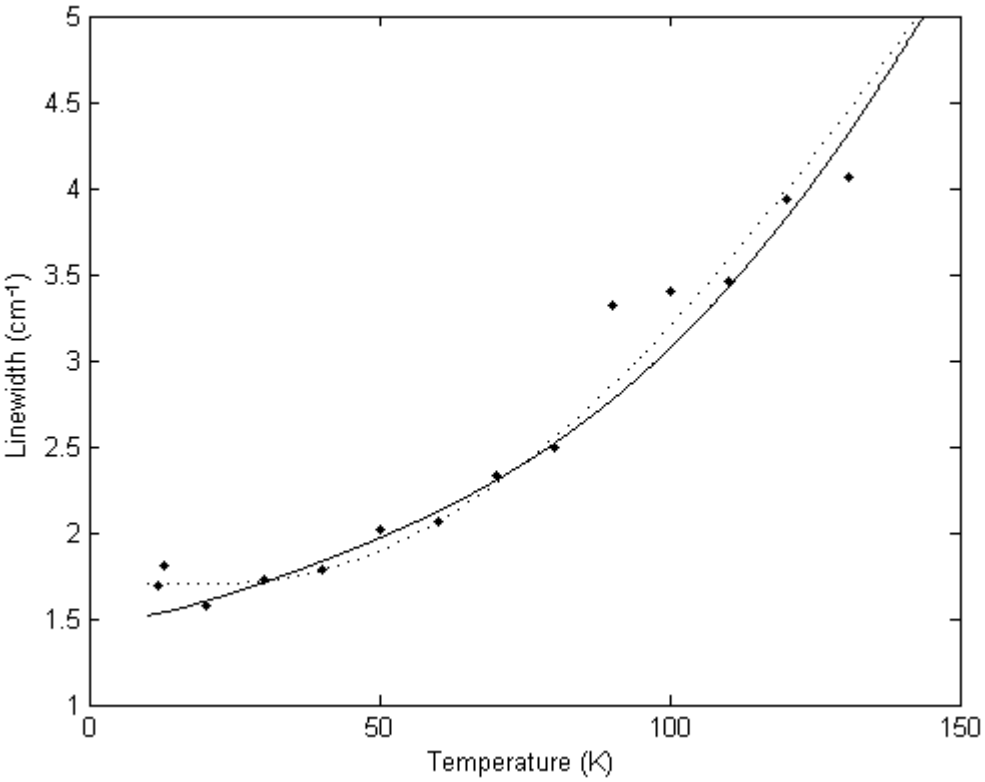

Figure 4-18: The fitted functions for the linewidth for the CaF_2:Er^{3+} Z_1 $\boldsymbol{\gamma_7}$ → Y_3 $\boldsymbol{\gamma_7}$ transition in C_{4v} point symmetry. The solid line is broadened by Raman scattering and Z1 $\boldsymbol{\gamma_7}$ → Z_2 $\boldsymbol{\gamma_6}$ direct absorption, the dotted line is broadened by Y_3 $\boldsymbol{\gamma_7}$ → Y_4 $\boldsymbol{\gamma_7}$ direct absorption without Raman scattering.

	Inhomogeneous	Raman	Single Phonon Direct			Fit
Transition	Inh (cm^{-1})	α (cm^{-1})	Transition	Energy (cm-1)	β (cm^{-1})	σ
$Z_1\,\gamma_7 \rightarrow Y_2\,\gamma_7$ C_{4v}	0.55	390	$Y_2\,\gamma_7 \rightarrow Y_1\,\gamma_6$	29.4	0.12	0.01
	0.65	340	$Y_2\,\gamma_7 \rightarrow Y_3\,\gamma_7$	95.5	1	0.02
	0.65	430	$Z_1\,\gamma_7 \rightarrow Z_2\,\gamma_6$	21.1	0.05	0
$Z_1\,\gamma_7 \rightarrow Y_3\,\gamma_7$ C_{4v}	1.5	230	$Z_1\,\gamma_7 \rightarrow Z_2\,\gamma_6$	21.1	0.65	0.03
	1.7	0	$Y_3\,\gamma_7 \rightarrow Y_4\,\gamma_7$	117.9	10	0.01
$Z_2\,\gamma_6 \rightarrow Y_1\,\gamma_6$ C_{4v}	0.32	135	$Y_1\,\gamma_6 \rightarrow Y_2\,\gamma_7$	29.4	0.18	0.01
	0.26	140	$Z_2\,\gamma_6 \rightarrow Z_1\,\gamma_7$	21.1	0.1	0.01
	0.32	145	$Z_2\,\gamma_6 \rightarrow Z_3\,\gamma_7$	12.0	0.06	0
$Z_3\,\gamma_7 \rightarrow Y_1\,\gamma_6$ C_{4v}	0.26	110	$Z_3\,\gamma_7 \rightarrow Z_4\,\gamma_6$	198.4	2.5	0.02
			$Y_1\,\gamma_6 \rightarrow Y_2\,\gamma_7$	29.4	0.1	
$Z_3\,\gamma_7 \rightarrow Y_2\,\gamma_6$ C_{4v}	0.14	270	$Z_3\,\gamma_7 \rightarrow Z_1\,\gamma_7$	227.0	0.21	0.02
$Z_1\,\gamma_4 \rightarrow Y_1\,\gamma_4$ C_{3v}	0.67	0	$Y_1\,\gamma_4 \rightarrow Y_3\,\gamma_{5,6}$	124.9	9	0
$Z_1\,\gamma_4 \rightarrow Y_2\,\gamma_{5,6}$ C_{3v}	1	500	$Z_1\,\gamma_4 \rightarrow Z_2\,\gamma_4$	21.1	4.4	0.06

Table 4-8: Parameters used in the fitting functions for the temperature dependence of the linewidths. Inh is the inhomogeneous component of the linewidth, α the coupling constant associated with Raman scattering, the direct transition indicates the direct phonon process affecting that transition and the energy in wavenumbers involved, β the coupling constants associated with that direct processes and σ is a measure of the goodness of fit.

Where

$$\sigma = \frac{\sum\left(y_{Exp} - y_{Fit}\right)}{\sum y_{Exp}}$$

Even in the transitions where multiple direct single-phonon processes may be dominant, the coupling constant associated with Raman scattering, α, seems to remain relatively constant. The constant α suggests that the inability to determine which single-phonon processes dominates occurs in cases where there is not a strong single-phonon direct process, so the choice is between weak direct processes, with consequently less to differentiate between them.

Except for the cases of the $Z_1\ \gamma_7 \rightarrow Y_3\ \gamma_7\ C_{4v}$ transition and the $Z_3\ \gamma_7 \rightarrow Y_2\ \gamma_6\ C_{4v}$ transitions, the minimum linewidth can be taken to be the inhomogeneous component, or where there are multiple possible inhomogeneous components, then the highest of the inhomogeneous components for that transition. This is because the temperature independent component of the direct one-phonon emission terms, at the lowest temperatures, merely brings the linewidth up to what it is in the other models due to the inhomogeneous terms.

For the $Z_1\ \gamma_7 \rightarrow Y_3\ \gamma_7\ C_{4v}$ transition, for the fit without Raman scattering, which is the most likely fit, the minimum linewidth is 1.7 cm^{-1}, the inhomogeneous component of the linewidth. For the fit with Raman scattering included it is approximately 1.4 cm^{-1}.

For the $Z_3\ \gamma_7 \rightarrow Y_2\ \gamma_6\ C_{4v}$ transition, due to the contribution from the single phonon emission process, the inhomogeneous contribution cannot give the minimum linewidth. However, considering this contribution, the minimum linewidth for this transition is 0.28 cm^{-1}.

4.6 Temperature-Dependent Line Position Analysis

The line shift analysis was made using an approximation that the contribution from states such that $|E_i - E_j| \leq \hbar\omega_D$ is very small in comparison to the states where $|E_i - E_j| \gg \hbar\omega_D$. This is in most cases as good approximation, as demonstrated by Chen and Bartolo [40] as the other terms are not observed in a significant enough state to be noticeable.

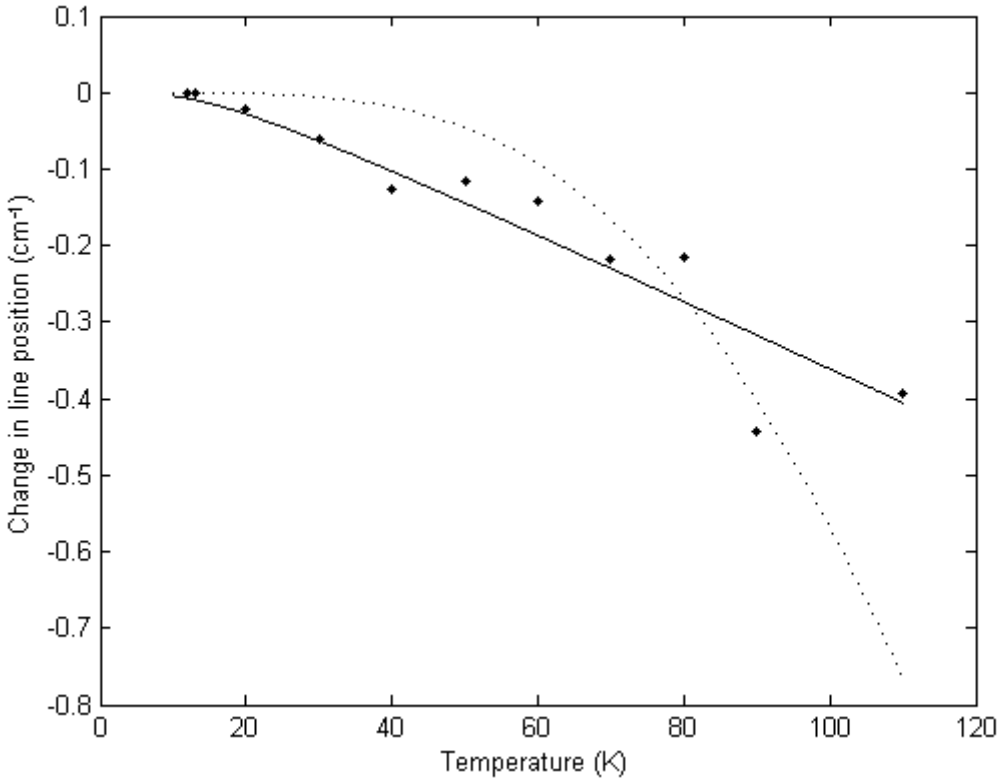

Figure 4-19: Temperature dependence of the line position of the $Z_1\ \boldsymbol{\gamma_4} \rightarrow Y_1\ \boldsymbol{\gamma_4}$ transition of $CaF_2:Er^{3+}$ in C_{3v} site symmetry where the solid line is the fit with a varied Debye temperature of 56 K, while the dotted line is a fit with a set Debye temperature of 516 K.

Figure 4.19 shows a fairly linear behaviour on the temperature scale here. Unfortunately at higher temperatures the intensity of this transition drops to levels such that it is difficult to determine the peak for the line position, meaning the behaviour after 80 K is difficult to characterise. It is apparent, however, that an effective Debye temperature similar to the literature value of 516 K is unlikely. Therefore, although it is not possible to determine exactly which phonon mode is dominant from this temperature range, it is possible to state that it is not the same mode that is responsible for line broadening.

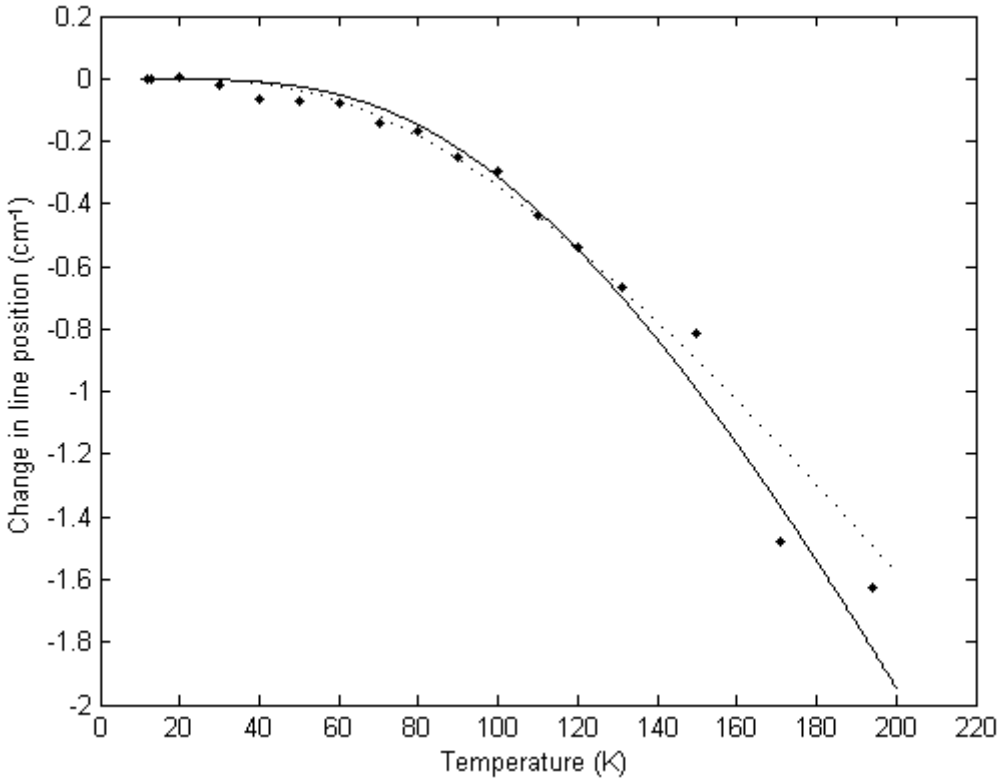

Figure 4-20: Temperature dependence of the line position of the $Z_1\ \boldsymbol{\gamma_7} \rightarrow Y_2\ \boldsymbol{\gamma_7}$ transition of $CaF_2:Er^{3+}$ in C_{4v} site symmetry where the dotted line is the fit with a varied Debye temperature of 375 K, while the solid line is a fit with a set Debye temperature of 516 K.

Figure 4.20 shows at low temperatures a strong correlation between the models with an effective Debye temperature of 375K and the one with the literature value of 516 K. This does, however, diverge at higher temperatures. This fitted Debye temperature gives a Debye frequency of 260 cm^{-1}. This could be due to either vibronic or Raman phonon modes [41]. Exactly which mode is dominant is undetermined as unfortunately there was insufficient data in the lineshape for this transition to analyse the temperature dependence of the linewidth.

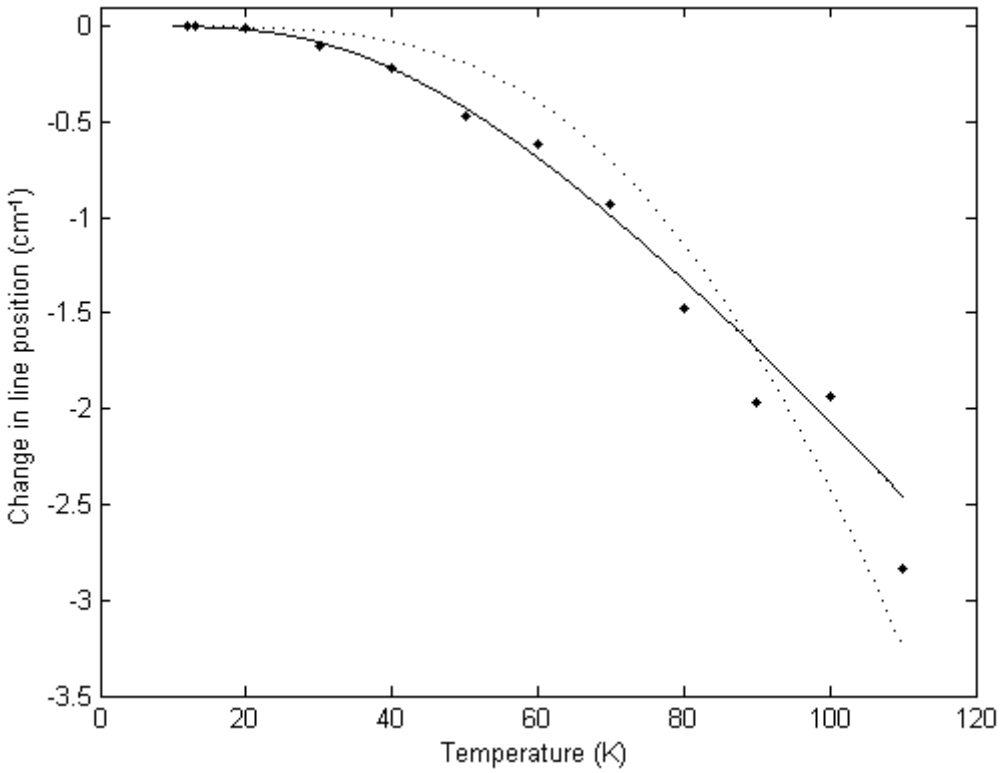

Figure 4-21: Temperature dependence of the line position of the $Z_1\ \boldsymbol{\gamma_4} \rightarrow Y_2\ \boldsymbol{\gamma_{5,6}}$ transition of $CaF_2:Er^{3+}$ in C_{3v} site symmetry where the solid line is the fit with a varied Debye temperature of 200 K, while the dotted line is a fit with a set Debye temperature of 516 K.

Figure 4.21 shows that in the case of the $Z_1\ \gamma_4 \rightarrow Y_2\ \gamma_{5,6}$ C_{3v} transition the effective Debye temperature provides a much better fit than the literature value. The effective Debye temperature corresponds to a Debye frequency of 139 cm^{-1}, which is likely due to vibronic phonons, although it smaller than the lowest recorded vibronic phonon peak by 11 cm^{-1} [41]. This is still the closest phonon energy however, as the lowest Raman scattering peak is at 157 cm^{-1} [41].

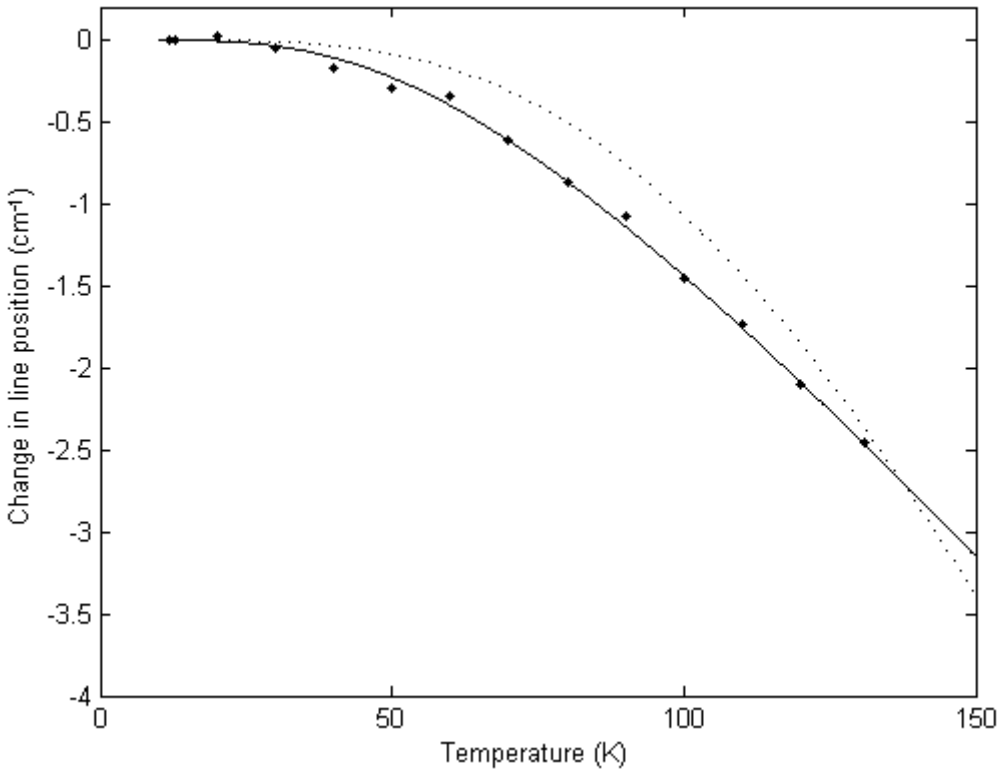

Figure 4-22: Temperature dependence of the line position of the $Z_1\ \boldsymbol{\gamma_7} \rightarrow Y_3\ \boldsymbol{\gamma_7}$ transition of $CaF_2:Er^{3+}$ in C_{4v} site symmetry where the solid line is the fit with a varied Debye temperature of 260 K, while the dotted line is a fit with a set Debye temperature of 516 K.

A Debye temperature of 260 K provides a much better fit for the $Z_1\ \gamma_7 \rightarrow Y_3\ \gamma_7$ transition in the C_{4v} site symmetry (figure 4.22) than the literature value of 516 K. This corresponds to a Debye frequency of 180 cm^{-1}, which corresponds to a vibronic phonon state [41]. The difference between the fitted and the literature Debye temperatures suggests that different phonon processes are dominant between the thermal line shift and the thermal linewidth change.

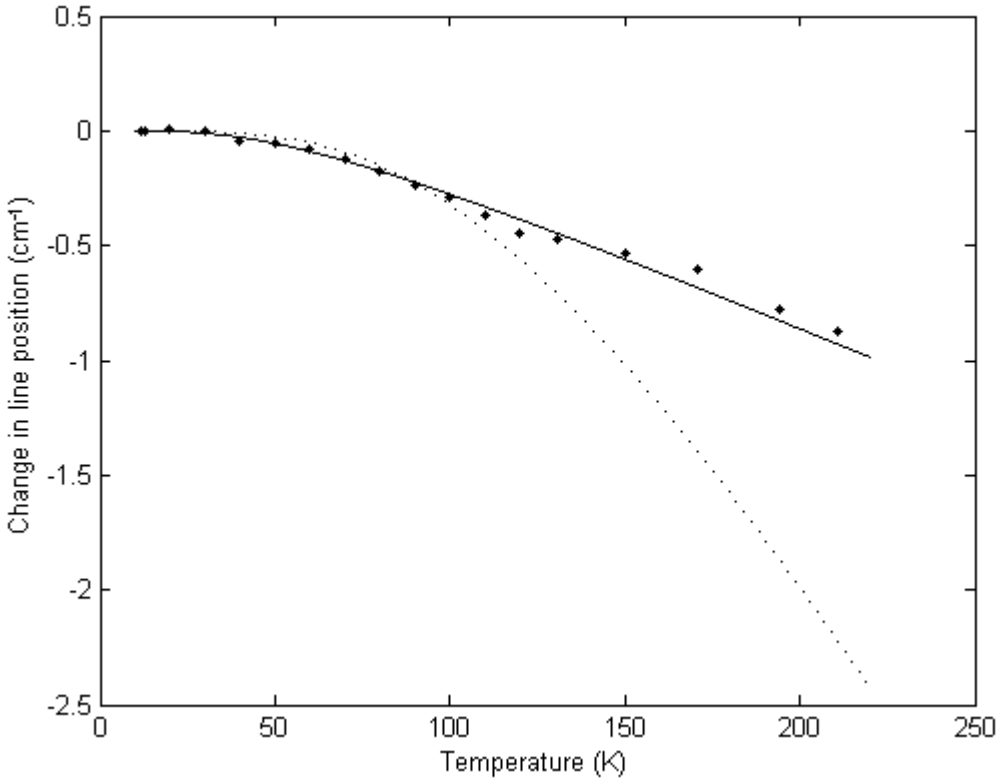

Figure 4-23: Temperature dependence of the line position of the Z_2 $\boldsymbol{\gamma_6}$ → Y_1 $\boldsymbol{\gamma_6}$ transition of CaF_2:Er^{3+} in C_{4v} site symmetry where the solid line is the fit with a varied Debye temperature of 210 K, while the dotted line is a fit with a set Debye temperature of 516 K.

A Debye temperature of 210 K provides a much better fit for the Z_2 γ_6 → Y_1 γ_6 transition in the C_{4v} site symmetry (figure 4.23) than the literature value of 516 K. This gives a Debye frequency of 145 cm^{-1}, corresponding to a vibronic transition [41]. The most significant component of the linewidth is the Raman scattering, so the line shift being dominated by optical phonons rather than Raman is expected by the large difference in the Debye temperatures.

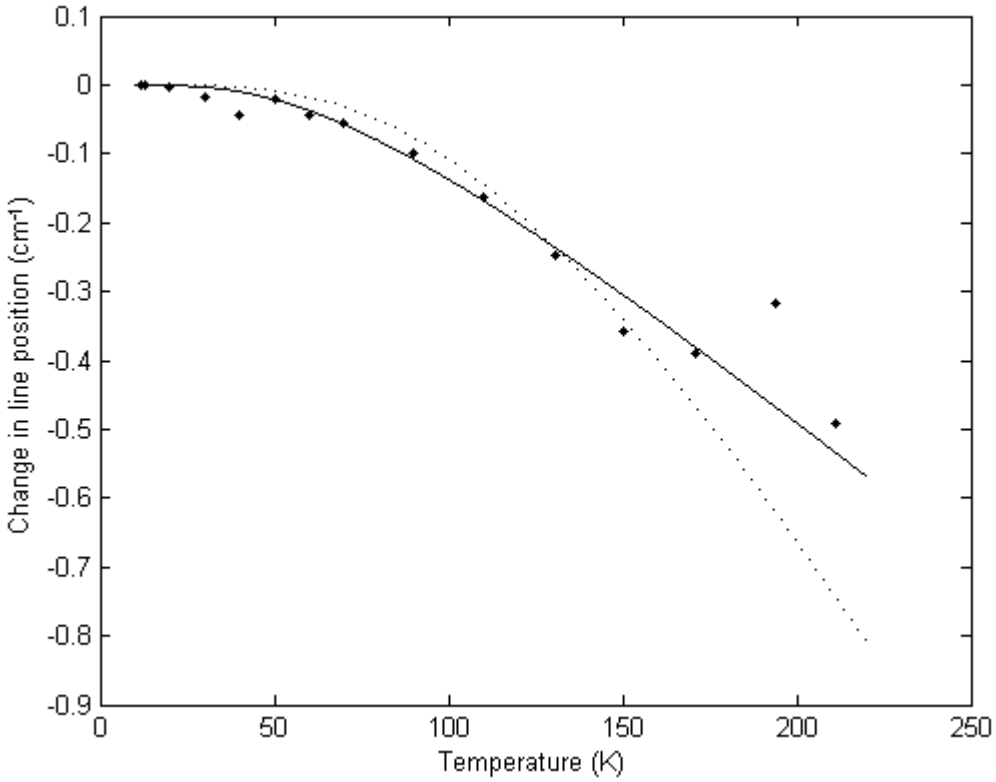

Figure 4-24: Temperature dependence of the line position of the $Z_3\ \boldsymbol{\gamma_7} \rightarrow Y_2\ \boldsymbol{\gamma_6}$ transition of $CaF_2:Er^{3+}$ in C_{4v} site symmetry where the solid line is the fit with a varied Debye temperature of 270 K, while the dotted line is a fit with a set Debye temperature of 516 K.

A Debye temperature of 270 K provides a much better fit for the $Z_3\ \gamma_7 \rightarrow Y_2\ \gamma_6$ transition in the C_{4v} site symmetry (figure 4.24) than the literature value of 516 K. This gives a Debye frequency of 188 cm^{-1}, corresponding to a vibronic transition [41]. Like the other transitions, this is expected due to the difference between the Debye temperatures indicating different processes dominate.

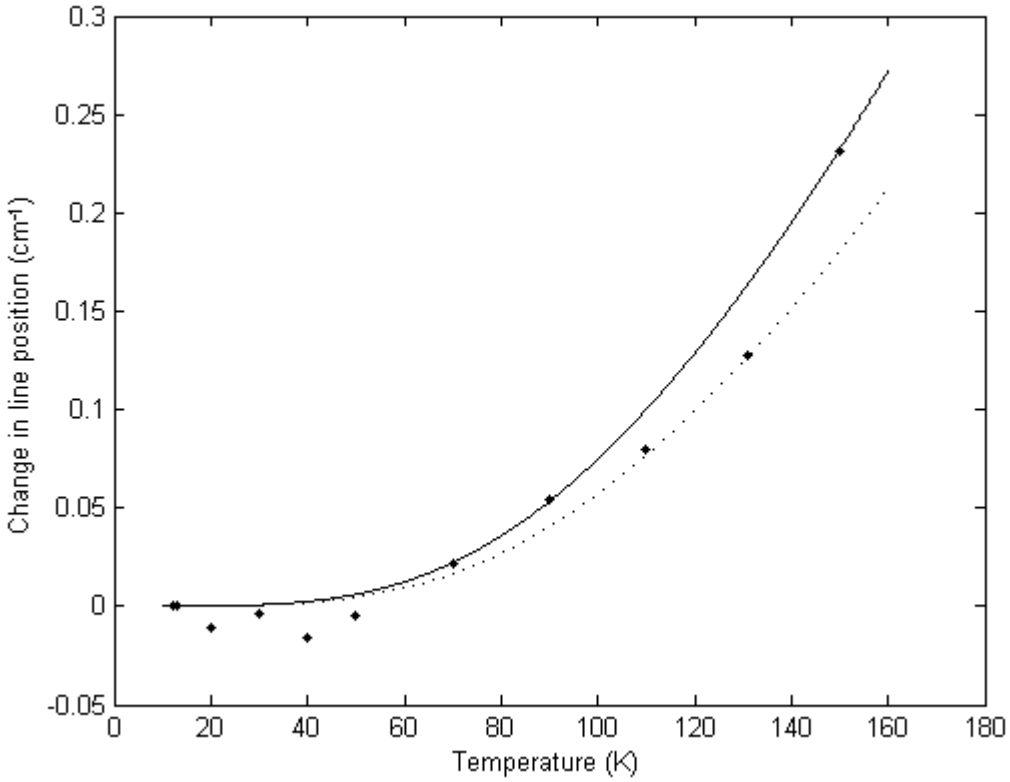

Figure 4-25: Temperature dependence of the line position of the $Z_3\ \boldsymbol{\gamma_7} \rightarrow Y_1\ \boldsymbol{\gamma_6}$ transition of $CaF_2:Er^{3+}$ in C_{4v} site symmetry where the solid line is the fit with a varied Debye temperature of 500 K, while the dotted line is a fit with a set Debye temperature of 516 K.

The similarity between the varied Debye temperature and the literature Debye temperature in the case of the $Z_3\ \gamma_7 \rightarrow Y_1\ \gamma_6$ C_{4v} transition indicates that it most likely is the literature Debye temperature. The difference between the models and the data is probably due to the approximation made in the models, which cannot deal with blue- and red-shifted data points. This creates the small discrepancy between the electron-phonon coupling constant, α', between the two models. This does indicate, however, that the phonon modes contributing to line broadening are the same modes contributing to line shift for this transition.

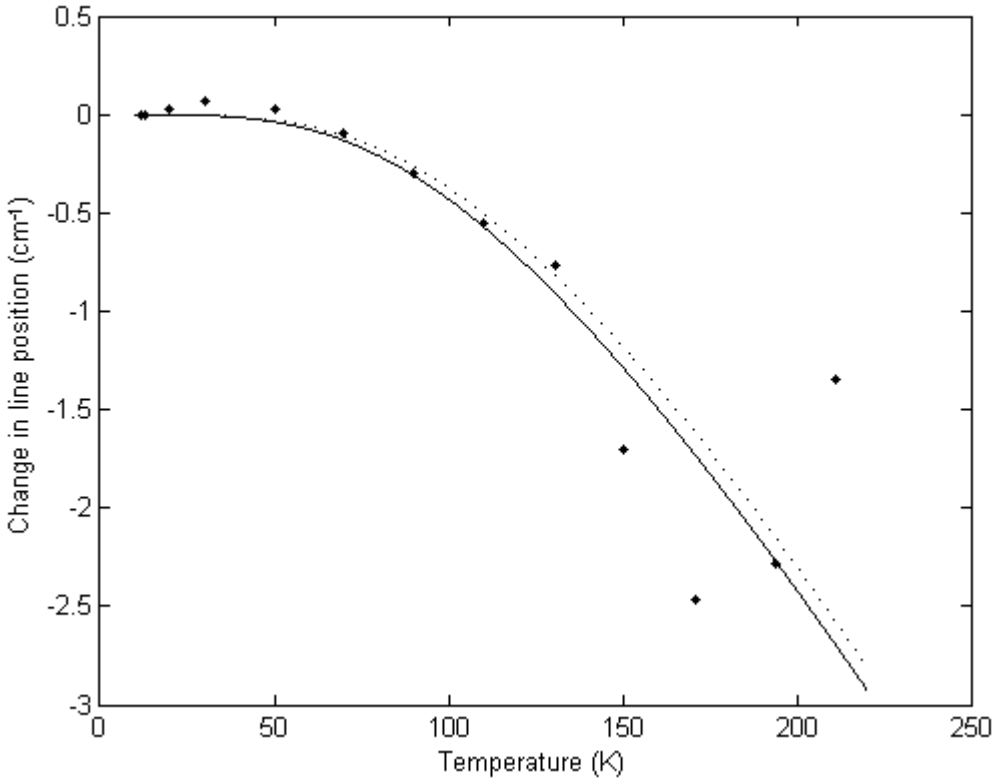

Figure 4-26: Temperature dependence of the line position of the $Z_2\ \boldsymbol{\gamma_6} \rightarrow Y_2\ \boldsymbol{\gamma_7}$ transition of $CaF_2:Er^{3+}$ in C_{4v} site symmetry where the solid line is the fit with a varied Debye temperature of 470 K, while the dotted line is a fit with a set Debye temperature of 516 K.

The discrepancy between the fitted Debye temperature and the literature Debye temperature in the $Z_2\ \gamma_6 \rightarrow Y_2\ \gamma_7$ C_{4v} transition is much smaller than in most of the other transitions. There were, however, problems at the higher temperatures determining the exact line position. This means that a precise assignment of Debye temperature is difficult. However, judging by the trend if the fitted Debye temperature is inaccurate then it is overestimated, which would put it in closer alignment with the Raman phonon mode of 322 cm^{-1} [41]. This would not appreciably change the coupling constant, α'.

Transitions	α' (cm^{-1})	T_D (K)	ω_D (cm^{-1})	σ
C_{4v}				
$Z_1\,\gamma_7 \rightarrow Y_2\,\gamma_7$	-19	375	260	0.06
	-44	519	359	0.009
$Z_1\,\gamma_7 \rightarrow Y_3\,\gamma_7$	-33	260	180	0.002
	-150	519	359	0.2
$Z_2\,\gamma_6 \rightarrow Y_1\,\gamma_6$	-4.1	210	145	0.01
	-45	519	359	0.8
$Z_2\,\gamma_6 \rightarrow Y_2\,\gamma_7$	-45	470	326	0.06
	-52	519	359	0.02
$Z_3\,\gamma_7 \rightarrow Y_1\,\gamma_6$	9.5	500	348	0.2
	8	519	359	0.07
$Z_3\,\gamma_7 \rightarrow Y_2\,\gamma_7$	-3.4	270	188	0.03
	-15	519	359	0.2
C_{3v}				
$Z_1\,\gamma_4 \rightarrow Y_1\,\gamma_4$	-0.75	56	39	0.02
	-80	519	359	0.02
$Z_1\,\gamma_4 \rightarrow Y_2\,\gamma_{5,6}$	-28	200	139	0.06
	-340	519	359	0.06

Table 4-9: Parameters for the line shift of $CaF_2:Er^{3+}$. Where α' is the coupling constant, T_D is the Debye temperature, $\boldsymbol{\omega_D}$ is the Debye frequency associated with that Debye temperature and σ is the goodness of fit for that transition and Debye temperature.

Of the transitions from sites in C_{4v} symmetry states, most ended with Debye temperatures considerably different from the literature value of 519 K [40]. Therefore, with the exception of the $Z_3\,\gamma_7 \rightarrow Y_1\,\gamma_6$ C_{4v} transition, different phonon modes are responsible for the line shifts and the line broadening. The fitting was done by varying the Debye temperature and the coupling constant α', using the approximation that states such that $|E_i - E_j| \gg \hbar\omega_D$ dominate. A more complete model would likely involve accounting for the states where $|E_i - E_j| \leq \hbar\omega_D$, giving a better fit to the data. This is mainly due to the arrangement of the data points in the 10 K to 50 K, where the simplified model used is unable to adequately describe, causing both a positive and a negative change in line position across the series.

Of the transitions where the fitted Debye temperature is different from the literature value, for the $Z_1\ \gamma_4 \rightarrow Y_1\ \gamma_4\ C_{3v}$ transition the dominant phonon mode could not be determined due to the limitations due to the temperature range. Similarly, for the $Z_1\ \gamma_7 \rightarrow Y_2\ \gamma_7\ C_{4v}$ transition the dominant phonon could be either Raman or vibronic, but due to the close alignment between two modes it is difficult to determine which. The $Z_2\ \gamma_6 \rightarrow Y_2\ \gamma_7\ C_{4v}$ transition is broadened by a Raman phonon mode, however, whilst the other four transitions are broadened by vibronic modes.

4.7 Conclusion

There is a fairly good agreement between the simulated spectra and the experimental spectra, although there are small irregular discrepancies in the line positions across the series. These are probably due to the differences between the LaF_3 from which most of the parameters were acquired and the CaF_2 used in this thesis.

The linewidth study showed that direct single-phonon processes needed to be considered for CaF_2:Er^{3+}, as for example the $Z_1\ \gamma_4 \rightarrow Y_1\ \gamma_4\ C_{3v}$ site transition showed no appreciable Raman scattering in the temperature range studied, and even when the Raman process dominates, the coupling constant without the direct processes can be very different from that with. In the case where it is difficult to determine exactly which direct process is dominant, however, the coupling constant associated with Raman scattering is similar, whilst still being different from what it would be if there were no direct processes considered.

Further work on the linewidths is needed in order to identify exactly which direct processes are dominant in these transitions, particularly the $Z_1\ \gamma_7 \rightarrow Y_3\ \gamma_7\ C_{4v}$ in order to determine if Raman scattering is significant or not in these temperature ranges. To more precisely model the line positions, states such that $|E_i - E_j| \leq \hbar\omega_D$ should be included. These were not included in the models used in this work, and have a much smaller contribution than states such that $|E_i - E_j| \gg \hbar\omega_D$, however the contribution seems significant enough that future studies should consider them.

Chapter 5 Temperature Dependent Infrared Absorption of $CsCdBr3:Er^{3+}$

5.1 Introduction

Unlike in the $CaF_2:Er^{3+}$ system, $CsCdBr_3$ has only one major symmetry centre, a C_{3v} site. This means that there are fewer transitions in the doped spectra. There has been much previous work done on rare earth doped $CsCdBr_3$, but little of it dealt with Er^{3+}. The most significant of those that did on this work, however, is that by *Quagliano et al* [23], who did an analysis of the energy levels and crystal field calculations, both of which were used in this thesis.

Analysis of the phonon modes in $CsCdBr_3$ was done by *Malkin et al* [42], and this was used in the line position analysis to determine which phonon modes were dominant. *Barthem et al* also did analysis of the phonon structure of $CsCdBr_3$, and were able to determine that the cut-off frequency of $CsCdBr_3$ is 90 cm^{-1} [43]. In the Debye approximation this is the Debye frequency, ω_D, giving a Debye temperature of 129 K. This Debye temperature was then used in the fits for the temperature dependent line broadening caused by Raman scattering, although in almost all of the transition studied in this chapter this component was minimal. This is discussed in section 5.5.

As in chapter 4, the models for line position use the simplified equation neglecting components from states such that $|Ei - Ej| \leq \hbar\omega_D$, but this simplified model fits the data well. There are, however, some transitions which cannot be modelled, as is discussed in section 5.2. This causes some problems when trying to describe trends across the series.

5.2 IR Spectra

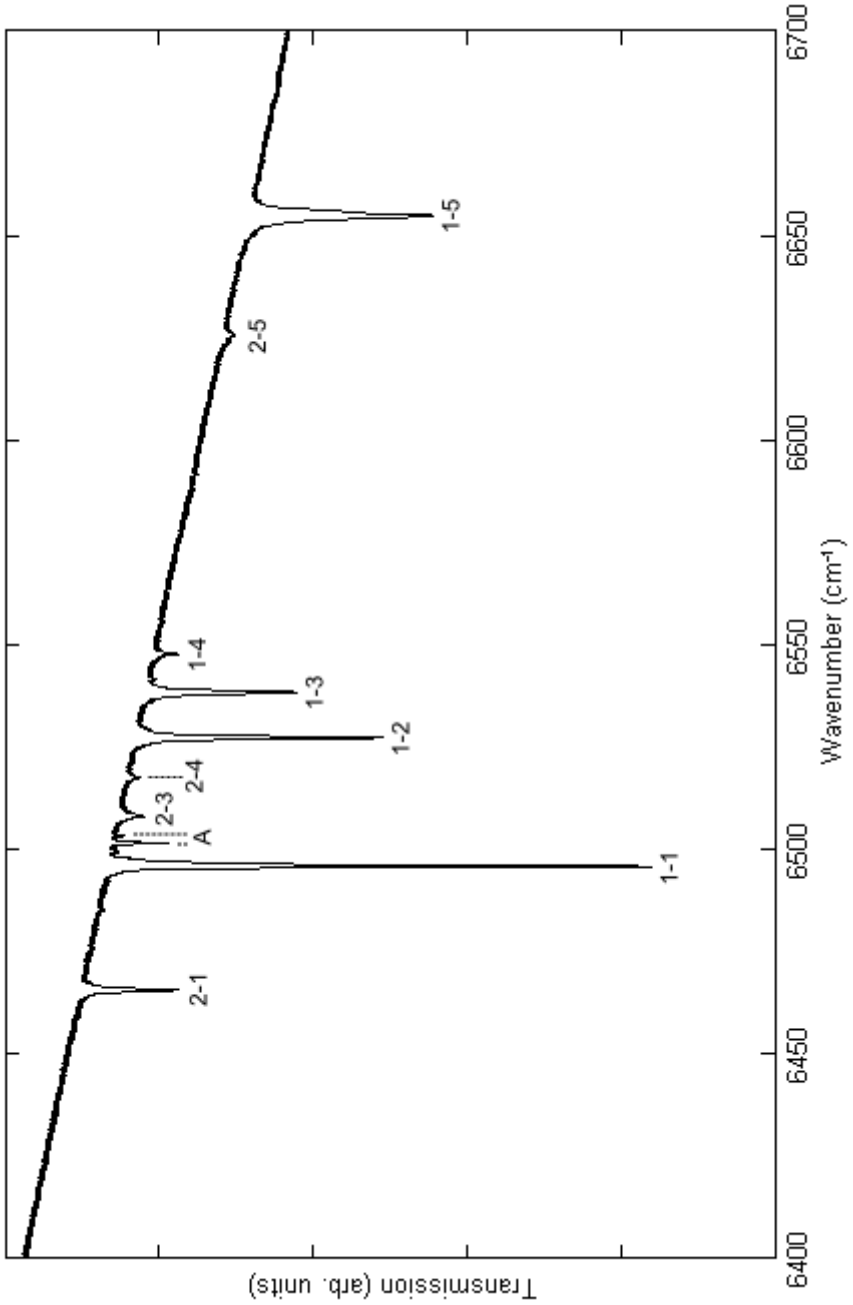

Figure 5-1: FTIR spectra of Er^{3+} doped $CsCdBr_3$ at 10 K. Notation is Z_A to Y_B is given by A-B. The transitions labeled A are due to impurities, likely either Sm^{3+} or Pr^{3+}.

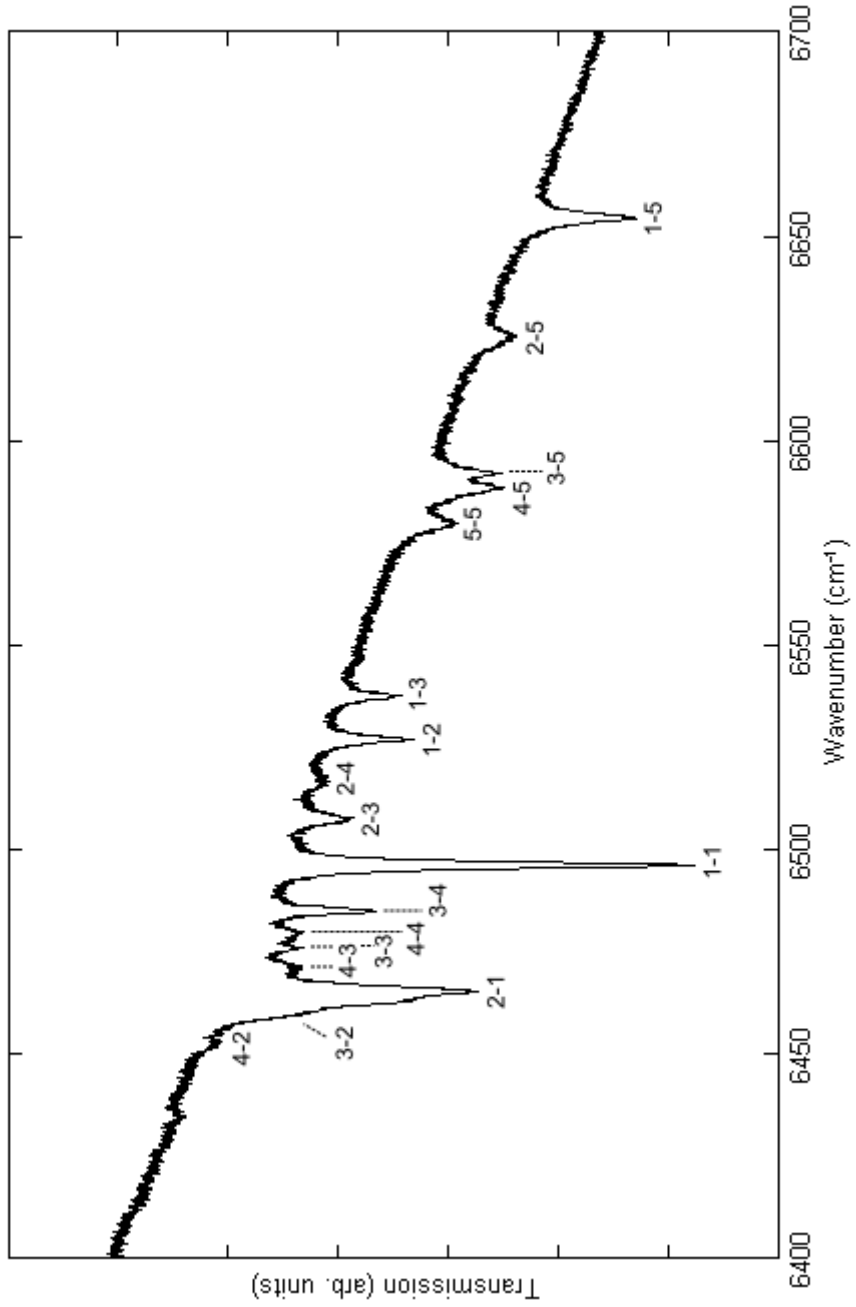

Figure 5-2: FTIR spectra of Er^{3+} doped $CsCdBr_3$ at 70 K. Notation is Z_A to Y_B is given by A-B.

There is only the one significant symmetry site in Er^{3+} doped $CsCdBr_3$, resulting in fewer spectral lines compared with CaF_2. The transitions were assigned based on the energy levels of Er^{3+} in $CsCdBr_3$ determined by *Quagliano et al.* [23] in 1996 using the same method as described in section 4.2. The proximity of so many different transitions between 6450 and 6480 cm^{-1} has limited the ability to analyse those transitions, as it is impossible to accurately determine the linewidth and line position for any of them, with the exception of the $Z_2\ \gamma_4 \rightarrow Y_1\ \gamma_4$ at the lowest temperatures.

Transition	Energy (cm^{-1})	Linewidth (cm^{-1})
$Z_1\,\gamma_{5,6} \rightarrow Y_1\,\gamma_4$	6495.9	0.6
$Z_1\,\gamma_{5,6} \rightarrow Y_2\,\gamma_4$	6527.4	0.8
$Z_1\,\gamma_{5,6} \rightarrow Y_3\,\gamma_{5,6}$	6538.4	1.0
$Z_1\,\gamma_{5,6} \rightarrow Y_5\,\gamma_{5,6}$	6654.9	2.0
$Z_2\,\gamma_4 \rightarrow Y_1\,\gamma_4$	6465.7	1.0
$Z_2\,\gamma_4 \rightarrow Y_3\,\gamma_{5,6}$	6508.2	1.4

Table 5-1: The transition energies, which give line position, and the linewidths of the transitions studied in this section, at 10 K

5.3 Crystal Field Analysis

Crystal field analysis was done based on the parameters used by *Quagliano et al* [23] and compared with their observed energy levels.

There is good agreement between the $^4I_{13/2}$ observed and the calculated energy levels, although the agreement between the $^4I_{15/2}$ observed and calculated energy levels is not as good. Although the parameters used were from *Quagliano et al* there were some small differences in the calculated energy levels. It is presumed this is due to rounding in the values of those parameters.

Multiplet	Label	Irrep	$E_{observed}$ (cm^{-1})	E_{calc} (cm^{-1})
$^4I_{13/2}$	Y_7	γ_4	-	6668
	Y_6	γ_4	-	6666
	Y_5	$\gamma_{5,6}$	6660	6665
	Y_4	γ_4	6544	6546
	Y_3	$\gamma_{5,6}$	6536	6533
	Y_2	γ_4	6524	6522
	Y_1	γ_4	6492	6494
$^4I_{15/2}$	Z_8	γ_4	242	252
	Z_7	$\gamma_{5,6}$	237	249
	Z_6	γ_4	224	236
	Z_5	$\gamma_{5,6}$	76	72
	Z_4	γ_4	69	61
	Z_3	γ_4	63	58
	Z_2	γ_4	31	19
	Z_1	$\gamma_{5,6}$	0	-7

Table 5-2: Calculated and observed energy levels of Er^{3+}: $CsCdBr_3$. The observed energy levels are from *Quagliano et al* [23] and the calculated energy levels are from this thesis.

Parameter	Value	Parameter	Value	Parameter	Value
EAVG	35254	T^4	-14 *	P^4	0.75 P^2
F^2	97431	T^6	324 *	P^6	0.50 P^2
F^4	70133	T^7	-172 *	B_A^2	135
F^6	49350	T^8	-122	B_A^4	4510
α	18.4	ζ	-2350	B_A^6	77
β	-676	M^0	4.8	$B_{A'}^6$	40
γ	1787 *	M^2	0.56 M^0	B_C^4	-423
T^2	-286 *	M^4	0.38 M^0	B_C^6	-179
T^3	-44	P^2	525	G_{10A0}^4	612

Table 5-3: Parameters used in the crustal field calculations for $CsCdBr_3$:Er^{3+}. Although these parameters were obtained from the paper by *Quagliano et al* [23] on this system, the parameters marked * were fixed values from $LaCl_3$:Er^{3+}. It should be noted that the crystal field parameters, $\boldsymbol{B_q^k}$, were converted to the format of Muujaji [35] for ease of comparison with those in chapter 4.

5.4 Simulated Spectra

Because of the way the crystal was cut, the orientation of the C_{3v} site with relation to the optical path is unknown. Using the simulated spectra and the experimental spectra it should be possible to determine this orientation. Unfortunately, however, the simulated energy levels differ substantially from the experimental energy levels, resulting in simulated spectra with a much different appearance to that the experimentally obtained spectra. Therefore in the simulated spectra the experimental energy levels had to be used. For the Y_6 γ_4 and Y_7 γ_4 energy levels, there were however no experimental energy level to use. Noting the good agreement of the other $^4I_{13/2}$ energy levels, with the exception of the Y_5 $\gamma_{5,6}$, the theoretical energy levels were used for the Y_6 γ_4 and Y_7 γ_4 energy levels.

The use of these energy levels do somewhat constrain the use of the simulated spectra, but it does allow a meaningful comparison to be done with the experimental spectra. A small shift of 4 cm^{-1} was also required to match the transition energies calculated from the energy levels with those observed in the experimental spectra. This is likely due to the calibration of the spectrometer.

As in the CaF_2:Er^{3+} simulated spectra, Lorentzian line shapes were used. This is because as with the CaF_2:Er^{3+} simulated spectra there was very little difference between the Lorentzian and the Voigt simulated spectra.

The best fit for the intensities was for an orthoaxial spectra in a combination σ and π polarization, in an approximately 2:1 σ to π ratio. This number was achieved by varying the ratio until the ratio of the intensities of significant peaks that depended heavily on one polarization was close to that of the experimental spectra, for both the 70 K and the 10 K spectra. This orthoaxial spectra suggests a perpendicular arrangement of the MX_3 chains relative to the spectrometer, and the polarisation ratio of 2:1 σ to π suggests a slight circular dichroism.

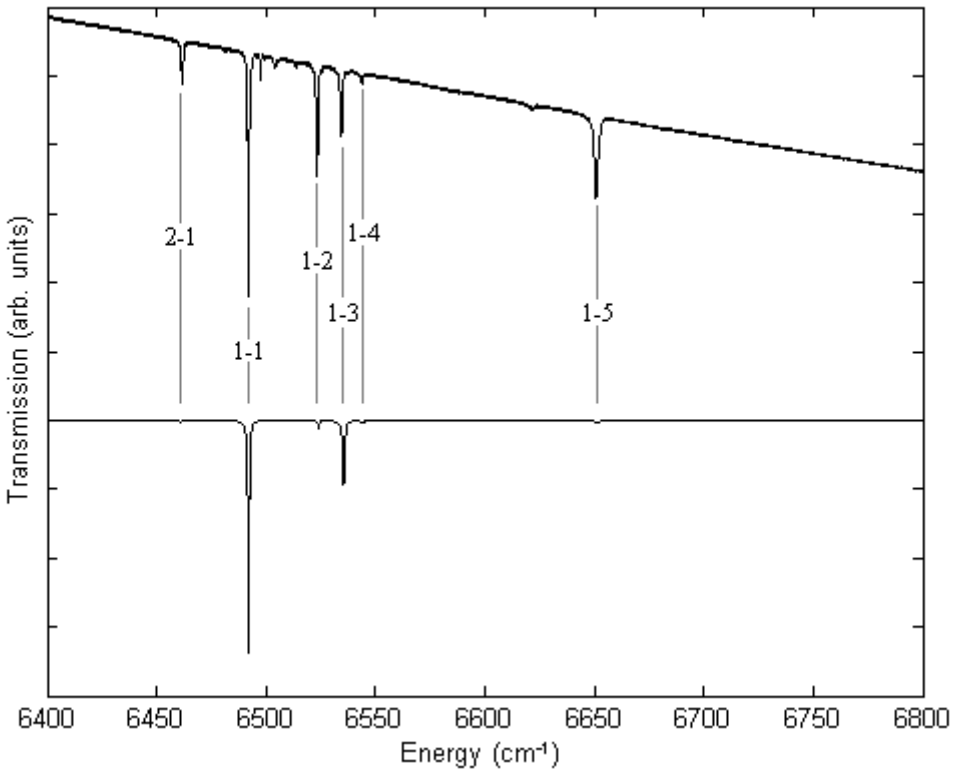

Figure 5-3: Simulated (bottom) and experimental (top) spectra of $CsCdBr_3:Er^{3+}$ at 10 K. Notation is $Z_A \rightarrow Y_B$ is A-B. The unlabeled transitions were not significant in the simulated spectra.

In the 10 K spectra, several strong transitions from the experimental spectra have been noted to be too small in the simulated spectra. These include the $Z_1\ \gamma_{5,6} \rightarrow Y_2\ \gamma_4$ and the $Z_1\ \gamma_{5,6} \rightarrow Y_5\ \gamma_{5,6}$ transitions, although the less intense transitions are also smaller than in the experimental spectra. This suggests that there are likely significant electric dipole transitions taking place.

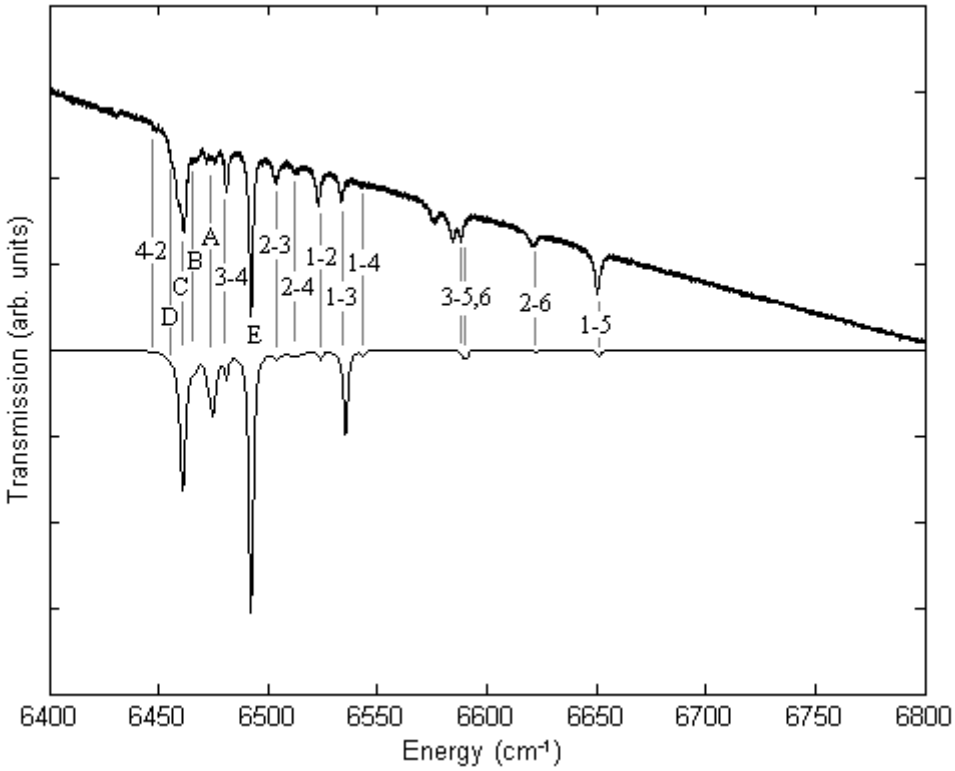

Figure 5-4: Simulated (bottom) and experimental (top) spectra of $CsCdBr_3:Er^{3+}$ at 70 K. Notation is $Z_A \rightarrow Y_B$ is A-B. The transition denoted by A is $Z_4\ \boldsymbol{\gamma_4} \rightarrow Y_3\ \boldsymbol{\gamma_{5,6}}$, B denotes two transitions, the $Z_3\ \boldsymbol{\gamma_4} \rightarrow Y_3\ \boldsymbol{\gamma_{5,6}}$ and the $Z_4\ \boldsymbol{\gamma_4} \rightarrow Y_4\ \boldsymbol{\gamma_4}$, C denotes the $Z_2\ \boldsymbol{\gamma_4} \rightarrow Y_1\ \boldsymbol{\gamma_4}$ transition, D denotes the $Z_3\ \boldsymbol{\gamma_4} \rightarrow Y_2\ \boldsymbol{\gamma_4}$ transition and E denotes both the $Z_1\ \boldsymbol{\gamma_{5,6}} \rightarrow Y_1\ \boldsymbol{\gamma_4}$ transition and the $Z_2\ \boldsymbol{\gamma_4} \rightarrow Y_2\ \boldsymbol{\gamma_4}$ transition. The other unlabeled transitions were not significant in the simulated spectra.

Temperature	FWHM (cm^{-1})						
10 K		$Y_1\ \gamma_4$	$Y_2\ \gamma_4$	$Y_3\ \gamma_{5,6}$	$Y_4\ \gamma_4$	$Y_5\ \gamma_{5,6}$	$Y_6\ \gamma_4$
	$Z_1\ \gamma_{5,6}$	0.64	0.85	1.03	0.87	2.03	-
	$Z_2\ \gamma_4$	0.98	0.5 *	1.44	1.04	-	-
70 K		$Y_1\ \gamma_4$	$Y_2\ \gamma_4$	$Y_3\ \gamma_{5,6}$	$Y_4\ \gamma_4$	$Y_5\ \gamma_{5,6}$	$Y_6\ \gamma_4$
	$Z_1\ \gamma_{5,6}$	1.92	2.22	2.19	2.26	2.97	-
	$Z_2\ \gamma_4$	3.30	2 *	3.96	8.64	-	4.02
	$Z_3\ \gamma_4$	-	3.00	2.29	1.97	1 *	2.31
	$Z_4\ \gamma_4$	-	2.75	3.43	3.37	-	-

Table 5-4: Parameters used in the simulated spectra for the full width at half maximum (FWHM) for the transitions. Parameters marked * are estimated, transitions with parameters marked with - were not significant enough to be noticeable; the other parameters were obtained from the experimental spectra. Transitions represented by values not in this table were not significant enough to be noticeable.

Although several of the transitions are less intense in the model at 70 K than in the experimental spectra, this is much less apparent than at 10 K. There are still some issues with the model at

this temperature, however. It overestimates the intensity of the $Z_3\ \gamma_4 \rightarrow Y_3\ \gamma_{5,6}$ transition, whilst still underestimating the intensity of the $Z_1\ \gamma_{5,6} \rightarrow Y_5\ \gamma_{5,6}$ transition.

5.5 Temperature Dependent Linewidth Analysis

The simplified model of just inhomogeneous component and Raman scattering does not fit the Er^{3+} doped $CsCdBr_3$. This is evidenced by the almost linear behaviour of the lineshape for most of the transitions, which does not fit the Raman model very well. Therefore fitting was done using the direct processes as well as the Raman scattering and the inhomogeneous component. It was assumed that that one direct process was dominant over the other processes, unless a reasonable fit was unable to be obtained. In this case two or more direct processes were considered. This was to avoid overparameterization, and it was shown in chapter four that assignment of exact direct process does not appreciably change the magnitude of the coupling constant of Raman scattering.

In the case of the $Z_1\ \gamma_{5,6} \rightarrow Y_1\ \gamma_4$ transition (see figure 5.5) there is very little difference between the fits using $Z_1\ \gamma_{5,6} \rightarrow Z_2\ \gamma_4$ or $Y_1\ \gamma_4 \rightarrow Y_2\ \gamma_4$ direct single phonon absorption. This is due to the very small difference between the differences of these energy states, 31 cm^{-1} for $Z_1\ \gamma_{5,6} \rightarrow Z_2\ \gamma_4$ and 32 cm^{-1} for $Y_1\ \gamma_4 \rightarrow Y_2\ \gamma_4$. This results in very similar equations describing these direct processes. In either case, as in almost all of the Er^{3+} doped $CsCdBr_3$ transitions studied in this chapter, there was no significant Raman scattering component. Due to the minimal differences between these two fits it is difficult to determine which one is more likely, so both are presented.

In the case of the $Z_2\ \gamma_4 \rightarrow Y_1\ \gamma_4$ transition (see figure 5.9) two one-phonon direct transitions were required; $Y_1\ \gamma_4 \rightarrow Y_2\ \gamma_4$ direct one phonon absorption and $Z_2\ \gamma_4 \rightarrow Z_1\ \gamma_{5,6}$ direct phonon emission. There was no significant Raman scattering component, however.

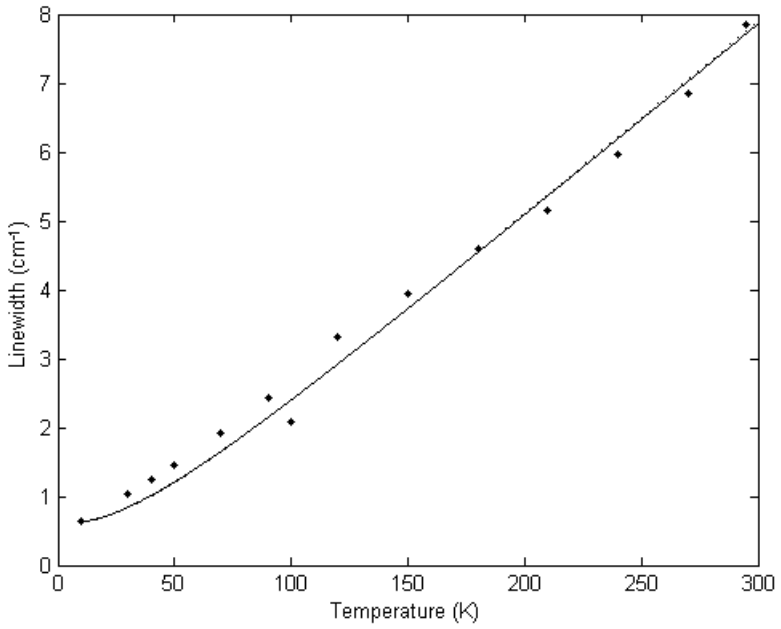

Figure 5-5: The fitted function for the linewidth for the $CsCdBr_3:Er^{3+}$ Z_1 $\boldsymbol{\gamma_{5,6}}$ → Y_1 $\boldsymbol{\gamma_4}$ transition. There is little difference between the fit using the Z_1 $\boldsymbol{\gamma_{5,6}}$ → Z_2 $\boldsymbol{\gamma_4}$ direct single phonon absorption, given by the solid line, or the Y_1 $\boldsymbol{\gamma_4}$ → Y_2 $\boldsymbol{\gamma_4}$ direct single phonon absorption, given by the dotted line.

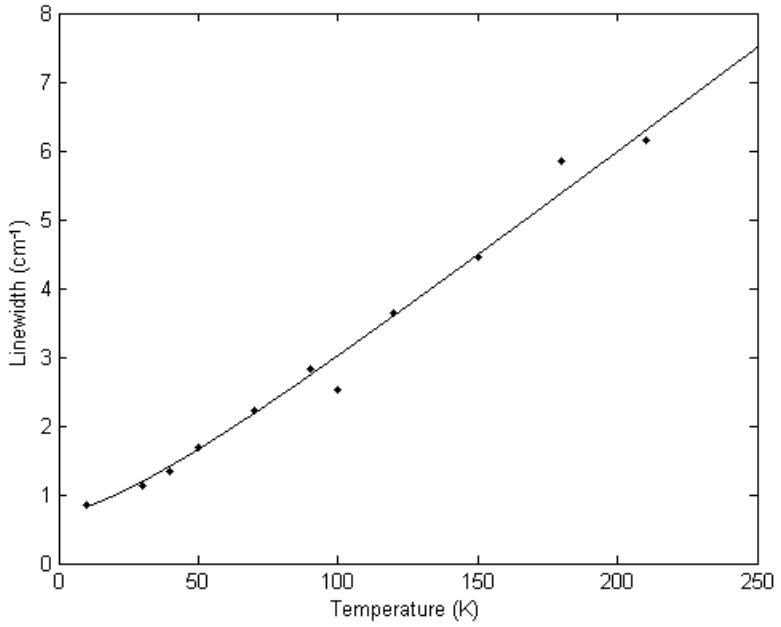

Figure 5-6: The fitted function for the linewidth for the $CsCdBr_3:Er^{3+}$ Z_1 $\boldsymbol{\gamma_{5,6}}$ → Y_2 $\boldsymbol{\gamma_4}$ transition, using Y_2 $\boldsymbol{\gamma_4}$ → Y_3 $\boldsymbol{\gamma_{5,6}}$ direct one phonon absorption.

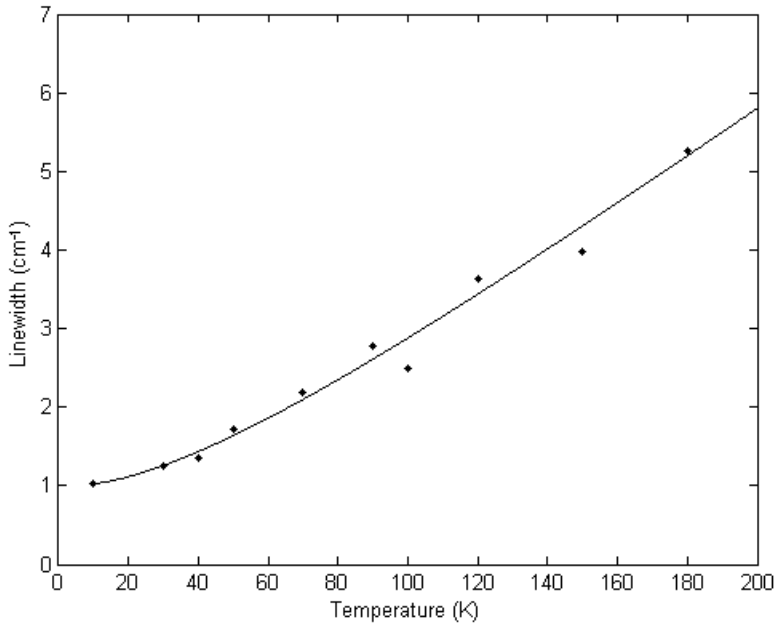

Figure 5-7: The fitted function for the linewidth for the $CsCdBr_3:Er^{3+}$ Z_1 $\boldsymbol{\gamma_{5,6}}$ → Y_3 $\boldsymbol{\gamma_{5,6}}$ transition, using Z_1 $\boldsymbol{\gamma_{5,6}}$ → Z_2 $\boldsymbol{\gamma_4}$ direct one phonon absorption.

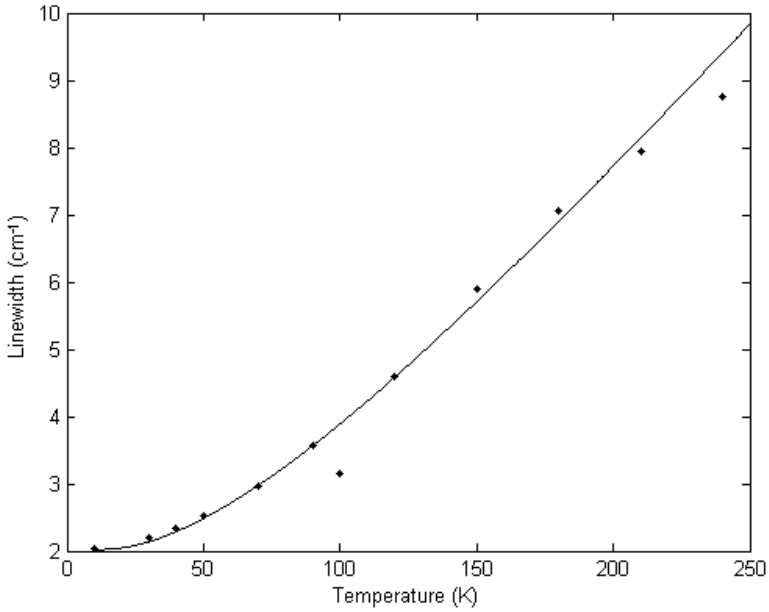

Figure 5-8: The fitted function for the linewidth for the $CsCdBr_3:Er^{3+}$ Z_1 $\boldsymbol{\gamma_{5,6}}$ → Y_5 $\boldsymbol{\gamma_{5,6}}$ transition, using Z_1 $\boldsymbol{\gamma_{5,6}}$ → Z_3 $\boldsymbol{\gamma_4}$ direct one phonon absorption.

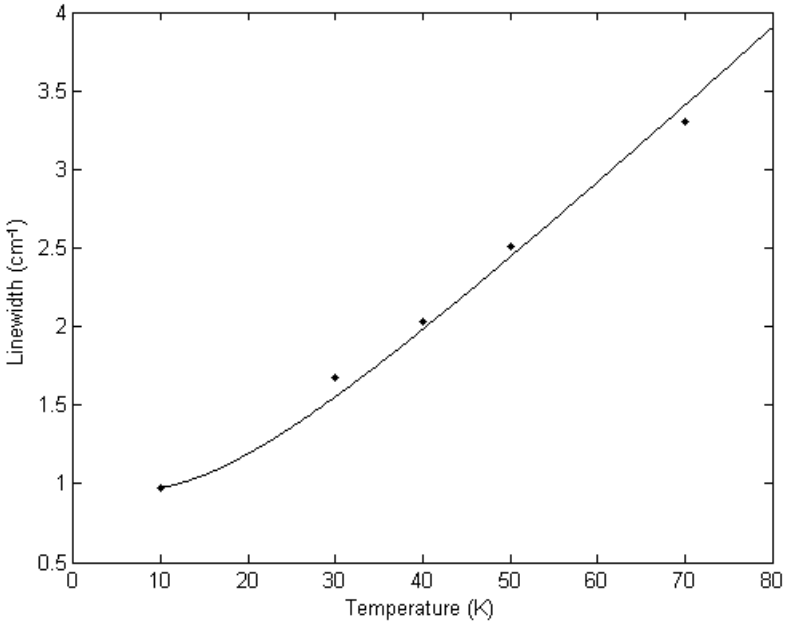

Figure 5-9: The fitted function for the linewidth for the $CsCdBr_3:Er^{3+}$ Z_2 $\boldsymbol{\gamma_4}$ → Y_1 $\boldsymbol{\gamma_4}$ transition, using Y_1 $\boldsymbol{\gamma_4}$ → Y_2 $\boldsymbol{\gamma_4}$ direct one phonon absorption and Z_2 $\boldsymbol{\gamma_4}$ → Z_1 $\boldsymbol{\gamma_{5,6}}$ direct phonon emission.

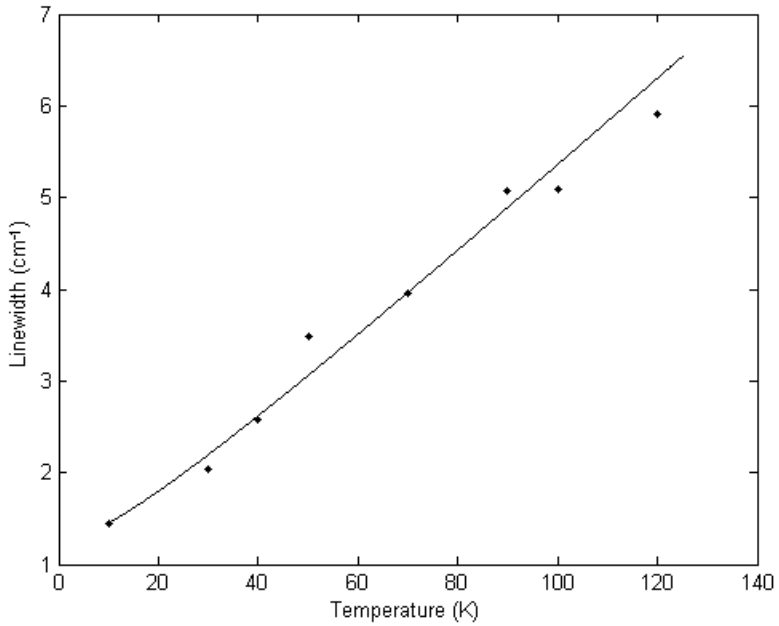

Figure 5-10: The fitted function for the linewidth for the $CsCdBr_3:Er^{3+}$ Z_2 $\boldsymbol{\gamma_4}$ → Y_3 $\boldsymbol{\gamma_{5,6}}$ transition, using Y_3 $\boldsymbol{\gamma_{5,6}}$ → Y_2 $\boldsymbol{\gamma_4}$ direct one phonon emission.

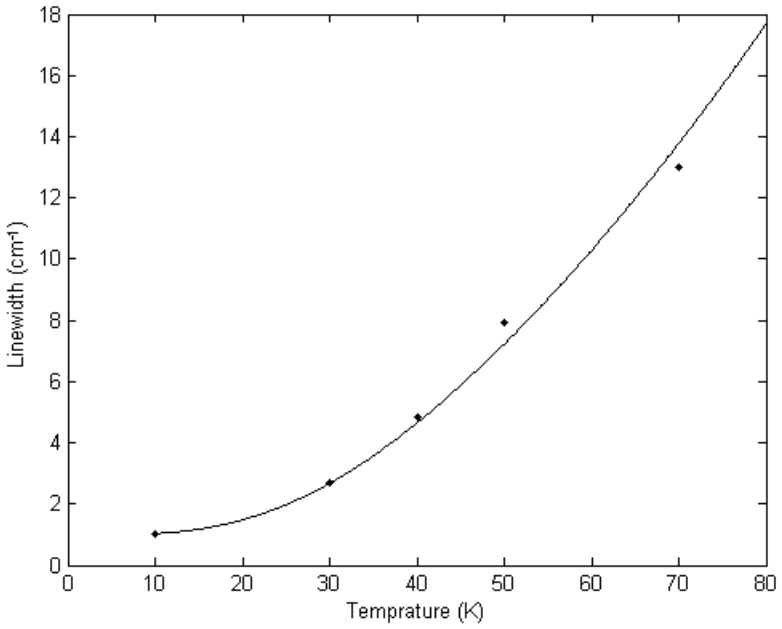

Figure 5-11: The fitted function for the linewidth for the $CsCdBr_3:Er^{3+}$ Z_2 $\boldsymbol{\gamma_4}$ → Y_4 $\boldsymbol{\gamma_4}$ transition, using Z_2 $\boldsymbol{\gamma_4}$ → Z_3 $\boldsymbol{\gamma_4}$ direct one phonon absorption and Raman scattering.

The Z_2 γ_4 → Y_4 γ_4 transition (figure 5.11) is the only transition studied in this system which had a significant Raman scattering component, and even this term has a significant component due to one-phonon direct absorption, Z_2 γ_4 → Z_3 γ_4. All of the other transitions in this chapter instead relied on just the inhomogeneous components and the single-phonon direct processes.

Transition		Inhomogeneous	Raman	Single Phonon Direct			
Assignment	Energy (cm^{-1})	Inh (cm^{-1})	α (cm^{-1})	Direct Transition	Energy	β (cm^{-1})	σ
$Z_1\,\gamma_{5,6} \rightarrow Y_1\,\gamma_4$	6492	0.62	0	$Z_1\,\gamma_{5,6} \rightarrow Z_2\,\gamma_4$	31	1.25	0.02
		0.62	0	$Y_1\,\gamma_4 \rightarrow Y_2\,\gamma_4$	32	1.3	0.02
$Z_1\,\gamma_{5,6} \rightarrow Y_2\,\gamma_4$	6524	0.76	0	$Y_2\,\gamma_4 \rightarrow Y_3\,\gamma_{5,6}$	12	0.53	0
$Z_1\,\gamma_{5,6} \rightarrow Y_3\,\gamma_{5,6}$	6536	1.02	0	$Z_1\,\gamma_{5,6} \rightarrow Z_2\,\gamma_4$	31	1.4	0.01
$Z_1\,\gamma_{5,6} \rightarrow Y_1\,\gamma_{5,6}$	6660	2.02	0	$Z_1\,\gamma_{5,6} \rightarrow Z_3\,\gamma_4$	63	4.1	0.02
$Z_2\,\gamma_4 \rightarrow Y_1\,\gamma_4$	6461	0.37	0	$Y_1\,\gamma_4 \rightarrow Y_2\,\gamma_4$	32	1.55	0.01
				$Z_2\,\gamma_4 \rightarrow Z_1\,\gamma_{5,6}$	31	0.8	
$Z_2\,\gamma_4 \rightarrow Y_3\,\gamma_{5,6}$	6505	0.78	0	$Y_3\,\gamma_{5,6} \rightarrow Y_2\,\gamma_4$	12	0.83	0.01
$Z_2\,\gamma_4 \rightarrow Y_4\,\gamma_4$	6513	1	150	$Z_2\,\gamma_4 \rightarrow Z_3\,\gamma_4$	32	6	0.01

Table 5-5: Parameters used in the fitting functions for the temperature dependence of the linewidths. Inh is the inhomogeneous component, α the coupling constant associated with Raman scattering, the direct transition indicates the direct phonon process affecting that transition and the energy in wavenumbers involved, β the coupling constants associated with that direct processes, σ is a measure of the goodness of fit and Δ is the energy of the transition, derived from the energy levels of *Quagliano et al* [23].

Where

$$\sigma = \frac{\sum(y_{Exp} - y_{Fit})}{\sum y_{Exp}}$$

In all of these transitions the fitted linewidths are in good agreement with the data, with the exception of the $Z_1\ \gamma_{5,6} \rightarrow Y_1\ \gamma_4$ at low temperatures. In this specific case, this was not able to be fixed with any variation or combination of direct processes and Raman scattering. Even so, the deviation is slight, causing minimal shift to the parameters. The lack of Raman scattering components suggests that in $CsCdBr_3:Er^{3+}$ it starts becoming significant at much higher temperatures, represented by a very small coupling constant. It is just that in the models used, this was taken to be zero, but it would have minimal effect being of a magnitude of approximately 0.1.

5.6 Temperature Dependent Line Position Analysis

Not all of the transitions could be analysed. For example, the $Z_1\ \gamma_{5,6} \rightarrow Y_1\ \gamma_4$ transition with the close positioning of the $Z_2\ \gamma_4 \rightarrow Y_2\ \gamma_4$ transition, mean that precise determination of the line position at a range of temperatures is impractical.

The absorption lines were analysed using a simplified model neglecting states with energies such that $|E_i - E_j| \leq \hbar\omega_D$ is significant, as the contributions from such states are small compared to states where $|E_i - E_j| \gg \hbar\omega_D$ is significant [32]. This model worked quite well, giving good fits to the data. Also, good fits were able to be achieved without varying the Debye temperature, except for the $Z_2\ \gamma_4 \rightarrow Y_1\ \gamma_4$ and $Z_2\ \gamma_4 \rightarrow Y_3\ \gamma_{5,6}$ transitions. This suggests that the electron-phonon coupling is possibly the same for the phonon modes which dominate in the line position changes and the line broadening changes [32]. Still, even varying the Debye temperature for the $Z_2\ \gamma_4 \rightarrow Y_3\ \gamma_{5,6}$ transition, the fit could be improved by adding a small component due to states where$|E_i - E_j| \leq \hbar\omega_D$. The other transitions' fits could also probably be improved by considering such states. The components from this would be much smaller than those from $|E_i - E_j| \gg \hbar\omega_D$ states already considered, however.

The magnitude of the coupling constant, α', was consistent between the different transitions, and consistently negative. This suggests that in all these cases the energy of the intermediate electronic level is lower than the energy of the initial level.

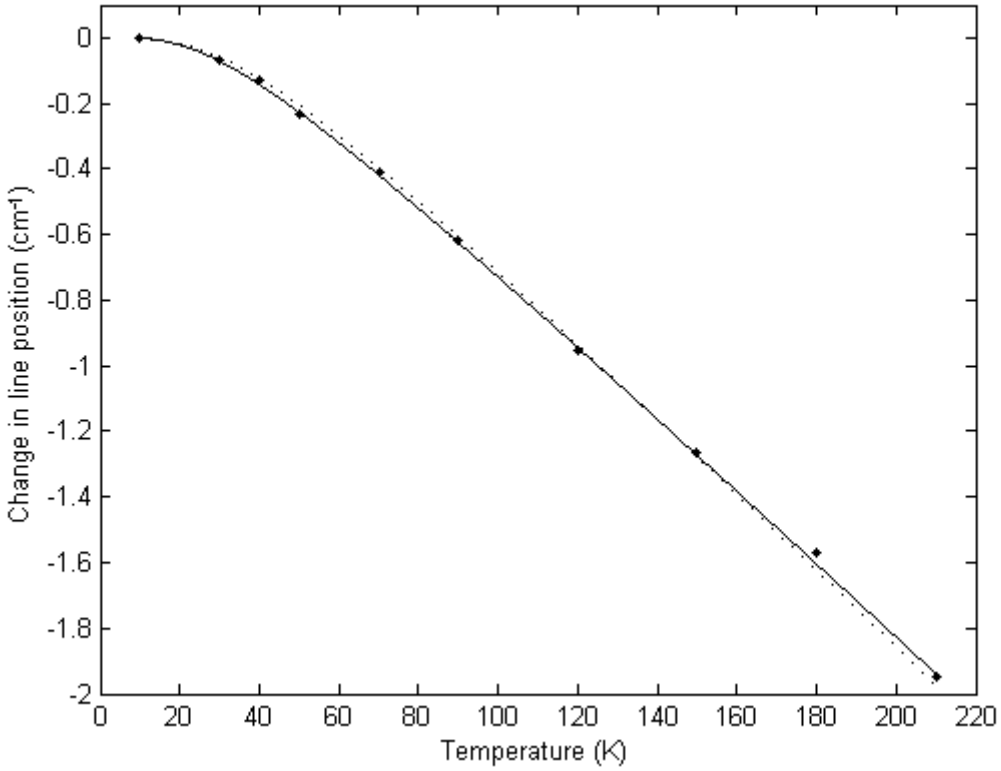

Figure 5-12: Comparison of the fits of the temperature dependence of the line position of the $CsCdBr_3:Er^{3+}$ Z_1 $\boldsymbol{\gamma_{5,6}}$ → Y_2 $\boldsymbol{\gamma_4}$ transition varying the Debye temperature from that obtained from the cutoff frequency (129 K [43]) as given by the dotted line, and treating it as a variable as given by the solid line.

In the case of the Z_1 $\gamma_{5,6}$ → Y_2 γ_4 transition there is only a small difference between the set Debye temperature (129 K) fit and the variable Debye temperature (112 K) fit. Using least squares fitting the best fit is determined to be the varied Debye temperature, although the difference is slight.

A Debye temperature of 112 K corresponds to a Raman phonon state [42], whereas one of 129 K would indicate (from chapter 5.5) that Raman processes are minimal, and corresponds to optical transverse phonon state.

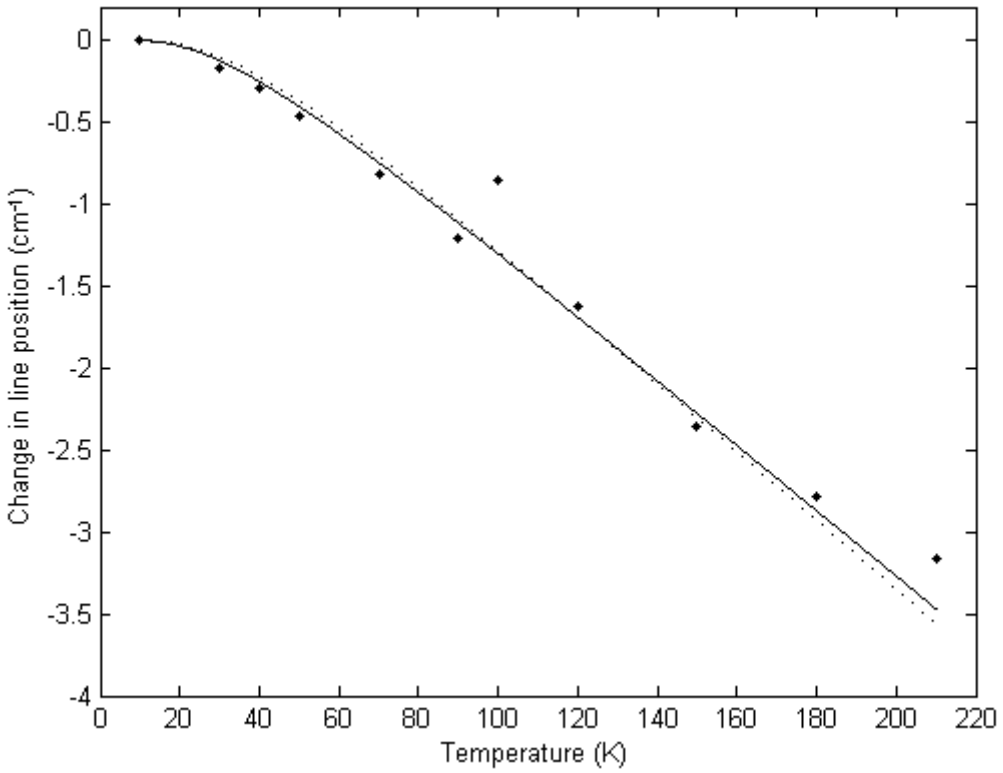

Figure 5-13: Comparison of the fits of the temperature dependence of the line position of the $CsCdBr_3:Er^{3+}$ Z_1 $\boldsymbol{\gamma_{5,6}}$ → Y_3 $\boldsymbol{\gamma_{5,6}}$ transition varying the Debye temperature from that obtained from the cutoff frequency (129 K [43]) as given by the dotted line, and treating it as a variable as given by the solid line.

The $Z_1\ \gamma_{5,6} \rightarrow Y_3\ \gamma_{5,6}$ transition (figure 5.13) and $Z_1\ \gamma_{5,6} \rightarrow Y_5\ \gamma_{5,6}$ transition (figure 5.14) have the same fitted Debye temperatures as the $Z_1\ \gamma_{5,6} \rightarrow Y_2\ \gamma_2$ transition (figure 5.10), and much the same conclusions can be drawn from the fits. Although in these cases the differences between the fits is slightly greater, the varied Debye fits are still better. The phonon modes which these Debye temperatures correspond to are identical to those for the $Z_1\ \gamma_{5,6} \rightarrow Y_2\ \gamma_4$ transition.

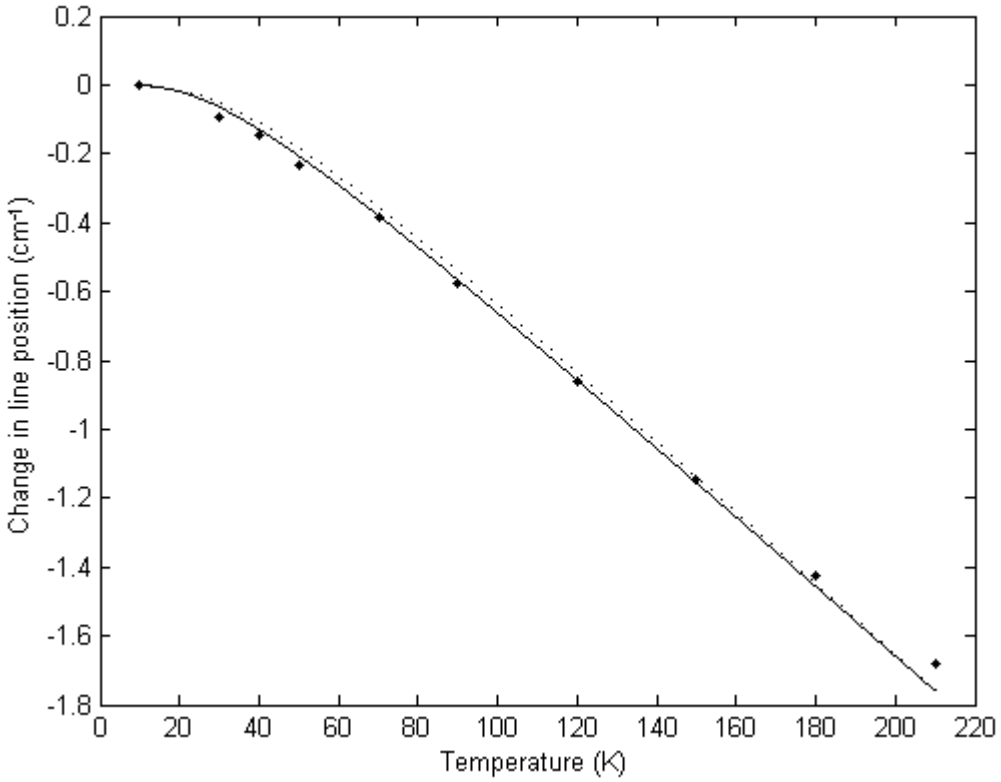

Figure 5-14: Comparison of the fits of the temperature dependence of the line position of the $CsCdBr_3:Er^{3+}$ Z_1 $\boldsymbol{\gamma_{5,6}} \rightarrow Y_5$ $\boldsymbol{\gamma_{5,6}}$ transition varying the Debye temperature from that obtained from the cutoff frequency (129 K [43]) as given by the dotted line, and treating it as a variable as given by the solid line.

The Z_2 $\gamma_4 \rightarrow Y_1$ γ_4 transition (figure 5.15) had a variable Debye temperature of 228 K. The set Debye temperature fit does not match the data particularly well, this being the only transition studied where a fit was able to be obtained at all where this was so. Even the variable Debye temperature fit only provides an adequate fit to the data; this is perhaps due to the shortness of the temperature range. At higher temperatures other transitions, such as the Z_3 $\gamma_4 \rightarrow Y_2$ γ_4, make it difficult to accurately determine the line position, limiting the range of temperatures for analysis.

For this transition the varied Debye temperature is notable in that at 228 K it is the only one higher than the Debye temperature obtained from the cutoff frequency. This Debye frequency corresponds to an optical longitudinal phonon state [42].

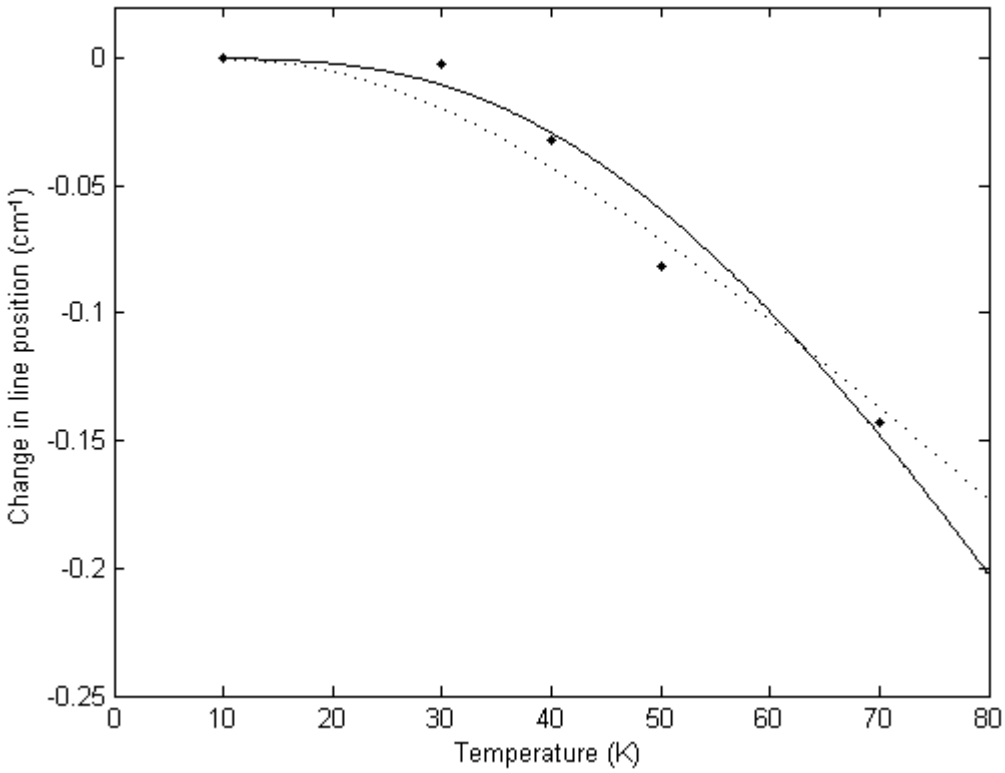

Figure 5-15: Comparison of the fits of the temperature dependence of the line position of the $CsCdBr_3:Er^{3+}$ Z_2 $\boldsymbol{\gamma_4}$ → Y_1 $\boldsymbol{\gamma_4}$ transition varying the Debye temperature from that obtained from the cutoff frequency (129 K [43]) as given by the dotted line, and treating it as a variable as given by the solid line.

The Z_2 γ_4 → Y_3 $\gamma_{5,6}$ transition (figure 5.16) had a variable Debye temperature of 90 K. This is significantly lower than that obtained from the cutoff frequency. This corresponds to a Debye frequency of 63 cm^{-1}, which matches an optical longitudinal phonon state of 62.2 cm^{-1} [42]. A more precise agreement could not be obtained because ω_D could not be smaller due to the limits in the equation used.

There is a smaller difference in this transition between the fits from the set and the varied Debye temperatures than in the Z_2 γ_4 → Y_1 γ_4 transition, but the varied fit is much closer to the data than that from the set Debye temperature.

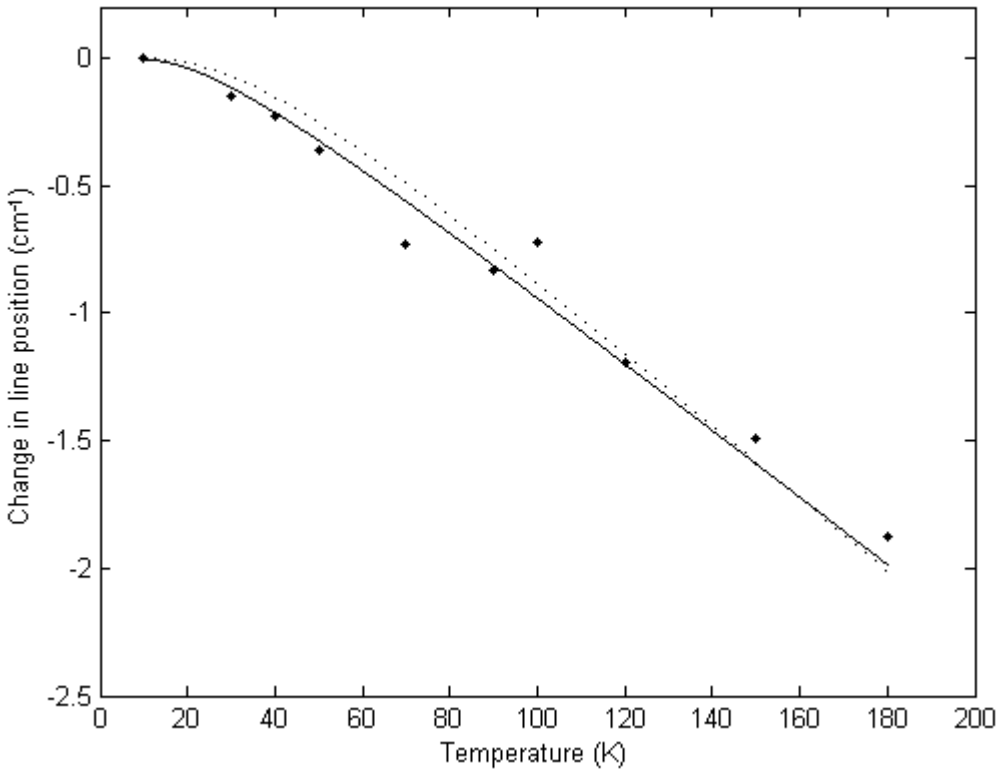

Figure 5-16: Comparison of the fits of the temperature dependence of the line position of the $CsCdBr_3:Er^{3+}$ Z_2 $\boldsymbol{\gamma_4}$ → Y_3 $\boldsymbol{\gamma_{5,6}}$ transition varying the Debye temperature from that obtained from the cutoff frequency (129 K [43]) as given by the dotted line, and treating it as a variable as given by the solid line.

Transition	α' (cm^{-1})	T_D (K)	ω_D (cm^{-1})	σ
$Z_1\,\gamma_{5,6} \rightarrow Y_2\,\gamma_4$	-3.8	112	78	0.004
	-4.6	129	90	0.002
$Z_1\,\gamma_{5,6} \rightarrow Y_3\,\gamma_{5,6}$	-6.8	112	78	0.03
	-8.3	129	90	0.03
$Z_1\,\gamma_{5,6} \rightarrow Y_5\,\gamma_{5,6}$	-3.45	112	78	0.001
	-4.1	129	90	0.02
$Z_2\,\gamma_4 \rightarrow Y_1\,\gamma_4$	-5.7	228	158	0.04
	-1.6	*129*	*90*	*0.04*
$Z_2\,\gamma_4 \rightarrow Y_3\,\gamma_{5,6}$	-3.6	90	*63*	0.02
	-5.7	*129*	*90*	*0.03*

Table 5-6: Summary of the parameters for the fitted curves for line shift for Er^{3+}:$CsCdBr_3$. The fits for the Z_2 $\boldsymbol{\gamma_4}$ → Y_1 $\boldsymbol{\gamma_4}$ and Z_2 $\boldsymbol{\gamma_4}$ → Y_3 $\boldsymbol{\gamma_{5,6}}$ transitions with a Debye temperature of 129 K are included for comparative purposes.

None of the transitions used the Debye temperature, although the closeness of the fits for the $Z_1\,\gamma_{5,6} \rightarrow Y_2\,\gamma_4$, $Z_1\,\gamma_{5,6} \rightarrow Y_3\,\gamma_{5,6}$ and $Z_1\,\gamma_{5,6} \rightarrow Y_5\,\gamma_{5,6}$ transitions suggest that it is possible.

Further investigation would be necessary to investigate whether Raman phonon states are significant in this process for these transitions or not. Regardless of which phonon process is dominant, the change in coupling constant is of the some magnitude, with the largest change being 1.5 cm^{-1} for the $Z_1\ \gamma_{5,6} \rightarrow Y_3\ \gamma_{5,6}$ transition. This means that it is at least possible to draw trends along the series.

5.7 Conclusion

The discrepancies between the crystal field model used in this chapter and the experimentally derived energy levels, suggest that the crystal field parameters used need adjusting. Further, although the simulated spectra was able to be used to suggest that the orientation of the $[MX_3]^-$ chains were perpendicular to the spectrometer, and that the approximately 2:1 σ to π polarization suggests a slight circular dichroism. There were some significant problems with the intensities of the transitions relative to the experimental spectra, suggesting that there are some issues with this model as well, probably to the lack of electric dipole transitions considered.

The model for the temperature dependence of the line broadening indicated that in all but one of the observed transitions Raman scattering is not significant, instead being mostly caused by one-phonon direct processes. If the Raman scattering coupling constant is non-zero but small, approximately 0.1, then on the scale studied in this chapter the broadening from this source would not be significant, but at higher temperatures would become more so.

The temperature dependence of the line shift showed an interesting trend in that three of the five studied transitions used the same Debye frequency, 78 cm^{-1}. This corresponds to a Raman phonon state, suggesting that while these transitions are not broadened by Raman processes, they are shifted by them. This is in agreement with the difference in the effective Debye temperatures between the two processes.

Chapter 6 Discussion and Conclusions

The comparison between the Er^{3+} in CaF_2 and $CsCdBr_3$ is interesting as it shows the effect that the mass of the ligand has on the linewidth and the line position. The lighter F^- ligand in CaF_2 results in a relatively high Debye temperature, and there are consequently many available phonon states, whereas the heavy Br^- ligands in comparison retard phonon propagation, resulting in a much lower Debye temperature.

The effect of different masses in Er^{3+} doped crystals is apparent in the linewidths. The CaF_2:Er^{3+} 4f transitions studied in chapter 4 had, generally, quite strong Raman scattering components in their broadening. In comparison the $CsCdBr_3$:Er^{3+} 4f transitions in chapter 5 generally had negligible Raman scattering components. This is likely due to the Raman scattering being a two phonon process, and if phonons are less common then single phonon processes are more likely to dominate.

It is difficult to compare this work with other studies of linewidths involving heavy ligands, such as the comparison of the actinide ion U^{3+} in, $LaBr_3$ and $LaCl_3$ by Karbowiak et al [44] because the other studies do not include the one-phonon direct processes in their models. This work has shown that even when Raman scattering dominates, the single-phonon direct process can cause a significant change in the size of the coupling constant. Even so, the lower Debye temperature in the $LaBr_3$, despite the problems Karbowiak et al had determining it and consequently the uncertainty they have in their results, does lead to a higher average coupling constant for Raman scattering. This is in contrast to the results obtained from the work in chapters 4 and 5. This therefore requires further investigation to determine whether this difference is due to the lack of consideration of single-phonon direct processes by Karbowiak et al, or whether some other process is involved.

Ellens et al. [14] also did not include single-phonon direct processes in their linewidth studies, so comparison with their results is also difficult. A Ellens et al determined the electron-phonon coupling constant for Raman scattering for $LiYF_4$:Er^{3+} to be small, approximately 35 cm^{-1}. This corresponds with an average of approximately 240 cm^{-1} for that of CaF_2:Er^{3+} in chapter 4 of this work, which is quite large. It should be noted however that there is a lot more variation in the values of the coupling constant in this work. This is due to studying just the $^4I_{15/2} \rightarrow$ to $^4I_{13/2}$ transitions in this work, whilst Ellens et al. just studied the clearest transitions in the UV range, and it is unclear what effect this may have had on the coupling constant range in relation to weaker transitions. The size of the coupling constant in CaF_2:Er^{3+} indicates an overall much stronger Raman scattering component than in the $LiYF_4$:Er^{3+}. As the factoring in of one-phonon

direct processes lowered the coupling constant, the large difference is not likely to be due to A Ellens et al not considering these. Therefore we must look at the F^- - Er^{3+} bond length to see why the discrepancy arises. The bond length for Y^{3+} - F^- in $LiYF_4$ is either 2.297 Å or 2.244 Å depending on the F^- ion [45], while the bond length for the Ca^{2+} - F^- in CaF_2 is 2.44 Å [46]. Because in CaF_2, unlike $LiYF_4$, the Er^{3+} does not match the charge of the ion it is displacing, the bond length will shorten. This will distort the fluorine cage inwards slightly. Using the ionic radii calculated by R D Shannon [47], the bond length was taken to be 2.31 Å. This bond length is approximately the same as the Er^{3+} – F^- in the $LiYF_4$, which from the same study by Shannon can be determined to be 2.30 Å. Crucially, however, the Y^{3+} - F^- bond length as predicted by the ionic radii from Shannon of 2.319 Å does not match the experimentally derived bond length of ~2.2 Å. Therefore we can predict that the bond length of Er^{3+} - F^- will be shorter. Shorter bond lengths cause stronger interactions between the dopants and the ligands, causing an increase in covalency [44] and therefore a reduction in the coupling is expected. This is seen in the average of the experimental results with a Raman scattering coupling constant of ~ 35 cm^{-1} for $LiYF_4:Er^{3+}$ [14] and ~ 240 cm^{-1} for $CaF_2:Er^{3+}$.

The bond length of the Cd^{2+} - Br^- in $CsCdBr_3$ is 2.770 Å [22], and like in CaF_2 it would be compressed slightly by the replacement of an Er^{3+} ion for a Cd^{2+}. Unlike in CaF_2, the structure of $CsCdBr_3$ allows more flexibility in bond lengths, as the arrangement of the long chains can tolerate significant structural changes due to impurities [22]. The calculated bond length using the ionic radii determined by Shannon [47] for Er^{3+} - F^- is 2.85 Å, however the calculated Cd^{2+} - Br^- bond length is 2.91 Å and the discrepancy between this and the experimentally derived value and the way the crystal structure of $CsCdBr_3$ can deform means that the precise bond length is unknown and could be within such a range that to speculate on the value is of limited utility. The negligible value of the coupling constant for Raman scattering suggests that under this model the bond length should be very short, or one of the other multitude of factors affecting the coupling constant is coming into play. The most likely factor is that the high mass of the ligand, causing a very low Debye temperature, is reducing the number of phonons making higher order processes, such as the two-phonon Raman scattering process, less likely.

The $CaF_2:Er^{3+}$ linewidth study in chapter 4 agreed with the work of Karbowiak et al [44] on the nature relation of bond length to the electron-phonon coupling constant, in relation to the work of A Ellens et al [14] on $LiYF_4:Er^{3+}$. The $CsCdBr_3:Er^{3+}$ study in chapter 5, in relation to chapter 4, suggested that higher mass ligands may cause lower Raman scattering electron-phonon

coupling constants, due to the significantly lower Debye temperature, which reduced the availability of phonons, meaning single phonon processes dominate.

The line shift studies in chapters 4 and 5 are highly dependent on the linewidth studies in their respective chapters for interpretation, as the phonon processes which broaden the transitions can also cause the line shifts. The transition in the $CaF_2:Er^{3+}$ line shift study of most note is the $Z_3 \rightarrow Y_1$ transition in C_{4v} point symmetry, as it is the only transition in that series that is blue-shifted. This is due to the energy of the intermediate electronic level being higher than that of the initial level [32], as the other transitions went through other intermediate levels. However, as is evident from the start of this transition, and many of the other transitions in this host and in $CsCdBr_3:Er^{3+}$, there are important contributions that were discarded from intermediate states with energies. These contributions were much smaller than those with energies but, as was shown with the direct single-phonon processes in the linewidth studies, even small contributions are capable of causing a substantial improvement in the data fit, and therefore a much improved set of parameters. Not using those parameters, however, some conclusions are able to be drawn. In the $CaF_2:Er^{3+}$ case, the varied Debye temperature was substantially different from the experimentally derived value in almost all of the cases, the exception being the $Z_3 \rightarrow Y_1$ C_{4v} transition. This suggests that in these cases the phonon modes causing the line shifts are different from those causing the line broadening, and the dominant phonon process in this seems to be vibronic processes.

In comparison, the line shift study for $CsCdBr_3:Er^{3+}$ had much more consistent values for the coupling constants, being between -3.45 and -8.3 cm^{-1}. In over half of the cases examined it is difficult to determine whether the variable Debye temperature fit or the fixed Debye temperature fit is better. The correct fit is therefore most likely to be the varied Debye temperature fit, due to a distribution of phonon modes of similar intensity. This means that the lines are most likely shifted by a combination of Raman processes and optical phonons, as in the linewidth study for this host the Raman processes are negligible, and the varied Debye temperatures for these modes correspond to optical phonon modes.

References

[1] R J Mears, L Reekie, S B Poole, D N Payne, *Electron. Lett.* **22** (1986) 159.

[2] E Desurvire, J R Simpson, P C Becker, *Optics Letters* **12** (1987) 888.

[3] A Kiel *Phys. Rev.* **126** (1962) 1292.

[4] G Burns, E A Geiwss, B A Jenkins, M Nathan *Phys. Rev.* **139** (1965) A1687.

[5] D E McCumber, M D Sturge *J. Appl. Phys.* **34** (1963) 1682.

[6] G F Imbusch, W M Yen, A L Schawlow, D E McCumber, M D Sturge *Phys. Rev.* **133** (1964) A1029.

[7] W M Yen, W C Scott, A L Schawlow *Phys. Rev.* **136** (1964) A271.

[8] J T Gourley *Phys. Rev. B* **5** (1972) 22.

[9] J Hegarty, W M Yen *Phys. Rev. Lett.* **43** (1979) 1126.

[10] K H Hellwege, P Hill, S Hüfner *Solid State Comm.* **5** (1967) 687.

[11] J H Van Vleck *Phys. Rev.* **57** (1940) 426.

[12] A Ellens *Electron-phonon coupling of lanthanide ions in solids*, PhD thesis (unpublished) Utrecht University (1996).

[13] A Ellens, H Anders, A Meijerink, G Blasse *Phys. Rev. B* **55** (1997) 173.

[14] A Ellens, H Andres, M L H ter Heerdt, R T Wegh, A Meijerink, G Blasse *Phys. Rev. B* **55** (1997) 180.

[15] J Becquerel, *Phys. Z.* **8** (1908) 632.

[16] F H Spedding *Phys. Rev.* **37** (1931) 777.

[17] C G Mosander *Phil. Mag.* **23** (1843) 241.

[18] B G Wybourne *Spectroscopic Properties of Rare Earths*, John Wiley & Sons, Inc, 1965.

[19] J-P Wells, R J Reeves *Phys. Rev. B* **64** (2001) 035102.

[20] N J Cockroft, G D Jones, R W G Syme *J. Chem. Phys.* **92** (1990) 2166.

[21] H K Welsh *J. Phys. C: Solid State Phys.* **18** (1985) 5637.

[22] G L McPherson, A M McPherson, J L Atwood *J. Phys. Chem. Solids.* **41** (1979) 495.

[23] J R Quagliano, N J Cockroft, K E Gunde, F S Richardson *J. Chem. Phys.* **105** (1996) 9812.

[24] J Heber, J Neukum, M Altwein, R Deirbilek, N Bodenschatz *Spectrochimica Acta A* **54** (1998) 1557.

[25] N J Cockroft, G D Jones, D C Nguyen *Phys. Rev. B* **45** (1992) 5187.

[26] G Liu, B Jacquier *Spectroscopic Properties of Rare Earths in Optical Materials*, Springer, New York, 2005.

[27] S Hüfner *Optical Spectra of Transparent Rare Earth Compounds*, Academic Press Inc, New York, 1978.

[28] W T Carnall, G L Goodman, K Rajnak, R S Rana *J. Chem. Phys.* **90** (1989) 3443.

[29] K Rajnak, B G Wybourne *Phys. Rev.* **132** (1963) 280.

[30] B R Judd *Phys. Rev.* **141** (1966) 141.

[31] H H Marvin *Phys. Rev.* **71** (1947) 102.

[32] R Powell *Physics of Solid State Laser Materials*, Springer-Verlag, New York, 1998.

[33] S P Jamison, R J Reeves *Phys. Rev. B* **67** (2003) 115110.

[34] M Mujaji, G D Jones, R W G Syme *Phys. Rev. B* **46** (1992) 14398.

[35] M Mujaji *Solid State Spectroscopy: Laser Selective Excitation of Holmium Ions in Crystalline Solids*, PhD thesis (unphblished) University of Canterbury (1992).

[36] J J Olivero, R L Longbothum *J. Quant. Spec. Radiat. Transfer* **17** (1977) 90161.

[37] P S Ho, A L Ruoff *Phys. Rev.* **161** (1967) 864.

[38] C A Freeth, G D Jones, R W G Syme *J. Phys. C: Solid State Phys.* **15** (1982) 5667.

[39] W A Hargreaves *Phys. Rev. B* **6** (1972) 3417.

[40] X Chen, B Di Bartolo *J. Appl. Phys.* **75** (1994) 1710.

[41] J P Russel *Proc. Phys. Soc.* **85** 194.

[42] B Z Malkin, A I Iskhakova, S Kambs, J Heber, M Altwein, G Schaack *Phys. Rev. B* **63** (2001) 075104.

[43] R B Barthem, R Buisson, R L Cone *J. Chem. Phys.* **91** (1989) 627.

[44] M Karbowiak, M Sobczyk, J Drożdżyński *J Solid State Chem.* **177** (2004) 2415.

[45] E Garcia, R R Ryan *Acta Cryst.* **C49** (1993) 2053.

[46] S Picozzi, S Massidda, A Continenza, R Resta *Phys. Rev. B* **55** (1997) 16318.

[47] R D Shannon *Acta Cryst.* **A32** (1976) 751.